

METAL-INSULATOR MULTISTACKS FOR ABSORPTION AND PHOTODETECTION

A THESIS SUBMITTED TO
THE GRADUATE SCHOOL OF ENGINEERING AND SCIENCE
OF BILKENT UNIVERSITY
IN PARTIAL FULFILLMENT OF THE REQUIREMENTS FOR
THE DEGREE OF
MASTER OF SCIENCE
IN
ELECTRICAL AND ELECTRONICS ENGINEERING

By
Sina Abedini Dereshgi
May, 2017

Metal-Insulator Multistacks For Absorption and Photodetection

By Sina Abedini Dereshgi

May, 2017

We certify that we have read this thesis and that in our opinion it is fully adequate, in scope and in quality, as a thesis for the degree of Master of Science.

Ekmel Özbay(Advisor)

Vakur Behçet Ertürk

Alpan Bek

Approved for the Graduate School of Engineering and Science:

Ezhan Kardeşan
Director of the Graduate School

ABSTRACT

METAL-INSULATOR MULTISTACKS FOR ABSORPTION AND PHOTODETECTION

Sina Abedini Dereshgi

M.S. in Electrical and Electronics Engineering

Advisor: Ekmel Özbay

May, 2017

Metal-insulator (MI) stacks are one of the most studied nanoscale devices of the recent decade. These structures have opened a new door to endless photonic applications ranging from solar cells to waveguides and polarizers. The main attribute of metal-insulator stacks is possibility of scaling down device dimensions with them that is the main trend in photonic and electronic technology nowadays. The conventional photonic structures require very high thicknesses where novel photonic devices can show many artificial properties by tailoring specifically designed metal-insulator cells also known as metamaterials.

In this thesis, we will investigate some metal-insulator absorber stacks with capability of highly confining light specifically for photodetection. The near-infrared part of the electromagnetic spectrum is problematic in photocurrent generation due to the fact that conventional narrow band gap PN photodiodes fail to function in room temperature. Adding to this predicament is their large dimensions. Some of these problems are addressed in this thesis. First a plasmonic MIM structure is studied with random nanoparticles obtained by dewetting in the top layer which confines the incident light in the plasmonic MIM cavity and gives rise to high absorption through surface plasmon polariton excitation in the bottom lossy metal. Several materials are investigated in order to engineer best absorbers with the focus on absorption in the bottom metal which is critical for photodetection. Our simulations and experimental results demonstrate over 90 percent absorption for most of the visible and near-infrared region. The absorption in the bottom metal in a structure comprised of chromium-aluminum oxide-silver nanoparticles (bottom to top) reaches 82 percent at 850 nm. After obtaining appropriate NIR absorption, an MIMIM photodetector is designed and fabricated where another insulator-metal layer is added to the bottom of the previous absorber. The formerly reported plasmonic photodetectors put the burden of absorption and

photocurrent path on the same MIM structure putting restrictions on device design. In our proposed structure, however, tunneling MIM photocurrent junction is used which shares only its top metal with the top absorbing MIM. The main advantage of this structure is that it separates the absorption and photocurrent parts of the photodetector, making separate optimization of each MIM possible. The best structure which is silver-hafnium oxide-chromium-aluminum oxide-silver nanoparticles (top to bottom) demonstrates a peak photoresponsivity (from non-radiative decay of surface plasmon polaritons) of 0.962 mA/W at 1000 nm and a dark current of only 7 nA in a bias of 50 mV. Our results demonstrate approximately two orders of magnitude enhancement in photoresponsivity compared to previously reported MIMIM photodetectors.

In another attempt to obtain perfect absorbers for visible and near-infrared regions, we put forth an MIMI absorber. In this work, the contribution of metal layers is studied in detail and material choice is discussed. Our optimization process suggests a versatile method for designing perfect absorbers. Transfer matrix method as well as FDTD simulations are used to optimize thicknesses. Furthermore, in order to shed light on material selection, impedance matching of the waves in the multilayer media to free space is proposed for the extraction of ideal metal permittivity values and comparing them to existing metals. Our experimental result of a tungsten-aluminum oxide-titanium-aluminum oxide (bottom to top) structure illustrates over 90 percent absorption for wavelength range of 400 nm to 1642 nm which is the highest perfect absorption bandwidth reported in similar MIMI structures to the best of our knowledge.

Keywords: Plasmonics, Metal-insulator stacks, Broadband perfect absorption, Lithography-free, Nanocavity, Tunneling photodetectors, Near-infrared.

ÖZET

EMİLİM VE FOTO ALGILAMA İÇİN METAL-YARI İLETKEN ÇOKLU İSTİFLERİ

Sina Abedini Dereshgi

Elektrik ve Elektronik Mühendisliği, Yüksek Lisans

Tez Danışmanı: Ekmel Özbay

Mayıs 2017

Bu tezde, özellikle ışık algolamak için ışığı olduka sınırlayan bir özellikteki metal izolatör emici yığınlarını inceleyeceğiz. Elektromanyetik spektrumun yakın kızıl ötesi kısmı, geleneksel dar bant aralıklı PN fotodiyotlarının oda sıcaklığında çalışmaması nedeniyle foto akım oluşumunda sorunludur. Bu çıkmaza birde büyük boyutları eklenmektedir. Bu tezlerden bazılarında bu sorunlar ele alınmıştır. Önce plazmonik bir MIM yapısı, üst katmanda dewetting ile elde edilen rastgele nanopartiküller ile gözlemlenir ve bu da, plasmonik MIM boşluğundaki olay ışığını sınırlar ve alttaki kayıplı metalde yüzey plasmon uyarımıyla yüksek absorpsiyona neden olur. Işık algılama için kritik olan alt metal emilimine odaklanarak en iyi emiciler elde etmek amacıyla çeşitli malzemeler araştırılmaktadır. Simülasyonlarımız ve deney sonuçları, görünür ve yakın kızılötesi bölgelerin çoğunda emiliminin yüzde 90'ın üzerinde olduğunu göstermektedir. Krom-alüminyum oksit-gümüş nanoparçacıklardan (altdan üste) oluşan bir yapıdaki alttaki metalin emilmesi 850 nm'de yüzde 82'ye ulaşır. Uygun NIR absorpsiyonu elde ettikten sonra, bir MIMIM foto-detektörü tasarlanır ve bir başka izolatör-metal tabakasının önceki absorbe edicinin tabanına eklendiği yerde imal edilir. Eskiden bildirilen plasmonik fotodetektörler, aynı MIM yapısında emilim ve foto akım cihaz tasarımına kısıtlamalar getirmiştir. Bununla birlikte, önerilen yapıımızda tünelleme MIM foto akım kullanılır, bu sadece üst metalini st emici MIM ile paylar. Bu yapının en büyük avantaj, fotodetektörün emme ve foto-akım bölümlerini ayırması, böylece her bir MIM'in ayrı ayrı optimizasyonunu mümkün kılmaktadır. Gümüş-hafniyum oksit-krom-alüminyum oksit-gümüş nanopartiküller (üstten alta) olan en iyi yapı, 1000 nm'de 0.962 mA / W'lık bir zirve foto responsivitesini (yüzey plazmonlarının radyasyona bağlı bozulmasından) ve karanlık akımı 50 mV öngeriliminde 7 nA'dır. Sonuçlarımız, daha önce bildirilen MIMIM fotodetektörlerine kıyasla fotoresponsivitede yaklaşık

yüz kat büyüklüktedir.

Görünür ve yakın kızılötesi bölgeler için mükemmel emiciler elde etmek için yapılan başka bir girişimde, bir MIMI emiciyi ortaya koyulmuştur. Bu çalışmada, metal tabakaların katkısı ayrıntılı olarak incelenmiş ve malzeme seçimi tartışılmıştır. Optimizasyon prosesi, mükemmel emiciler tasarlamak için çok yönlü bir yöntem önermektedir. Kalınlıkları optimize etmek için transfer matrisi yöntemi ve FDTD simülasyonları kullanılmıştır. Ayrıca, malzeme seçimine ışık tutmak için, ideal metal permitivite değerlerinin çıkarılması ve mevcut metallere kıyasla boş alana empedans eşleştirilmesi önerilmektedir. Tungsten-alüminyum oksit-titanyum-alüminyum oksit (tepeden aşağıya doğru) yapısına ait deney sonuçlarımız, benzer MIMI yapılarında en iyi mükemmel absorpsiyon bant genişliği olan 400 nm ile 1642 nm arasındaki dalga boyu aralığında yüzde 90'ın üzerinde absorpsiyonu göstermektedir.

Anahtar sözcükler: Plasmonik, Metal yalıtkan iatifleri, Genişband mükemmel absorbe ediciler, Litografisiz, Nano kavite, Tunnelemeli foto detektör, Yakın kızıl ötesi.

Acknowledgement

First, I would like to express my sincere appreciation to Prof. Ekmel Özbay for his wise supervision, endless support, encouragement and being a role model for success. Also, I would like to thank Dr. Bayram Bütün for his supervision. I learned to be professional and productive thanks to the work ethics in NANO-TAM. I would like to thank Prof. Ali Kemal Okyay who walked me through the first steps to teach me how to be a scientist. Second, I would like to state my deep gratitude to Prof. Vakur Behçet Ertürk and Prof. Alpan Bek for allocating their time to investigate my work and providing me with invaluable comments to make this thesis stronger.

I would like to thank Negin for making pleasant distractions from my work and making me experience rare fun events during my studies. I am so grateful to know her in the first place and I am thankful for her unconditional support during the good and bad days. I am also very grateful to make good friends in the path of my studies; specifically Amir for being a friend and an insightful mentor who made big amendments to all my works. I would like to appreciate the UNAM and NANOTAM family for the friendly environment they provided which was perfect for learning. Also, I am thankful for my friends, Bahram, Hodjat, Berkay, Alireza, Sami and Amin who provided warm company and scientific arguments and were like family all these years.

Last but not least, I would like to dedicate this thesis to the unconditional love and support of my family, my mother, sister and brother in law who had to bear with my rare visits. I could not have imagined a better upbringing if they were not always there for me. Specifically, my main source of inspiration, my father, who has always been a role model for wisdom and open-mindedness. He has always said that *"Success is the area of a rectangle where one side is intelligence and the other one is diligence. Even if you feel that you are not intelligent enough, you can compensate with hard work and there is no excuse for not achieving success"*.

Contents

- 1 Introduction** **1**
 - 1.1 Background 1
 - 1.2 Motivation and Thesis Outline 4

- 2 Theory and Methods** **5**
 - 2.1 Absorption 7
 - 2.1.1 Optical absorption 7
 - 2.1.2 Plasmonic Absorption 11
 - 2.1.3 Cavity Absorption 21
 - 2.2 Photodetection 24
 - 2.2.1 PIN photodetectors 26
 - 2.2.2 Avalanche photodetectors 28
 - 2.2.3 MSM photodetectors 28
 - 2.2.4 Quantum well photodetectors 29

<i>CONTENTS</i>	ix
2.2.5 Metal semiconductor photodetectors	30
2.2.6 Metal insulator photodetectors	33
3 Simulation, Fabrication and Characterization	36
3.1 Simulation	36
3.2 Fabrication	37
3.2.1 PVD	38
3.2.2 CVD	40
3.2.3 RTA	44
3.2.4 Photolithography	45
3.2.5 Etching	47
3.3 Characterization	48
3.3.1 Ellipsometer	48
3.3.2 FTIR	50
3.3.3 Spectral Photoresponsivity and Normal Absorption	51
4 Plasmonic MIM Absorbers and MIMIM Photodetectors	54
4.1 Introduction	55
4.2 MIM Absorption	57
4.3 MIMIM Photodetection	63

<i>CONTENTS</i>	x
4.4 Discussion	66
5 MIMI Cavity Absorbers	69
5.1 Introduction	69
5.2 Calculation and Analysis	70
5.3 Results and Discussion	72
6 Conclusion	79
A ALD Recipe and Characterization	91

List of Figures

2.1	Classification of metamaterials with respect to their optical parameters.	6
2.2	E-k diagram of a direct bandgap semiconductor with two transitions illustrated with red arrows.	8
2.3	(a) Direct, (b) phonon assisted, (c) two photon and (d) trap assisted absorption.	9
2.4	(a) Schematic of the SPPs and the geometry of solving Maxwell's equations and (b) Kretschmann configuration for SPP excitation.	13
2.5	(a) Schematic of the SPPs excitation from high-index medium and (b) Dispersion relation for SPP excitation from high-index medium.	15
2.6	(a) Schematic of the SPP excitation using grating structure and (b) dispersion relation in gratings.	16
2.7	(a) Metallic nanoparticle under illumination in quasi-static approximation and (b) increased absorption cross section in resonance.	16
2.8	(a) Schematic of the test MIM structure and (b) absorption vs wavelength in VIS and NIR spectra with designation of LSP and SP peaks.	19

2.9	E-field magnitude in a cross section of the structure at (a) higher order resonance 483 nm and (b) fundamental resonance 763 nm, the simulated Poynting vector magnitude (for the first peak of 463 nm) in the structure at (c) SPP resonance of 476 nm and (d) LSP resonance of 500 nm. The white lines mark the boundaries of the three layers of the MIM.	20
2.10	Schematic of the MIMI cavity absorber.	22
2.11	(a) Schematic and (b) the energy band diagram (at equilibrium) of a PIN Ge/SiGe photodetector.	27
2.12	(a) Schematic and (b) the electric field (at equilibrium) of an avalanche Ge/SiGe photodetector.	28
2.13	(a) Schematic and (b) the energy band diagram (at equilibrium) of a Ge symmetric MSM photodetector.	29
2.14	Energy band diagram of a quantum well (a) in equilibrium and (b) under applied bias.	30
2.15	(a) Schematic and (b) energy band diagram and photocurrent generation mechanism in Schottky photodetectors.	31
2.16	(a) Circuit model and (b) logarithmic I-V curve of a fabricated Schottky diode.	32
2.17	A symmetric tunneling barrier MIM structure in equilibrium.	34
2.18	(a) MIM and (b) MIMIM photodetector structure [1].	35
3.1	Lumerical FDTD Solutions environment.	37
3.2	(a) Schematic of the chamber of a thermal evaporator (PVD system) and (b) the deposition geometry.	38

3.3	VAKSIS (a) thermal evaporator and (b) sputtering systems.	39
3.4	(a) Schematic of the chamber of a DC sputtering system and (b) the voltage drop inside the chamber.	40
3.5	(a) Schematic of an ALD system and (b) Cambridge Nanotech Savannah S-100 ALD system.	41
3.6	Al ₂ O ₃ deposition from TMA and water cycles. (a) Introduction of hydroxyl groups to the surface and pulse of TMA in to the chamber, (b) reaction between TMA and the hydroxyl groups and purge of the byproducts, (c) introduction of hydroxyl groups to the surface and (d) reaction between TMA and the hydroxyl groups and purge of the byproducts	43
3.7	ATV Technologie GmbH, SRO-704 RTA system.	45
3.8	(a) Schematic of the exposure in proximity mode and (b) the aligner system used.	46
3.9	(a) Schematic of wet and dry etched grating sample and (b) the inductively coupled plasma etch system used for devices in this thesis.	48
3.10	(a) Schematic of an ellipsometer and (b) J.A. Woollam Co. Inc. VASE Ellipsometer.	49
3.11	Bruker Vertex 70v FTIR in NANOTAM.	51
3.12	(a) Schematic of the home made reflectance measurement setup and (b) the photo of the setup [2].	52
3.13	(a) Schematic of the home made photoresponsivity measurement setup and (b) the photo of the NIR setup [2].	53

4.1 Schematic of the total MIMIM photodetector structure [2]. 56

4.2 (a) Three applied RTA recipes of 500°C heat for 20 min with heating rate of 100 °C/min and cooling rate of 100 °C/min, heating rate of 100 °C/min and cooling rate of 500°C/min and heating rate of 500 °C/min and cooling rate of 50 0°C/min respectively, SEM image of nanoparticles after (b) slow heating-slow cooling, (c) slow heating-rapid cooling and (d) rapid heating-rapid cooling [1]. 58

4.3 (a) particle size distribution analysis of the optimized RTA recipe for 10 nm deposited Ag film and (b) reflection of MIM absorber structure with Al absorbing metal, Ag nanoparticles and three different dielectric materials Al₂O₃, ZnO and TiO₂. [2, 3]. 59

4.4 Measured and computational 3D simulation results of reflectance from a surface of MIMIM (Ag nanoparticles - 40 nm Al₂O₃ - 30 nm M_{abs} - 10 nm HfO₂ 70 nm Ag bottom contact) with M_{abs} chosen to be (a) Aluminum and Gold, (b) Silver and Chromium, (c) simulated absorption percentage in different absorbing metals and (d) sample photos. Inset of (c) illustrates the layer being studied (i.e. absorbing metal) [2, 3]. 61

4.5 Computed field distributions at two different wavelengths. (a) E-field at 400 nm, (b) E-field at 1000 nm, (c) H-field at 400 nm and (d) H-field at 1000 nm for MIMIM structure with Chromium absorbing (middle) metal, at a cross section of the sample which includes and bisects two nanoparticles. The inset between the two E-field figures illustrates the cross section plane in the software environment [1, 2, 3]. 62

4.6 Q_{SPP} for (a) Al, Au, Ag and (b) Cr [2]. 63

4.7 (a) Schematic of the tunneling junction and (b) photo of the sample under microscope [1]. 65

4.8 IV characteristics of MIMIM (Ag nanoparticles - Al_2O_3 - M_{abs} - HfO_2 - Ag negative bottom contact metal) devices with (a) Aluminum absorbing metal and (b) Chromium absorbing metal, photoresponsivity at applied negative 50 mV bias for MIMI (without Ag nanoparticles) and MIMIM devices respectively with (c) Aluminum absorbing metal and (d) Chromium absorbing metal. [2]. 67

4.9 (a) Calculated absorption in the absorbing metal and spectral photoresponsivity at applied negative 50 mV bias for MIMI and MIMIM devices with chromium absorbing metals. [1]. 68

5.1 (a) Schematic of the MIMI structure and (b) over 90% absorption bandwidth for four different double metal- Al_2O_3 (MIMI) stacks where the middle thin metals are 10 nm thick. The insets of Fig. 1 (a) illustrate field directions, the direction of propagation (TE) and the layer and boundary numbers. 71

5.2 Absorption versus wavelength of double MI pairs (MIMI) with $d_d = 80$ nm and thick bottom metals and the same middle thin metal materials of 5 nm, 10 nm, 15 nm, and 20 nm thick (a) Ti, (b) Cr, and (c) W. The green line denotes 90% limit for absorption. 73

5.3 (a) Simulated contour plot of absorption in a cross-section of the MIMI sample with optimum parameters (thin metal thickness of 10 nm and $d_d = 80$ nm) and (b) simulated absorption versus wavelength for infinite slabs of some metals. 74

5.4 (a) Calculated ideal real and imaginary parts of permittivity for bottom reflector thick metal, (b) ideal real relative permittivity versus real parts of relative permittivity of Ti, Cr, and W and (c) ideal imaginary relative permittivity versus imaginary parts of relative permittivity of Ti, Cr, and W. The inset of Fig. 4 (a) shows the known and unknown calculation parameters. 76

5.5 (a) Simulated absorption versus the wavelength and dielectric thicknesses (d_d) for the optimum MIMI sample with $d_{Ti} = 10$ nm, (b) calculated TMM counterpart of part (a), (c) cross section FIB image of the fabricated sample, (d) measured, simulated, and calculated (TMM) absorption at normal incidence, absorption of the fabricated sample (e) measured at different incidence angles (θ degrees) for TE polarization and (f) measured at different incidence angles (θ degrees) for TM polarization. The inset of Fig. 5 (d) shows the sample photo. 78

A.1 Refractive index data of the deposited Al_2O_3 at $200^\circ C$ 92

A.2 Refractive index data of the deposited HfO_2 at $200^\circ C$ 94

A.3 Uniformity test of deposited HfO_2 at $200^\circ C$ on a 4 inch wafer. . . 94

List of Tables

A.1	Al ₂ O ₃ deposition recipe in ALD.	93
A.2	HfO ₂ deposition recipe in ALD.	93

Chapter 1

Introduction

1.1 Background

As nanoelectronic and optoelectronic devices keep scaling down interminably, there has been a lot of research devoted to catch up with this trend to decrease the size of the devices and enhance their efficiency simultaneously. The trend is generally imposed by cost-effective industrial demands that in turn push nanotechnology to come up with smaller and better performing designs [1, 2, 3]. Among the most notable applications of nanophotonic devices are propagation and guiding [4], beaming [5], confinement of the light and absorbers. The perfect, black-body absorbers are capable of almost annihilating reflection and are useful in many applications such as thermal imaging [6], emitters [7], photovoltaics [8], photodetectors [9] and shielding. Some of the main figures of merit for absorbers are flat, near 100 percent absorption, high bandwidth, easy fabrication, small dimensions and polarization insensitivity. The bulk absorbers require very thick layers to absorb light perfectly which are not favorable. Also, some of the plasmonic structures that use Kretschmann and Otto configurations to excite surface plasmon polaritons (SPP) are tacitly considered obsolete due to the fact that they fail to comply with scaling down trend. One of the turning points on the verge of

searching for alternatives was met when scientists started to apply nanoparticle-based plasmonic layers to MIM structures which used the geometry dependence of the plasmonic layers as a major advantage. The geometry dependence nature of plasmonic MIM absorbers provides the tunability of band and peaks of absorption. MIM structures with the top metal layer designed as gratings [10, 11], nanoparticles [12, 13, 14, 15] and nanopillars [16, 17, 18] made way to more efficient, omni directional and compact structures thanks to advanced patterning methods such as electron beam lithography (EBL). MIM structures are capable of confining light in the nanoantenna-air and the spacer insulator layer which correspond to localized surface plasmon (LSP) and SPP excitations respectively [10]. These absorbers function on the basis of bringing together the absorption peaks resulting from LSPs and SPPs to obtain broadband absorption.

Increasing the breadth of absorption is one of the motivations in literature. Michael *et. al.* proposed an MIM structure containing a combination of multi-harmonic geometries that brings together different absorption peaks from different geometries in a super cell to achieve broadband absorption [19]. However, such multi-geometric absorbers are fabricated using electron beam lithography (EBL) which is slow, expensive and applicable to small areas. Other innovations in broadband absorption include using layered tandem cell structures that are reasonably simple while fulfilling figures of merit of perfect absorbers to a large degree. Despite being lithography free, though, they require deposition of many layers which suffers from repeatability [20]. One of the broadest absorption results reported is the use of pyramid structure composed of MI layers which illustrates nearly 100 percent absorption from 1 μm to 14 μm [21]. This structure has a very broad absorption response due to the fact that the middle insulator layer is gradually changing in a pyramid which brings together the resonance of insulator layers with different thickness. Still, the fabrication of metamaterial pyramid is challenging but possible. A very simple and subtle absorber design is using thin deposited MI layers (most frequently MIMI) with lossy metals to form Fabry-Perot nanocavities that trap light. This method is lithography-free and applicable to large areas and requires rather few different types of materials to be deposited which is a reasonable trade-off between complexity of structure

and response. These structures can also exhibit extended bandwidth into mid-infrared (MIR) when the number of MI layers is increased. Not only do MIMI absorbers eradicate the need for EBL but also they outperform most of the plasmonic absorbers. One of the initial reports that attracted attention for Fabry-Perot cavity absorbers was reported by Kats et al. in which nanometer thick anti-reflection coatings (ARC) resulted in absorption in a simple two-layer structure [22]. In order to enhance the functionality of these absorbers, several metals and insulators were then utilized to get ultra-broadband perfect light absorption. These studies include W-Al₂O₃ [23], Cr-SiO₂ [24], Ag-Si [25], Ni/Ti-SiO₂ [26], Au-PMMA-Cr [27] and Cu-SiO₂ [28] multilayers. The broadest over 90% absorption is reported for an MIMI absorber with Cr-Al₂O₃ layers which is from 400 nm to 1400 nm [29]. Most of the competitive absorbers are MIMI structures which have been studied in recent years. However, these absorbers are not optimally engineered to have broadest possible absorption and material choice is an issue of study.

As discussed earlier, there are many applications for absorbers and we are interested in photocurrent phenomenon in this thesis. One of the most problematic wavelength ranges in photodetection yet quite a critical one is the NIR spectrum. There are many applications for photodetection in NIR region including space applications [30], telecommunication [31, 32], night surveillance [33], plant health monitoring [34], food analysis [35] and spectroscopy [36]. Traditional semiconductor PN photodetectors for NIR are not functional in room temperature. This stems from the fact that the suitable bandgap for a semiconductor to efficiently absorb NIR is in the order of 0.3 eV; room temperature is too hot for such a low bandgap and there will already be many free electrons and holes in conduction and valence band and the excited electrons will not make a sensible change to the concentration of free carriers. Thus, there are reports to tailor plasmonics to NIR photocurrent generation by tuning the absorption peaks to NIR wavelengths. Incident photons on the plasmonically active layer excite LSPs or SPPs and their non-radiative decay results in energetic hot electron-hole pairs (EHP) that can be harnessed as photocurrent at a proper junction like Schottky [37]. The reported designs are not tunable due to the fact that absorption and photodetection segments of the devices are the same. Therefore, freedom of engineering

optimum photodetectors with separate absorption and photocollection parts are not resolved.

1.2 Motivation and Thesis Outline

In this thesis several absorbers with capability of applications in photodetectors are studied. In chapter 2, a brief review of the absorption phenomena in different absorbers are discussed. SPPs and LSPs as well as the function of cavity absorbers are investigated and some theoretical models for further understanding of such designs are put forth.

In chapter 3, clean room facility tools that are used for the fabrication of devices are reviewed. Many physical and chemical vapor deposition techniques as well as lithography techniques are introduced. Afterwards, the characterization tools and a concise introduction into their operation theory are discussed. Moreover, simulation tools used in modeling the devices are discussed briefly.

Chapter 4 includes a brief introduction to challenges that remain unresolved in plasmonic MIM absorbers and plasmonic photodetectors. First an MIM plasmonic absorber with the capability of ultra high absorption in single layer is studied. Also, in an attempt to address some of the challenges for photodetectors, new designs and material selections for MIMIM photodetectors are proposed for broadband absorption and optimum engineering of photodetectors. The results demonstrate separated absorption and photocollection parts that can be designed with more freedom to function in desired wavelength ranges.

Chapter 5 includes a review of existing results in literature on MIMI absorbers. Then, a versatile analysis of MIMI absorbers and their operation principles follows. Afterwards, a rigorous material selection is followed to achieve broadband absorbers in VIS and NIR spectrum. The simulation, analytic and experimental results are demonstrated for the broadest MIMI absorber to the best of our knowledge.

Finally, chapter 6 includes a summary of the proposed designs and possible future work paths for loss based devices of next generation.

Chapter 2

Theory and Methods

As discussed earlier in the introduction section, absorbers and photodetectors are the backbone of many applications. In this chapter, the theory and working principle of absorbers and photodetectors are discussed with information on methods to analyze them. First a glance at the stance of plasmonics is provided in the optical material classifications.

Plasmonics can be considered a subcategory of metamaterials. “Meta” means “beyond” in Greek vocabulary and refers to materials that do not exist naturally. Metamaterials are those materials that are fabricated so that they can reveal extraordinary properties that do not exist in natural materials. In other words, metamaterials are artificially fabricated materials with layers combined in unit cells smaller than the wavelength of interest, so that the total material can be approximated as an effective single metamaterial than the constituent materials. Since the inhomogeneity in metamaterials is much smaller than the wavelength of interest, their electromagnetic response can be expressed in terms of homogenized single materials [38]. Many extraordinary effects such as negative index of refraction [39, 40], optical magnetism [41], giant artificial chirality [42], nonlinear optics [43], super resolution [44, 45] and electromagnetic cloaks of invisibility [46, 47].

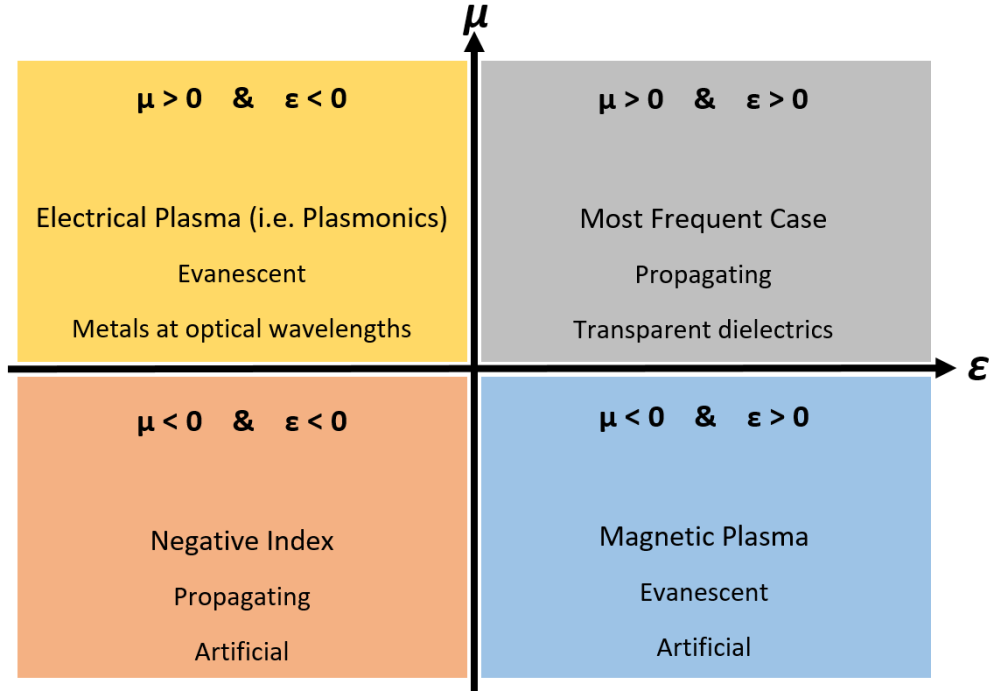


Figure 2.1: Classification of metamaterials with respect to their optical parameters.

In photonics, a material is described with two electromagnetic parameters; permittivity (ϵ) and permeability (μ). Figure 2.1 illustrates the classification of metamaterials. In this figure, the horizontal and vertical axes represent permittivity and permeability, respectively, where the positive halves of axes are designated to be positive where the other halves are negative. As it is illustrated in Fig. 2.1, the second medium is frequently referred to as “plasmonics”. Plasmonics are a major part of the works that will be discussed in this thesis and the main focus will be on the lossy behavior of these structures. In the upcoming discussions, it will be assumed that the materials that are dealt with are non-magnetic and thus $\mu = \mu_0$ for all materials.

2.1 Absorption

In this section absorption phenomena are discussed with the focus on pointing out different absorption mechanisms like direct bandgap absorption and plasmonic absorption. It is worth pointing out that some methods of absorption like excitonic absorption is not within the scope of this thesis and are not discussed. The figures of merit for a good absorber are:

- Near 100% absorption
- Broad band absorption
- Polarization insensitivity
- Incident angle insensitivity
- Small dimensions and thickness.

2.1.1 Optical absorption

In this subsection, some of the major optical absorption mechanisms that involve exciting electrons to conduction band and holes to valence band will be discussed. In terms of bands, there are two types of absorptions, interband and intraband absorption. The former refers to the excitation of an electron from valence to conduction band while the latter refers to excitation of electrons or holes to higher states within the same band. This subsection is devoted to interband transition phenomena which takes place when a photon with an energy more than the bandgap of the semiconductor reaches it and excites an electron from conduction to valence band leaving behind a hole (EHP). In order for absorption to take place momentum and energy conservations should hold. Density of states in a semiconductor crystal is calculated using Kronig-Penney model which gives the E-k diagram also commonly referred as “energy band diagram” which dictates electron transition to higher states (optical absorption). An E-k diagram for a

direct bandgap semiconductor is illustrated in Fig. 2.2. Direct bandgap semiconductors are those where the minimum of conduction band and the maximum of the valence band happen at the same k value like Ge [48]. The absorption in tandem cell absorbers work on the principles of absorption methods in optical absorption section which are bulky and usually have thicknesses on the order of several μms .

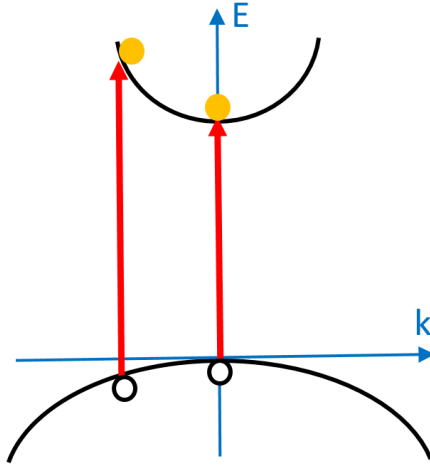


Figure 2.2: E-k diagram of a direct bandgap semiconductor with two transitions illustrated with red arrows.

In an E-k diagram of valence and conduction bands, a transition of electron to an upper state (or analogously, a hole to a higher state, where higher state for a hole means lower in the E-k diagram representation) is only possible when a photon with enough energy and a state with conserved momentum value exist:

$$E_2 = E_1 + E_{\text{photon}} \quad (2.1)$$

$$k_2 = k_1 + k_{\text{photon}} \quad (2.2)$$

The density of states is calculated using the Bloch theorem which states that the edges of Brillouin zone are $\frac{\pi}{a}$ where a is the unit cell of the material crystal in the order of 0.5 nm. The momentum value for photons in the VIS and NIR region is in the order of $\frac{\pi}{1000\text{nm}}$ ($k_{\text{photon}} = 2\pi/\lambda$). Since the momentum of Brillouin zone edge is $\frac{\pi}{0.5\text{nm}} \gg k_{\text{photon}}$, Eq. 2.2 boils down to

$$k_2 = k_1 \quad (2.3)$$

In other words, the momentum of photon is approximately zero and the electron-hole transitions are vertical.

2.1.1.1 Direct Absorption

Direct absorption could take place in direct or indirect bandgap semiconductors. In this type of absorption a photon with sufficient energy pushes an electron to conduction band leaving a hole behind in the valence band. This mechanism is dominant and most probable one in most of the conventional absorbers and photovoltaic devices. Figure 2.3a illustrates direct absorption in an indirect bandgap semiconductor like Si.

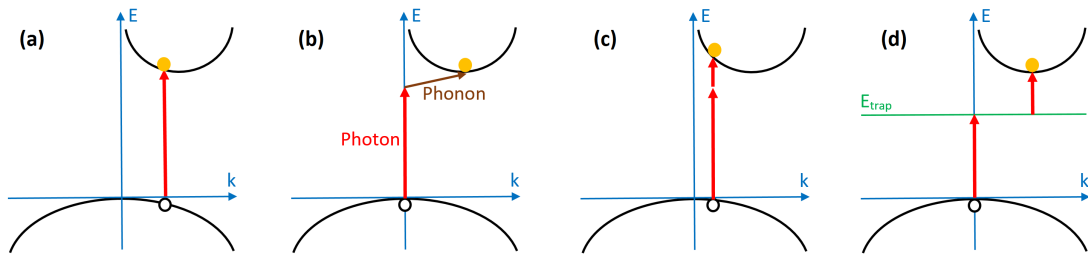


Figure 2.3: (a) Direct, (b) phonon assisted, (c) two photon and (d) trap assisted absorption.

2.1.1.2 Phonon Assisted Absorption

This mechanism happens when the photon reaching to the electrons in the valence band is not energetic enough for indirect bandgap semiconductor electron excitation. Therefore, there must be a particle with high momentum to compensate the momentum difference to lead to interband transition. This is sometimes achieved when a phonon reaches the particle at the same time as the low energy photon does (Fig. 2.3b). This kind of absorption is generally discussed in indirect bandgap semiconductors, but is possible in both direct and indirect bandgap

ones. However, since there is the necessity of simultaneously arriving phonons and photons, this method is rare and has low probability [49]. .

2.1.1.3 Two Photon Absorption

In this type of absorption, two photons that add up to the required energy difference needed for transition, simultaneously reach to electrons [50]. This method also happens with low probability and is possible in direct or indirect bandgap semiconductors (Fig. 2.3c).

2.1.1.4 Trap Assisted Absorption

Trap assisted absorption is probable when there are traps in the bandgap of semiconductors. Position and momentum spaces are reciprocal spaces meaning that there is inverse Fourier relation between these two spaces. Localized traps are prevalent in semiconductors due to extrinsic atom defects (*i.e.*, impurities) or crystal defects. These states are quite broad in momentum space which support a wide range of momentum values. Thus, they are stable and electrons (or holes) can remain in these states by absorbing one photon and waiting for another proper photon to complement the interband transition which is depicted in Fig. 2.3d. There is another absorption phenomenon similar to trap assisted absorption which is called surface state absorption. The crystal periodicity is generally assumed to be infinite; however, there are unterminated bonds also known as “dangling bonds” and “surface states” that exist on the surface and edges of semiconductors. They behave analogous to traps in terms of absorption. One similar phenomenon exists in layered materials where there exist “interface states”. These mechanisms are more probable than other ones and are sometimes comparable to direct absorption due to their stable nature [51]. The trap assisted absorption happens in both direct and indirect bandgap semiconductors.

2.1.2 Plasmonic Absorption

In this section plasmonic theory as well as its affiliated absorption mechanism will be discussed. Plasmonics deals with the study of light-matter interaction in dimensions comparable or smaller than the wavelength of the incident light. In conventional electromagnetics, metals are considered perfect conductors and a finite conductivity is defined to make the study more accurate. However, since the penetrated electromagnetic waves into the metal are not negligible for frequencies below far-infrared regime, this model will no longer be valid. In VIS and NIR spectrum of the electromagnetic radiation, the penetration of electromagnetic waves into the metals is substantial and even at ultraviolet frequencies, metals behave like dielectrics and allow propagation of electromagnetic waves with attenuation. Metals are modeled such that their conduction and valence bands interfere giving rise to high population of loosely bound electrons called “free electrons”. Electrons in the metal resonate in response to the driving electromagnetic waves. The resulting resonance is called “plasmon resonance” and the quanta of these oscillations is called a “plasmon”. A Plasmon in fact is a quasi-particle associated with plasma oscillations (similar to its mechanical vibration counterpart *i.e.*, a phonon).

2.1.2.1 Bulk Plasmons

As a reasonable approximation, free electron plasma is assumed to play the role of free electrons in metals. In this model, the interaction of electrons with each other as well as bound electron effects are neglected and the oscillator equation (*a.k.a.*, Drude model) is solved for free electrons. However, in optical frequencies where happen to be near the plasma frequency of metals, the Drude model has significant deviations and the effect of bound electrons in d-band of the metals should be considered. Therefore, Lorentz-Drude oscillator model which incorporates a damping factor (γ) is more reliable [52]

$$m \frac{d^2 \bar{r}}{dt^2} + m\gamma \frac{d\bar{r}}{dt} + m\omega_0^2 \bar{r} = -e\bar{E} \quad (2.4)$$

In this equation, e , m , \bar{r} and \bar{E} ($\bar{E} = E_0 e^{-j\omega t}$) refer to charge, effective mass, position of electrons and electric field acting on electrons respectively. ω_0 represents the oscillation frequency of the bound electrons under applied electric potential. Assuming a solution of the form $\bar{r}(t) = r_0 e^{-j\omega t}$ for the position variable, it can be determined as

$$\bar{r}(t) = \frac{e}{m(\omega^2 - \omega_0^2 + j\gamma\omega)} \bar{E}(t) \quad (2.5)$$

The polarization of metal is equal to the total dipole moment ($\bar{P} = -ner$). Considering Eq. 2.5 together with the relations $\bar{P} = \epsilon_0 \chi \bar{E}$ and $\epsilon = 1 + \chi$, the permittivity (ϵ) can be found and decomposed into its real and imaginary parts explicitly:

$$\epsilon(\omega) = 1 + \frac{\bar{P}}{\epsilon_0 \bar{E}} = 1 + \frac{\omega_p^2}{\omega_0^2 - \omega^2 - j\gamma\omega} \quad (2.6)$$

$$\epsilon'(\omega) = 1 + \frac{\omega_p^2(\omega_0^2 - \omega^2)}{(\omega_0^2 - \omega^2)^2 + \gamma^2\omega^2} \quad (2.7)$$

$$\epsilon''(\omega) = \frac{\omega_p^2\gamma\omega}{(\omega_0^2 - \omega^2)^2 + \gamma^2\omega^2} \quad (2.8)$$

where $\omega_p = \sqrt{ne^2/\epsilon_0 m}$ is defined as the volume plasmon angular frequency of the metal of interest and $\epsilon(\omega) = \epsilon'(\omega) + j\epsilon''(\omega)$. At frequencies lower than the ω_p waves will be attenuated and as a result will propagate within only a few skin depths. On the other hand, At frequencies higher than ω_p which is called the “plasmonic band”, the permittivity will be positive and the metals will act like dielectrics. If we use lossless Drude model for the a metal ($\epsilon(\omega) = 1 - \frac{\omega_p^2}{\omega^2}$), using the dispersion relation of transverse waves $k^2 = \epsilon(\omega) \frac{\omega^2}{c^2}$, the dispersion relation for bulk plasmons is calculated as

$$\omega = \sqrt{\omega_p^2 + c^2 k^2} \quad (2.9)$$

Since it is difficult to directly excite bulk plasmons and there is a bottleneck in momentum matching, volume plasmons are rarely the intention of devices engineered to be absorbers.

2.1.2.2 Surface Plasmon Polaritons and Surface Plasmons

SPPs are surface waves that propagate in the interface of a metal and dielectric if the incident light is properly coupled to them, which means that the momentum

and energy conservation is fulfilled. SPPs are generated as a result of coupling of electromagnetic radiation to conduction electrons of metals in the interface. SPPs which are quasiparticles bridging the phenomenon between the incident light and the propagating waves. SPs have high momentum values and are more localized versions of SPPs and they mark the highest frequency and momentum that SPPs can achieve. SPPs usually happen at frequencies smaller and close to SP resonances. If Maxwell's equations are solved for a structure containing a boundary between a metal and a dielectric, surface waves can be excited with propagation constant. These waves are called SPPs. As mentioned earlier, the momentum of photons is very small and SPPs are need higher momentum. As a result, SPPs cannot be excited by direct illumination. One primitive method such as Kretschmann setup is using high-index medium to excite SPPs in the interface of a metal and the low-index medium. This surface wave is highly decaying inside both the adjacent media and it propagates solely in the interface. In Fig. 2.4a, the x-direction is considered to be the direction of propagation and there is no variation of fields in the z-direction. Solving the Maxwell's equations for the

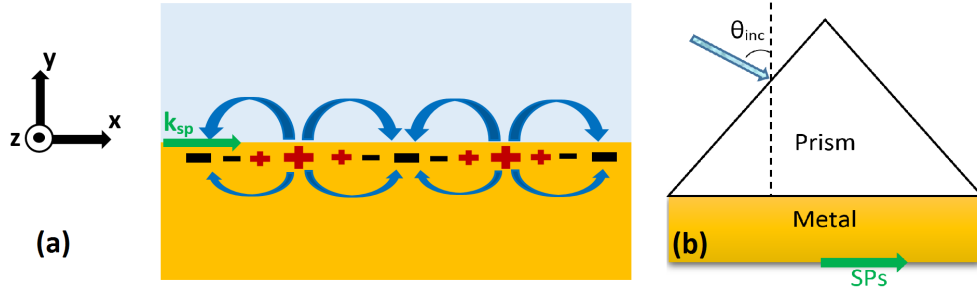


Figure 2.4: (a) Schematic of the SPPs and the geometry of solving Maxwell's equations and (b) Kretschmann configuration for SPP excitation.

structure in Fig. 2.4a will yield the criterion for SPP excitation. The solution for TE and TM waves lead to the fact that only TM polarization will be capable of exciting SPPs and the application of boundary conditions leads to

$$\frac{k_m}{k_d} = -\frac{\epsilon_m}{\epsilon_d} \quad (2.10)$$

$$k_{sp} = \frac{\omega}{c} \sqrt{\frac{\epsilon_m \epsilon_d}{\epsilon_m + \epsilon_d}} \quad (2.11)$$

where m and d in the subscripts stand for metal and dielectric. It can be inferred from Eq. 2.10 that there is a negative relation between permittivities of the media in contact with each other which means that a material with negative permittivity (*i.e.*, metal) should be in contact with a normal dielectric. Equation 2.11 shows the dispersion relation of SP(P)s and indicates that the dielectric material can be altered to tune the SPP resonance. In order for a solution to exist, the dispersion relation of SPPs and the incident light should somehow be matched. This has been conventionally achieved using Kretschmann (Fig. 2.4b) [53] and Otto [54] configurations where a high-index prism is used to support the momentum matching condition. In Kretschmann structure, if the dielectric material of prism is chosen appropriately, there is a minimum incident angle above which the x-component of the k vector will be large enough to support SPPs.

$$\theta_{inc} > \theta_c = \sin^{-1} \left\{ \frac{1}{n_p} \left(\sqrt{\frac{\varepsilon_m}{\varepsilon_m + 1}} \right) \right\} \quad (2.12)$$

In Eq. 2.12, $\varepsilon_d = 1$ which denotes air and n_p is the refractive index of the prism. Moreover, the metal should be thin enough such that the excited highly decaying wave in the prism/metal interface couples to the metal/air interface where SPPs can be propagating waves.

In order to find the SPP resonance frequency, we can let $k_{sp} \rightarrow \infty$. In other words, from Eq. 2.11 it is dictated that $\varepsilon_m = -\varepsilon_d$. Using lossless Drude model approximation for the metal ($\varepsilon = 1 - \frac{\omega_p^2}{\omega^2}$) we can solve for SPP resonance frequency

$$\varepsilon_m = 1 - \frac{\omega_p^2}{\omega_{sp}^2} = -\varepsilon_d \Rightarrow \omega_{sp} = \frac{\omega_p}{\sqrt{1 + \varepsilon_d}} \quad (2.13)$$

The dispersion relation of excitation from a high-index medium case is illustrated in Fig. 2.5b for a schematic like Fig. 2.5a. As it can be inferred from this figure, there is no intersection (match) between the tangential- k dispersion relation of light ($\omega = ck/\sin \theta$) and that of SP(P)s. However, when incident from high-index medium, as illustrated in Fig. 2.5a, the wave is slower ($\omega = ck/\sqrt{\varepsilon_d} \sin \theta$) and there is an intersection to excite SPPs in the interface of air (low-index medium) and metal. The excitation is fulfilled when the incident light excites an evanescent wave from the interface of the metal and high-index medium downwards. If the metal is thin enough, this wave would couple to SPPs in the bottom interface as illustrated in Fig. 2.5a. It should be mentioned that the calculated resonance is for

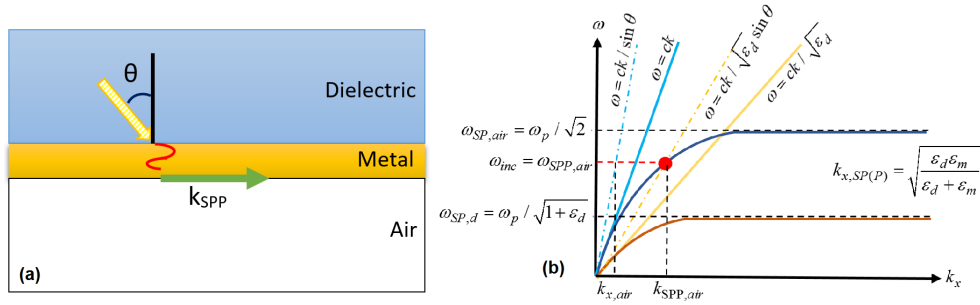


Figure 2.5: (a) Schematic of the SPPs excitation from high-index medium and (b) Dispersion relation for SPP excitation from high-index medium.

loss-less case and it assumes that k is infinite. This would mean that if we had a plasmonic lens, we would resolve infinitely small objects. This arises from the fact that the smallest resolution is $\lambda/2$ and λ approaches zero (since $k = 2\pi/\lambda$)! Obviously, this is not feasible. Therefore, in a more realistic case where the loss and damping is not overlooked for metals, there will be a higher order limit for momentum. This relation can be found in reference number [52] which is beyond the scope of this thesis. Despite sustaining SPPs and having freedom of engineering, Kretschmann and Otto structures are considered obsolete due to being bulky and difficult to fabricate. Also, the high-index medium setup provides single-wavelength matching which is limiting. The high demand of decreasing size of photonic devices and the advent of techniques such as EBL have motivated scientists to look for nanoscale alternatives. One of the most successful structures are gratings or nanoislands [55] that are vastly used nowadays. Since gratings have very sharp edges in position space and are periodic, due to reciprocity, they can support a wide range of momentum values and are thus quite effective in SPP excitation. The dispersion relation for a grating can be written as [52]

$$k_{||,Air} = k_{sp} + mG \quad (2.14)$$

where $k_{||,Air} = k_{inc} \sin(\theta_{inc})$, $m = 1, 2, \dots$ is the order of grating and $G = 2\pi/P$ where P is the periodicity of grating. Besides, k_{sp} is the same as Eq. 2.11. The structure is illustrated in Fig. 2.6a and the dispersion relation is sketched in Fig. 2.6b in which the yellow arrow shows the amount of compensation of momentum by grating.

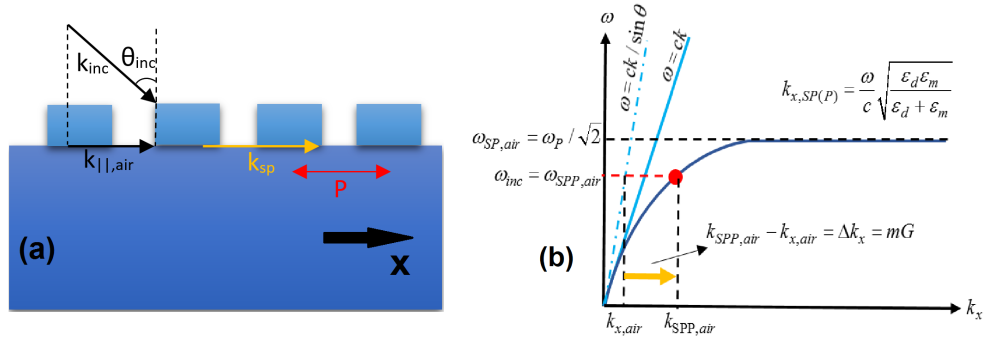


Figure 2.6: (a) Schematic of the SPP excitation using grating structure and (b) dispersion relation in gratings.

2.1.2.3 Localized Surface Plasmons

Metallic nanoparticles can provide conditions for the excitation of non-propagating SPPs commonly referred to as LSPs. Analogous to SPPs, LSPs are excited in the metal/dielectric interface. Unlike the SPPs, LSPs can be excited under direct illumination without the need for any matching setup. Since particles are smaller than or in the order of the wavelength of interest, size of the nanoparticles is vital and the equation for LSPs comes with size parameters. First, assume a small nanoparticle which is one tenth in size compared to the wavelength of illumination where the E-field will be approximately constant through the nanoparticle which is illustrated in Fig. 2.7a. This approximation is known as quasi-static approximation. Assume that there is a medium as shown

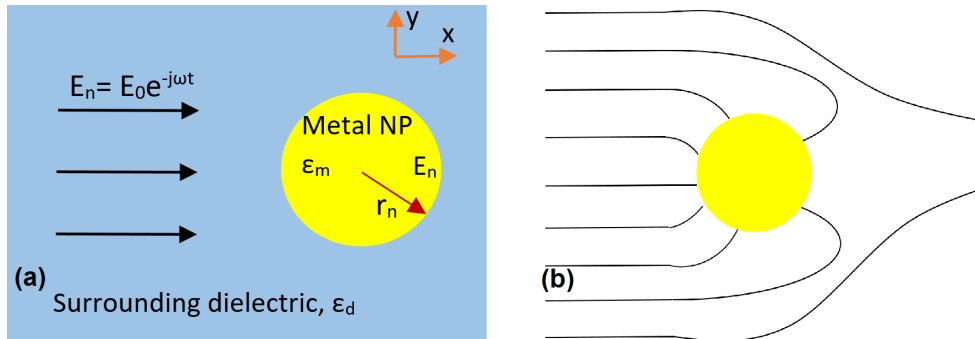


Figure 2.7: (a) Metallic nanoparticle under illumination in quasi-static approximation and (b) increased absorption cross section in resonance.

in Fig. 2.7a. Also, a monochromatic light with an E-field oscillating in the y-direction in the form of

$$\bar{E}_{inc}(t) = \text{Re} \left\{ \hat{a}_y E_0 \exp(-j\beta x - \frac{\alpha}{2}x + j\omega t) \right\} \quad (2.15)$$

is illuminating the particle where $\beta = k_0 n'$ and $\alpha = -2k_0 n''$. It is also assumed that the incident light induces dipole moment ($p_y(t)$) in y-direction in the vicinity of particle surface. The affiliated potential in the vicinity of particle surface is $\varphi_{inc} = -E_0 e^{j\omega t} y + \frac{p_y \cdot r}{r^3}$ where the center of spherical coordinate system is designated to be the middle of the metallic nanoparticle. The potential inside the nanoparticle is $\varphi_n = -E_n(t)y$. Solving for E-field using the well known boundary conditions for electric field and electric flux density, the electric field and the dipole moment can be explicitly found as

$$\bar{E}_n(t) = \hat{a}_y \frac{3\varepsilon_d}{\varepsilon_n + 2\varepsilon_d} E_0 e^{j\omega t} \quad (2.16)$$

$$p_y(t) = \frac{\varepsilon_n - \varepsilon_d}{\varepsilon_n + 2\varepsilon_d} r_n^3 E_0 e^{j\omega t} \quad (2.17)$$

These equations show that the resonance of dipole moment happens when

$$\text{Re}\{\varepsilon_n\} = -2\varepsilon_d \quad (2.18)$$

which is known as Frölich condition [52]. If Frölich condition is met, the nanoparticle will show a peak of absorption and increased effective absorption cross section as illustrated in Fig. 2.7b. This figure also shows the exceptional capability of nanoparticles in confining light which are the main property of interest in plasmonics. Similar to SPPs, Eq. 2.18 vindicates the property of tuning the LSP resonance by the surrounding dielectric material choice. Assuming drude model for the metal, the LSP resonance frequency is found as:

$$\varepsilon_m = 1 - \frac{\omega_p^2}{\omega_{LSP}^2} = -2\varepsilon_d \Rightarrow \omega_{LSP} = \frac{\omega_p}{\sqrt{1 + 2\varepsilon_d}} \quad (2.19)$$

If the nanoparticle is extremely small ($r_n < 10nm$), there will be high damping arising from the bound electron oscillation to the boundaries of the nanoparticle. In this case, $\omega_{LSP} = \frac{A\nu_F}{r_n}$ where ν_F is the Fermi velocity in the metal and A is the proportionality factor [56]. On the other hand, if the particle size is big enough

to violate the uniformity of E-field inside the particle and as a result the quasi-static approximation, then the expansion of the first TM mode of Mie theory gives dipole moment as

$$P_n = V \frac{1 - \frac{\epsilon_n + \epsilon_d}{10} + O(x^4)}{\frac{1}{3} + \frac{\epsilon_n}{\epsilon_d - \epsilon_n} - \frac{\epsilon_d + 10\epsilon_n}{30} x^2 - j \frac{4\pi\epsilon_n^{3/2} V}{3\lambda_0^3} + O(x^4)} E_0 \exp(-j\omega t) \quad (2.20)$$

where $x = \frac{\pi r_n}{\lambda_0}$ is a size factor and V is the particle volume [57].

LSPs are highly size dependent and there are a large number of publications dedicated to different size effects in metallic nanoparticles, nanoislands, nanorods and other more sophisticated shapes. In nanorods, for example, a variety of LSP resonance peaks can be excited in longitudinal and latitudinal axes of the nanorods using different illumination polarizations [58].

2.1.2.4 SP and LSP Absorption

The most notable structures for plasmonic absorption are MIM structures composed of a back reflector metal, a dielectric spacer in the middle and a plasmonic metal layer which can be in the form of grating, nanoparticles, nanopyramids, etc. A simple grating structure is illustrated in Fig. 2.8a consisting of thick Al, 40 nm Al_2O_3 and Al grating with periodicity of 500 nm, thickness of 50 nm and width of 100 nm. In order to give insight to the working principle of these absorbers a grating based MIM structure is calculated using a commercial-grade simulator based on the finite-difference time-domain method [59]. Since the back reflector is optically thick, there is no transmission through the structure, $A = 1 - R - T = 1 - R$. The total absorption result in the MIM plasmonic cavity is sketched versus wavelength for VIS and NIR in Fig. 2.8b. Moreover, the absorption in bottom metal and the grating layer are sketched in Fig. 2.8b which add up to from the total absorption. There are two peaks in the total absorption curve each comprised of LSP and SPP resonances. As proved earlier in Eqs. 2.13 and 2.19, in each absorption peak, LSP resonance absorption peak happens at lower frequency (*i.e.*, higher wavelength) compared to SPP resonance. Therefore the first peak of absorption is at lower wavelengths that is the resonance with a dielectric constant

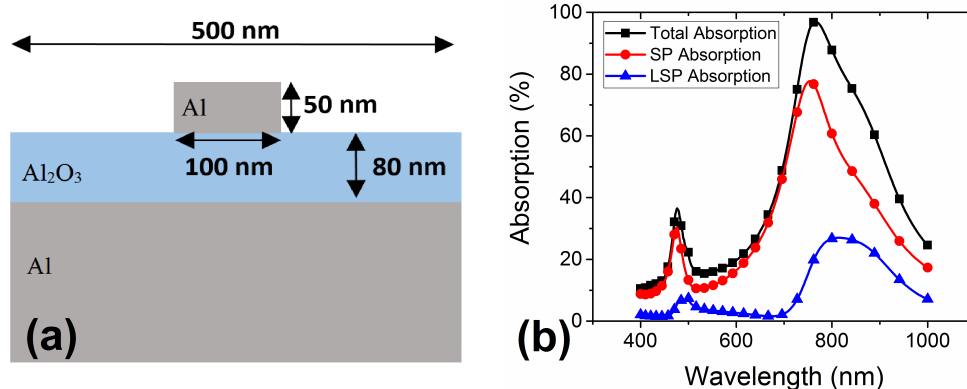


Figure 2.8: (a) Schematic of the test MIM structure and (b) absorption vs wavelength in VIS and NIR spectra with designation of LSP and SP peaks.

of aluminum oxide and the bottom metal in the cavity which stands for SPP resonance. The higher peak on the other hand is the LSP resonance of the structure as pointed out in Fig. 2.8b which is the resonance of the grating structure. There are two peaks in the results; the higher wavelength resonance is the fundamental mode of the structure and the lower one is a higher order mode. The broad plasmonic MIM absorbers are designed by bringing together these two peaks close to each other. A well-known method for having broadband absorption is using lossy metal as the bottom metal at higher wavelengths and using gold nanoparticles which has loss in lower VIS wavelengths (this is obvious from the color of gold!). In order to further elucidate the absorption phenomenon, Fig. 2.9 can be considered. Figure 2.9a and Fig. 2.9b illustrate the electric field magnitude at the first (483 nm) and second (763 nm) resonance wavelengths respectively. Note that the E-field magnitude shows higher order mode excitation in lower wavelength. The lower and higher wavelength resonances are also known as bright and dark plasmonic modes respectively. It can easily be deduced from Fig. 2.9a and Fig. 2.9b that the resonance at 763 nm stands for the fundamental mode with dipole-like excitation and the resonance at 483 nm resembles quadrupole-like excitation. Moreover, the simulated Poynting vector magnitude for the first peak comprised of SPP resonance at 476 nm and LSP resonance at 500 nm are illustrated in Fig. 2.9c and Fig. 2.9d respectively. Scrutinizing the Poynting vector magnitude contour plots reveal that at 476 nm, there is strong coupling of light to the SPPs which is a propagating wave and thus the Poynting vector magnitude

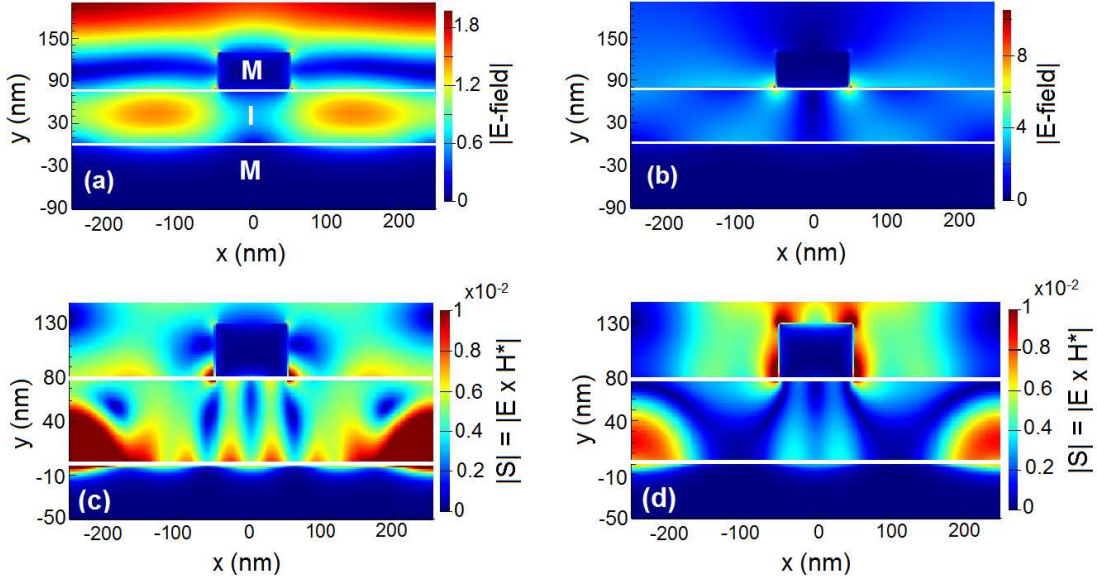


Figure 2.9: E-field magnitude in a cross section of the structure at (a) higher order resonance 483 nm and (b) fundamental resonance 763 nm, the simulated Poynting vector magnitude (for the first peak of 463 nm) in the structure at (c) SPP resonance of 476 nm and (d) LSP resonance of 500 nm. The white lines mark the boundaries of the three layers of the MIM.

at this wavelength resembles the sketched schematic in Fig. 2.4a. The light is mainly concentrated inside the cavity in the bottom Al/Al₂O₃ interface which excites SPPs. At 500 nm on the other hand, the SPP coupling gradually dies out and gives way to strong concentration of light around the grating and thus excites LSPs. Since the situation is quite similar for the fundamental mode at 763 nm, the same discussion also applies for it and the results for this resonance is avoided in favor of avoiding redundancy. If designed such that all these peaks come together, one would obtain a broadband plasmonic absorber.

Plasmonic absorption in MIM structures is highly geometry and design sensitive and there are a myriad of publications on different structures. For example, using a higher index dielectric or decreasing the thickness of the dielectric would push both SPP and LSP plasmon resonances to higher wavelengths. Also, increasing the width of the grating while keeping the periodicity fixed, would red-shift the absorption resonance peaks as a result of higher dipole moment oscillation possible in such case. The resonant behavior in this plasmonic cavity can be

described as

$$w \frac{2\pi}{\lambda} n_d = m\pi - \varphi \quad (2.21)$$

where w is the width of the grating, λ the free space wavelength, n_d the refractive index of the spacer dielectric, φ the phase shift acquired by the reflections from the resonator terminations and m stands for the mode of the resonance while $m=1$ being the fundamental mode [60].

2.1.3 Cavity Absorption

Cavities are very important in many microwave and optical applications like lasers. Cavities are formed by a lossless dielectric medium sandwiched between two reflectors. One of the main figures of merit for a cavity is quality factor which is defined as the ratio of the stored power to the power loss in the reflector walls. If Q_c is the quality factor due to the conductivity loss of reflectors and Q_d the quality factor due to the loss happening in dielectric, the general quality factor Q of a cavity is defined as [61]

$$Q = \left(\frac{1}{Q_c} + \frac{1}{Q_d} \right)^{-1} \quad (2.22)$$

Though a high quality factor is always pursued in many applications, in cavity absorbers low quality factor is a figure of merit. In other words, the metals should be lossy so that the light is trapped and dissipated in the metals in order to annihilate reflection. The most studied structures in literature for low quality factor absorbers are MIMI absorbers as illustrated in Fig. 2.10. In these absorbers, the top dielectric acts as an anti reflection coating (ARC) and reduces reflection. Afterwards, the middle thin metal is very thin (on the order of 10 nm) which absorbs part of the light and lets it pass partially. The transmitted light will be trapped in the cavity between the thin metal and the bottom reflector metal and will decay in these metals after several back and forth travels. Bottom metal is optically thick and the transmission vanishes as a result. Despite being very thin, the middle metal blocks the reflected light from bottom metal due to the fact that its intensity is highly reduced and will not make it through thin metal

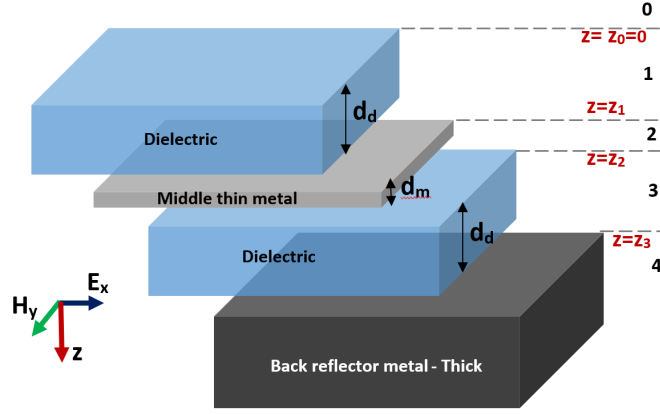


Figure 2.10: Schematic of the MIMI cavity absorber.

to air.

In order to analyze such a multi layer structure, transfer matrix method (TMM) is beneficial next to simulation. As mentioned before, we have thick bottom reflector metal; therefore, the transmission (T) vanishes and the absorption (A) boils down to $A = 1 - R - T = 1 - R$ where R stands for reflection. We will use the notation illustrated in Fig. 2.10 and assume a TE polarized incident light. The incident light can also be assumed a TEM wave since we discuss normal incidence only. For each layer in MIMI structure, d_i , $\gamma_i = \alpha_i + j\beta_i = j\omega\sqrt{\mu_i\varepsilon_i}$, μ_i and ε_i ($i=0, 1, 2, 3, 4$) represent the thickness, complex propagation constant, complex permeability and complex permittivity of each layer while ω stands for angular frequency. It can be assumed that there exists a solution with total forward and backward propagating electromagnetic waves for each layer of the form

$$\bar{E}_{y,i} = A_i e^{-\gamma_i z} + B_i e^{+\gamma_i z}, \bar{H}_{x,i} = \frac{1}{j\omega\mu_i} \frac{\partial \bar{E}_{y,i}}{\partial z} \quad (2.23)$$

where A_i and B_i are amplitude constants. Maxwell's boundary conditions enforce that tangential electric and magnetic fields (\bar{E}_y , \bar{H}_x) are equal at all the boundaries between any two adjacent layer ($\bar{E}_{y,i}|_{z=z_i} = \bar{E}_{y,i+1}|_{z=z_i}$, $\bar{H}_{x,i}|_{z=z_i} = \bar{H}_{x,i+1}|_{z=z_i}$). Solving for all four layers a general matrix relation between two adjacent layers can be derived as

$$\begin{pmatrix} A_i \\ B_i \end{pmatrix} = (M_i)_{2 \times 2} \begin{pmatrix} A_{i+1} \\ B_{i+1} \end{pmatrix} \quad (2.24)$$

$$(M_i) = \begin{pmatrix} \frac{1}{2} \left[1 + \frac{\gamma_{i+1} \mu_i}{\gamma_i \mu_{i+1}} \right] e^{(\gamma_{i+1} - \gamma_i) z_i} & \frac{1}{2} \left[1 - \frac{\gamma_{i+1} \mu_i}{\gamma_i \mu_{i+1}} \right] e^{-(\gamma_{i+1} + \gamma_i) z_i} \\ \frac{1}{2} \left[1 - \frac{\gamma_{i+1} \mu_i}{\gamma_i \mu_{i+1}} \right] e^{(\gamma_{i+1} + \gamma_i) z_i} & \frac{1}{2} \left[1 + \frac{\gamma_{i+1} \mu_i}{\gamma_i \mu_{i+1}} \right] e^{-(\gamma_{i+1} - \gamma_i) z_i} \end{pmatrix} \quad (2.25)$$

Since the transmission is zero, the ratio of $R = |A_0/B_0|$ would give absorption ($A = 1 - R$) in the structure. The total equation linking the air layer to the bottom reflector metal layer will be

$$\begin{pmatrix} A_0 \\ B_0 \end{pmatrix} = (M_0) (M_1) (M_2) (M_3) \begin{pmatrix} A_4 \\ B_4 \end{pmatrix} \quad (2.26)$$

Assuming that $B_4=0$ as a result of zero backward propagating wave in the bottom reflector metal, the absorption can be calculated explicitly [62].

Another important method for studying multilayer structures and absorbers in general, is the impedance transfer method which can give equivalent impedance of the structure. If this impedance is matched to that of air, perfect coupling and absorption will result. This method can be used to extract ideal permittivity values of any layer designated to be unknown which is a significant method in material optimization process. For example, as will be discussed in MIMI absorbers in chapter 5, if we assume that the bottom reflector metal is unknown and all other layers are known in terms of material and thickness, the total normalized (to the free space wave impedance) wave impedance at the first interface of the structure (the interface where the light impinges the structure) can be calculated. In order to fulfill this, the TMM relation of Eq. 2.26 can be calculated. Then, the electric and magnetic fields are evaluated at $z=0$ boundary using A_0 and B_0 constants. The ratio of electric to magnetic field normalized to the free space wave impedance gives the equivalent wave impedance Z_T of the structure as

$$Z_T = \frac{|E_y|}{|H_x|} / \sqrt{\frac{\mu_0}{\epsilon_0}} \quad (2.27)$$

Calculation give Z_T as [28, 29]

$$Z_T = \frac{A_1 + A_2 n_R}{B_1 + B_2 n_R} \quad (2.28)$$

where

$$A_1 = n_d n_m \tan^2(\varphi_d) + n_d n_m \varphi_m (n_d^2 + n_m^2) - n_d^2 n_m \quad (2.29)$$

$$A_2 = -j n_m^2 \varphi_m \tan^2(\varphi_d) + j 2 n_d n_m \tan(\varphi_d) - n_d^2 \varphi_m \quad (2.30)$$

$$B_1 = -jn_d^4\varphi_m \tan^2(\varphi_d) + j2n_d^3n_m \tan(\varphi_d) + jn_d^2n_m^2\varphi_m \quad (2.31)$$

and

$$B_2 = n_d^2n_m \tan^2(\varphi_d) + n_d\varphi_m(n_d^2 + n_m^2) \tan(\varphi_d) - n_d^2n_m \quad (2.32)$$

In these equations, subscript R , m and d stand for back reflector metal, middle thin metal and dielectric parameters. $\varphi_i = j\gamma_i d_i$ represents the phase shift coming from each layer and γ , d and n are the complex propagation constant, thickness and complex refractive index of layers, respectively. In order to simplify the derivation of Eq. 2.28, it is assumed that $\varphi_m = j\gamma_m d_m \ll 1$ due to very thin layer of middle metal in MIMI structures which leads to $\tan(\varphi_m) \approx \varphi_m$. Applying $Z = 1$ condition on Eq. 2.28 to match the equivalent wave impedance of the structure to that of free space and considering optimum thicknesses and material parameters for the other three layers, it is possible to obtain the ideal refractive index (n_R) of the optically thick bottom layer that we assumed to be unknown. This method yields a versatile approach to define optimum materials.

2.2 Photodetection

Photodetection is the conversion of photons into electric current which has many applications as discussed in Background section of chapter 1. The process of photodetection is completed in three steps [63]:

1. Absorption of photons by the structure.
2. Generation of hot EHPs.
3. Collection of electrons or holes with applied voltage to generate photocurrent.

There are some terms and definitions for photodetectors some of which are covered concisely here.

Dark current. In order to collect energetic EHPs, a reverse DC bias should be applied to generate required E-field. The DC current that flows in the absence of optical signal is called dark current which increases power loss and therefore is desired to be low.

Photoresponsivity. Photoresponsivity or more accurately, spectral photoresponsivity ($R(\lambda)$), is defined as the ratio of the photocurrent (I_p) to the incident optical power (P_{op}) and is a measure of the efficiency of a photodetector. It is frequently discussed as a function of wavelength and is desired to be high:

$$R(\lambda) = \frac{I_p(\lambda)}{P_{op}(\lambda)} \quad (2.33)$$

Quantum efficiency. If there is no gain mechanism in the structure, which is the case in photodetectors generally, there is a maximum limit for photoresponsivity at a particular wavelength. This arises from the fact that a limited number of photons take part in EHP excitation and from those excited, a limited number contribute to photocurrent. Thus,

$$R_{\max}(\lambda) = \frac{n_e(\lambda)q/t}{n_p(\lambda)hv/t} \quad (2.34)$$

Quantum efficiency (QE) is defined (η) as the ratio of the number of photogenerated electrons (or holes) to the number of the incident photons:

$$\eta(\lambda) = \frac{n_e(\lambda)}{n_p(\lambda)} \quad (2.35)$$

By this definition, it is possible to calculate QE experimentally using Eqs. 2.34 and 2.35 as [64]

$$\eta(\lambda) = \frac{hcR(\lambda)}{q\lambda} \quad (2.36)$$

Response time. In some application such as communications, response speed of a photodetector is critical. It is defined as the maximum optical signal frequency that can be detected. Response time is highly affected by the decay time of EHPs as well as carrier kinetics in the photodetector.

The figures of merit for a good photodetector are:

- Low dark current

- Low bias voltage
- High spectral photoresponsivity and quantum efficiency
- Low response time
- Small dimensions and thickness.

Some of the NIR photodetector structures will be discussed concisely in this section.

2.2.1 PIN photodetectors

PIN photodetectors are enhanced versions of PN photodetectors which can be considered the earliest developed structures. In these detectors, EHPs are generated and with the help of negative bias, they flow by drift mechanism inside depletion region and enter as minority carriers to P or N semiconductors where diffuse mechanism governs the flow. Since a photodetector needs large detection area to have higher QE, PIN shows better performance compared to PN due to expanded and larger depletion layer in intrinsic region as well as independency of depletion region from applied bias. This advantage is achieved at the expense of lower speed because of the longer drift time needed for carriers in expanded depletion region. If the depletion region is too thin, the capacitive effect becomes significant and again deters response speed. Moreover, the metallic contacts to these semiconductor detectors should have very low contact resistance which is achievable between highly doped semiconductors and metals. However, if the semiconductors have high doping in PN junction, the depletion region will be too small and will decrease QE. Thus, PIN structure is preferable because not only does it keep depletion region thick, but also it provides the chance to have highly doped P and N sides [65]. The materials that are frequently used for this class of detectors are Ge and InGaAs. While Ge (bandgap=0.66 eV) is more fabrication friendly in standard Si fabrication process and integrable CMOS technology, InGaAs devices are faster, with higher quantum efficiency and lower dark current [66]. Moreover, it is possible to modify the bandgap of InGaAs by changing

the composition of this ternary compound semiconductor ($\text{In}_{1-x}\text{Ga}_x\text{As}$):

$$0.356 + 0.7x + 0.4x^2 \quad (2.37)$$

Thus the bandgap of InGaAs can be tuned between 0.34 eV (InAs bandgap) and 1.42 eV (GaAs bandgap).

These type of detectors have high efficiencies and photoresponses on the order of 0.5 mA/W. However, these detectors require cooling and cryogenic temperatures (77 K) of operation due to the fact that they have low bandgap which allows them to absorb NIR spectrum. This stems from the fact that room temperature is too hot for these devices and the excited energetic EHPs do not provide big contrast in the absence of already existing EHPs due to room temperature band to band excitation of carriers. This leads to prohibitive costs of these devices. However, there are reports of incorporating epitaxially grown Ge/SiGe on Si substrates that can operate at room temperatures and decrease the dark current to nA ranges. The reduction in dark current comes from heterojunction between Si and Ge which also reduces recombination in photocollection process in the drift of carriers. The schematic and the energy band diagram (at equilibrium) of Ge/SiGe detectors are illustrated in Figs. 2.11a and 2.11b. The convention of contact signs are chosen to represent forward bias (note that reverse bias is used in photodetection) [67].

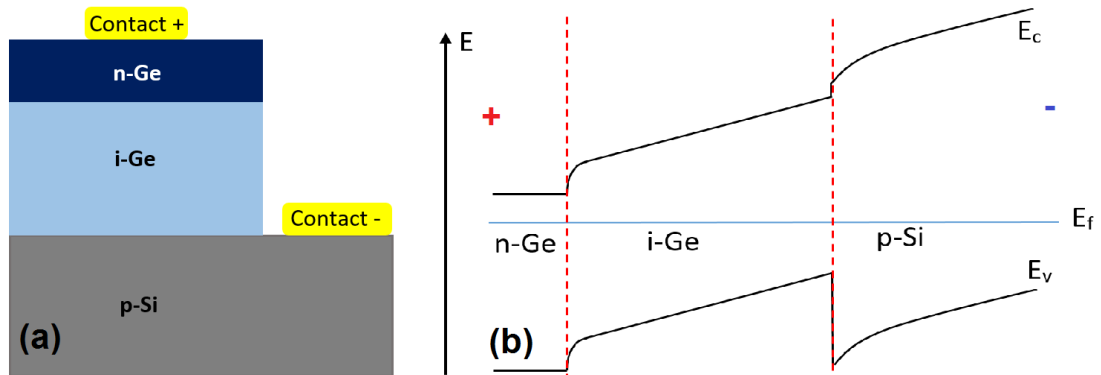


Figure 2.11: (a) Schematic and (b) the energy band diagram (at equilibrium) of a PIN Ge/SiGe photodetector.

2.2.2 Avalanche photodetectors

These group of photodetectors are similar to PIN ones with Ge or InGaAs choices. The difference is the gain mechanism. In avalanche photodetectors, there is a high applied voltage so that the generated carriers in one layer, enter to another high electric field layer both of which are within depletion region. Since they have high speed they provide impact ionization and ionize the static charges giving rise to EHPs. This method has high sensitivity and QE greater than unity. The general level of photoresponsivity value is close to 400 mA/W Figures 2.12a and 2.12b illustrate the schematic and electric field (at equilibrium) of a Ge/SiGe avalanche photodetector [67]. This group of photodetectors also function better in cryogenic temperatures.

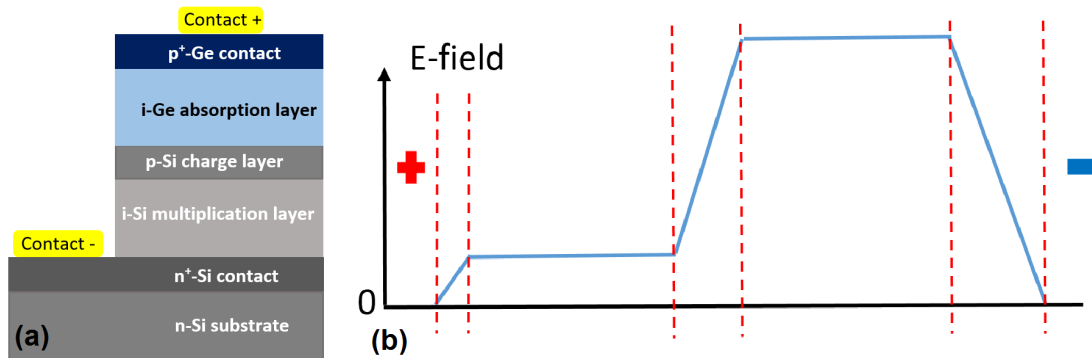


Figure 2.12: (a) Schematic and (b) the electric field (at equilibrium) of an avalanche Ge/SiGe photodetector.

2.2.3 MSM photodetectors

Metal semiconductor metal (MSM) photodetectors can be classified into two categories which are discussed below. They consist of two back to back Schottky diodes with Schottky I-V curves. As opposed to PIN and avalanche photodetectors, in these devices the majority carrier flow governs photocurrent. These class of photodetectors are again similar to PIN detectors with possibility of using either Ge or InGaAs as the absorbing medium. MSM devices generally use

inter-digitated two contacts on top which means that they are easy to fabricate (one photolithography step) and are planar devices. In these devices the EHPs are generated in the depletion region and with the help of a bias, they are collected over Schottky barrier. Since there is Schottky barrier either for electrons or holes, these detectors suffer from high dark current. The general level of photoresponsivity value is close to 600 mA/W and extremely low temperature boosts efficiency due to low bandgap of the semiconductor [67]. The Schematic and energy band diagram (at equilibrium) of a Ge symmetric MSM photodetector is depicted in Figs. 2.13a and 2.13b.

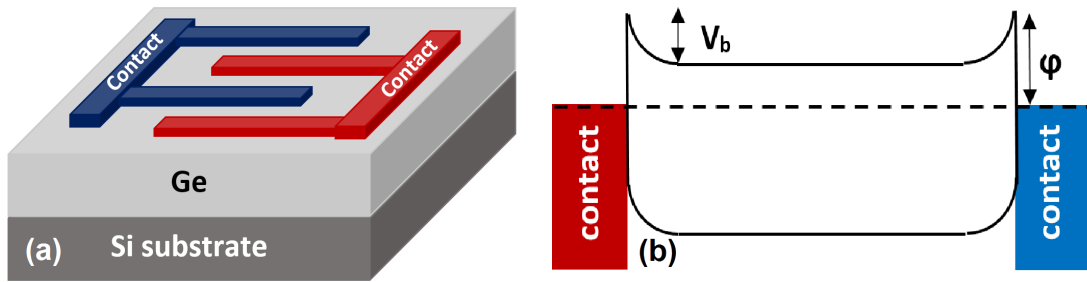


Figure 2.13: (a) Schematic and (b) the energy band diagram (at equilibrium) of a Ge symmetric MSM photodetector.

2.2.4 Quantum well photodetectors

These photodetectors function on the principal of intersubband transitions rather than band to band transitions. In other words, the photons with lower energy excite electrons to higher levels within the same band rather than from valence to conduction band. The fundamental principal is quantum confinement which provides discrete energy states in the conduction band. Besides, the quantum confinement provides the freedom of engineering ground state energy. Together with material choice, the barrier for electron excitation can be properly engineered. The states in the equilibrium condition have electrons and the distance from the state to top of the barrier defines the necessary photon energy. Moreover, in order to prevent tunneling between the wells, the barriers are wide. There are often 20 to 30 wells in these photodetectors. The material of choice is mostly

GaAs/InGaAs. When the bias voltage is applied, the barrier is lowered to let an electron be excited or so called “photoemitted” which is then directed through the structure to contribute to photocurrent. Figures 2.14a and 2.14b show a quantum well structure in equilibrium and under applied bias respectively. These photodetectors provide better response in low temperatures and the optimum photoresponsivities are in the order of 500 mA/W [68]. The contact that has higher potential is called emitter and the other one is collector.

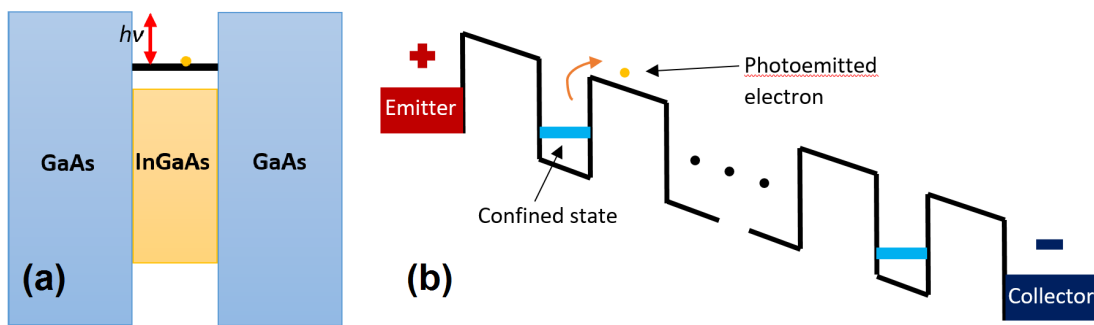


Figure 2.14: Energy band diagram of a quantum well (a) in equilibrium and (b) under applied bias.

2.2.5 Metal semiconductor photodetectors

These type of semiconductors are classified different than MSM detectors due to the mostly plasmonic nature of them. Plasmonic photodetectors in general are inferior in terms of efficiency and photoresponsivity; however, they function well in terms of speed. They are also quite tunable with the geometry nanoantennas and materials and eradicate the need for extremely low temperatures unlike formerly discussed detectors and thus function in room temperature. MS photodetectors are basically comprised of a Schottky junction where instead of a thin film contact, a patterned metallic contact is used which can support LSPs. In order to keep the patterns in contact with each other, a transparent conductive oxide (TCO) is used which encapsulates all nanoantennas and is in contact with semiconductor as well. It should be pointed out that the semiconductor is usually chosen to be lower doped to minimize recombination of electrons (or holes) that

surpass the barrier into the semiconductor during the diffusion process. If the designed photodetector is based on hot electron extraction, the semiconductor would be a low doped n-type semiconductor. When photons with the resonance wavelength energy are incident on nanoparticles, LSPs are excited which then decay non-radiatively and give their energies to produce hot EHPs. Depending on the design (p-Schottky or n-Schottky) the electrons or holes are collected over the Schottky contact with a reverse bias. Plasmonic photodetectors are also considered a significant breakthrough due to the fact that they require very low bias and can be fabricated in extremely small dimensions. The schematic of the device as well as the photocurrent generation mechanism are respectively illustrated in Figs. 2.15a and 2.15b. From the IV curve of Schottky junction, based on the

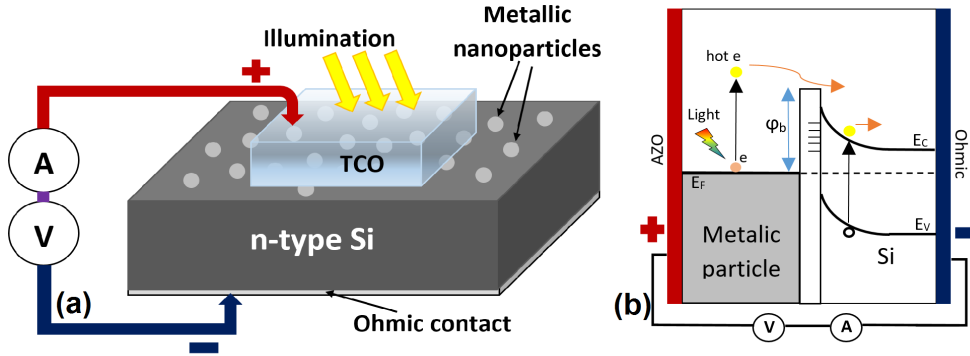


Figure 2.15: (a) Schematic and (b) energy band diagram and photocurrent generation mechanism in Schottky photodetectors.

empirical data the barrier height (φ_b) can be elicited. Thermionic emission is the dominant current flow mechanism in Schottky diodes which is given by [69]

$$I = I_S [(\exp(qV_a)/nkT) - 1] \quad (2.38)$$

In this equation, V_a is the applied voltage, I_S is the diode reverse saturation current, n is the ideality factor, q the charge of electron, k the Boltzmann constant and T the temperature. The reverse saturation current is defined as

$$I_S = A_{eff} A^{**} T^2 \exp(-q\varphi_b/kT) \quad (2.39)$$

Where A_{eff} is the effective area of the limiting contact (i.e. smaller) in the device and A^{**} is the Recharadson constant [70, 71]. In general, though barrier shows

variations with applied bias, it is still negligible [72]. The mentioned equations for Schottky current mechanism are ideal and there are some deviations in fabricated Schottky diodes from this ideal method. These deviations occur due to the fact that the semiconductor side has an ohmic junction with a metal which is not always ideally ohmic. Given the fact that the semiconductor is usually low doped (high doped semiconductors form better ohmic contacts), this effect is more critical. Therefore, a series resistance to the diode (R_S) is usually added to the circuit model of the junction. Another parallel resistance (R_P) is also added to model the high leakage current in high negative bias section of an I-V curve. However, the parallel resistance is negligible in low bias applications such as Schottky photodetectors. The discussed circuit model as well as a $\log(|I|)$ -V curve of a Schottky junction between Pt and n-type Si is illustrated in Fig. 2.16. Since the exponential term in Eq. 2.38 is very large compared to the second term

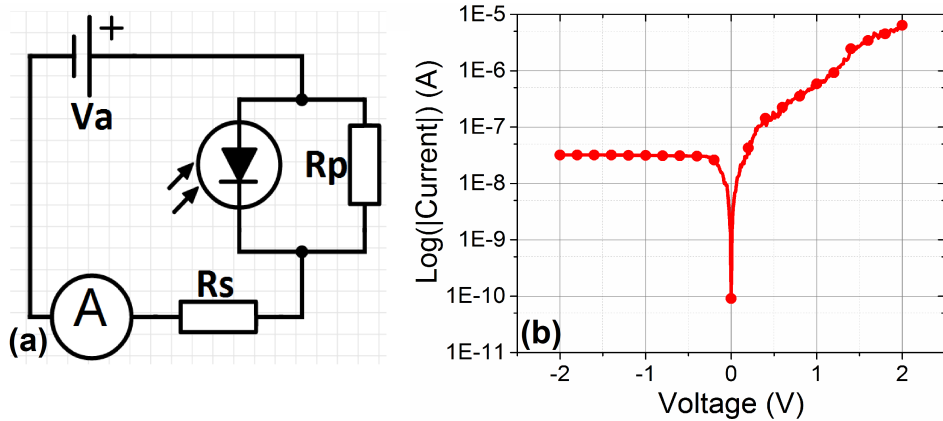


Figure 2.16: (a) Circuit model and (b) logarithmic I-V curve of a fabricated Schottky diode.

at room temperature, the second term can be neglected. Therefore the overall approximated and improved current model is written as

$$I = I_S [q(V_a - IR_S)/nkT] \quad (2.40)$$

Rearranging Eqs. 2.39 and 2.40, the applied voltage is

$$V_a = R_S I + n\phi_b + (nkT/q) \ln(I/AeffA^{**}T^2) \quad (2.41)$$

In Eq. 2.41, $R_S I$ is the dominant term in high forward bias region and thus the series resistance can be found from the slope of the I-V curve at high forward

bias region. Differentiating V_a with respect to $d(\ln(I))$ gives

$$\frac{d(V_a)}{d(\ln(I))} = R_S I + n \frac{kT}{q} \quad (2.42)$$

In Eq. 2.42 it is possible to obtain R_S and n from the slope and y-intercept of $d(V_a)$ versus $d(\ln(I))$ curve respectively. Once they are determined, φ_b can explicitly be found from Eq. 2.41.

One simple and useful method of modeling plasmonic Schottky detectors is using Fowler function which relates quantum efficiency to the barrier height

$$\eta = C_F \frac{(h\nu - q\varphi_b)^2}{h\nu} \quad (2.43)$$

where h and ν are Plancks constant and the frequency of light respectively and C_F is a fit parameter called Fowler emission coefficient. This method is interesting due to the fact that it relates the calculated or simulated absorption to the measured spectral photoresponsivity and gives barrier height. Spectral photoresponsivity (R) and absorption (A) are correlated by $R(v) = \eta_i A(v)$. This method has been reported to estimate the barrier height reasonably well [73]; however, this method is quite controversial and has certain deficiencies due to the following presumptions: generated hot electrons act as free electrons and the initial momentum distribution of hot carriers is isotropic [63].

2.2.6 Metal insulator photodetectors

These photodetectors use SPPs or LSPs to excite hot EHPs. The photocurrent mechanism is tunneling through very thin insulator films. In an MIM structure, where the middle insulator is very thin, electrons can tunnel through the thin metals rather significantly if an electric field is applied. For insulators thicker than 10 nm, there is almost zero tunneling. A symmetric tunneling barrier in equilibrium (no bias) is illustrated in Fig. 2.17. In this figure, the wave functions (ψ_i) in three regions ($i=1, 2, 3$) are depicted. In order to find the tunneling probability (T), the following equation can be used

$$T = \frac{\psi_2^*(L_b)\psi_2(L_b)}{\psi_2^*(0)\psi_2(0)} \quad (2.44)$$

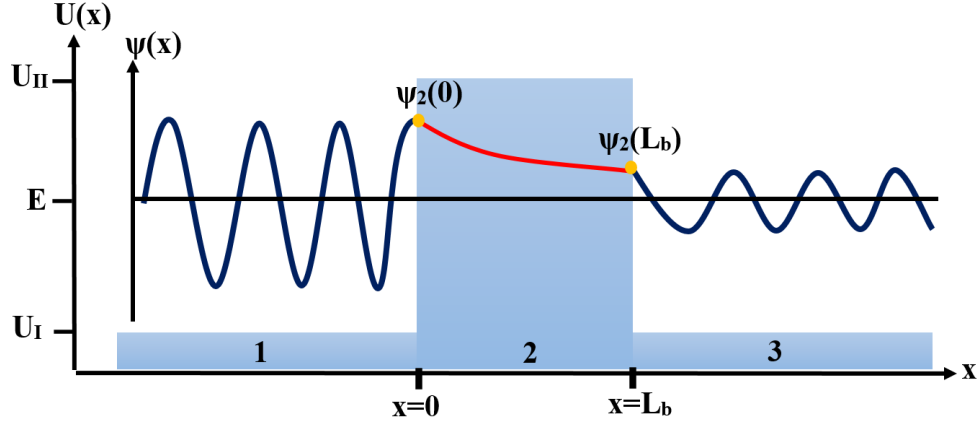


Figure 2.17: A symmetric tunneling barrier MIM structure in equilibrium.

where L_b is the tunneling barrier thickness. Using the zero order WKB approximation for a potential energy E , Eq. 2.44 can be simplified to

$$T = e^{-\int_{x=0}^{L_b} 2\bar{h}^{-1} \sqrt{2m^*[U(x)-E]} dx} \quad (2.45)$$

where $U(x)$ is the potential energy of the barrier and \bar{h} is the reduced Planck constant. The current through a tunneling barrier is given by

$$J(V) = 4\pi e \frac{m}{h^3} \int_{x=0}^{\infty} dET(E) \int_{E=E_x}^{\infty} dE(f(E) - f(E + eV)) \quad (2.46)$$

where $T(E)$ is the electron tunnel probability, e the electron charge, V the applied bias, E_x the kinetic energy of the electron in the direction perpendicular to the barrier and f is the Fermi distribution functions of the energy levels (or occupation densities) [74]. Equation 2.45 also reveals that increasing the tunnel barrier thickness by a factor of two results in a $1/e^{-2}$ decrease in tunneling probability and tunneling current as a result. Therefore, thick barriers block dark current and photocurrent largely. Thus, the barriers are designed thin in such devices and instead, the two metal energy levels are adjusted with a mismatch of work functions to have high photocurrent as well as low bias.

SPP excitation is the dominant method for photocurrent generation in devices that tailor tunneling transport mechanism. They can be either MIM or MIMIM structures both of which are illustrated in Fig. 2.18. If an MIM structure is fabricated to excite SPPs, one of the metal layers should contain nanoantennas. In this case, however, there will be competing photocurrents from LSP and SPP

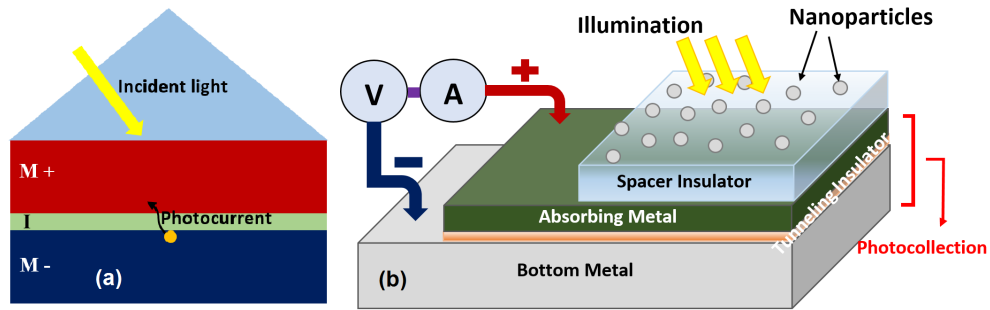


Figure 2.18: (a) MIM and (b) MIMIM photodetector structure [1].

excitation in the nanoparticle and metal layer respectively which will reduce photocurrent. One solution to this is using Kretschmann configuration. The main obstacle for this method is the bulky structure which is not fabrication friendly at all. Moreover, the resulting photoresponsivity will not be broadband. The photoresponsivity level of these devices are on the order of 1000 mA/W at a bias level of 50 mV [75]. A reasonable solution to the obstacles mentioned is using two MIM structures. In this design, the absorption and photocollection junctions will be separated which would give way to efficient engineering of each MIM. In these devices, the middle metal is shared between the absorption and photocurrent MIM structures. The photoresponsivity level on these type of devices is on the order of 0.1 mA/W at a 50 mV bias. The thickness of insulator in tunneling junction is generally less than 5 nm [76, 1].

In conclusion, metal insulator stacked photodetectors put forth many opportunities for material choice and interface and junction engineering which can form next generation NIR photodetectors.

Chapter 3

Simulation, Fabrication and Characterization

In this chapter, first simulation methods using Lumerical FDTD Solutions will be discussed. Afterwards, the fabrication tools used in UNAM (National Nanotechnology Research Center) [77] and NANOTAM (Nanotechnology Research Center) [78] will be discussed briefly. Finally, the characterization systems will be reviewed.

3.1 Simulation

For all the simulations, a commercial-grade simulator based on the finite-difference time-domain method was used to perform the calculations [59]. Finite difference time domain is a method developed based on Maxwell's time dependent curl equations

$$\nabla \times \bar{E} = -\frac{\partial \bar{B}}{\partial t} \quad (3.1)$$

$$\nabla \times \bar{H} = \frac{\partial \bar{D}}{\partial t} + \sigma \bar{E} \quad (3.2)$$

It is implied from the name that a short electromagnetic pulse is sent in the desired frequency range and the solution is performed in time domain. Eqs. 3.1 and 3.2 are discretized by central difference approximation [79]. As an example a 2D simulation region from the software environment is depicted in Fig. 3.1. In this

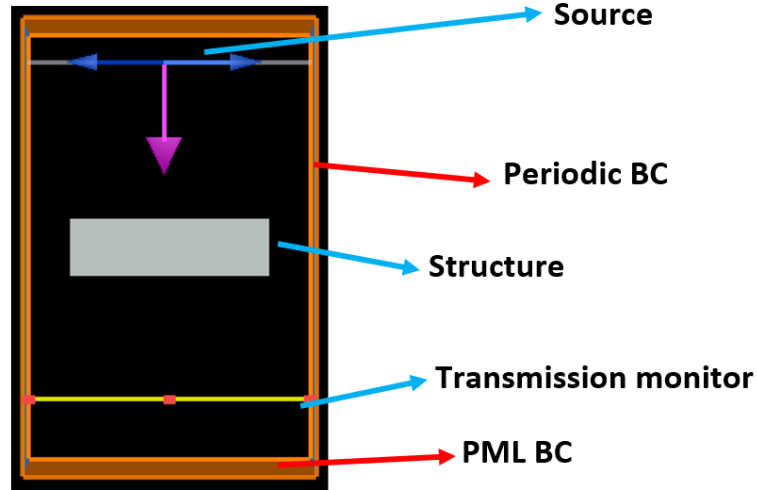


Figure 3.1: Lumerical FDTD Solutions environment.

figure, there is a plane wave source with x-polarization illuminating the object from top and a monitor is placed in the bottom to record Fourier transformed transmitted power (steady state condition). The top and bottom boundaries in the y-direction simulation region are set as PML. In the x-direction, the left and right boundaries are set periodic.

3.2 Fabrication

This section includes a glance at the fabrication tools used for the devices in this thesis and a brief discussion on their operation mechanisms. In the cleaning process of samples, since quartz or silicon were used as mechanical substrates, no RCA cleaning and oxide removal was carried out. The cleaning process included only acetone agitation followed by isopropanol and deionized water cleaning and nitrogen flow.

3.2.1 PVD

PVD stands for physical vapor deposition. In this method, a material is heated or bombarded and the gas phase material or detached atoms are transmitted and physically deposited on the target. Therefore, there is no strong chemical bonds between the deposited material and the target (substrate). These devices require very low pressures to provide line of sight deposition. PVD method is mostly used for metal deposition.

3.2.1.1 Thermal Evaporator

Thermal evaporator is the most simple PVD method. In this system, the material (source) is extremely heated by guiding a very high current through it. Since there is resistive heating in the source material, it finally starts to vaporize. The source is usually placed in the bottom of the chamber and the target is placed in the top as depicted in Fig. 3.2a. When the pressure is very low (ultra high vacuum), the

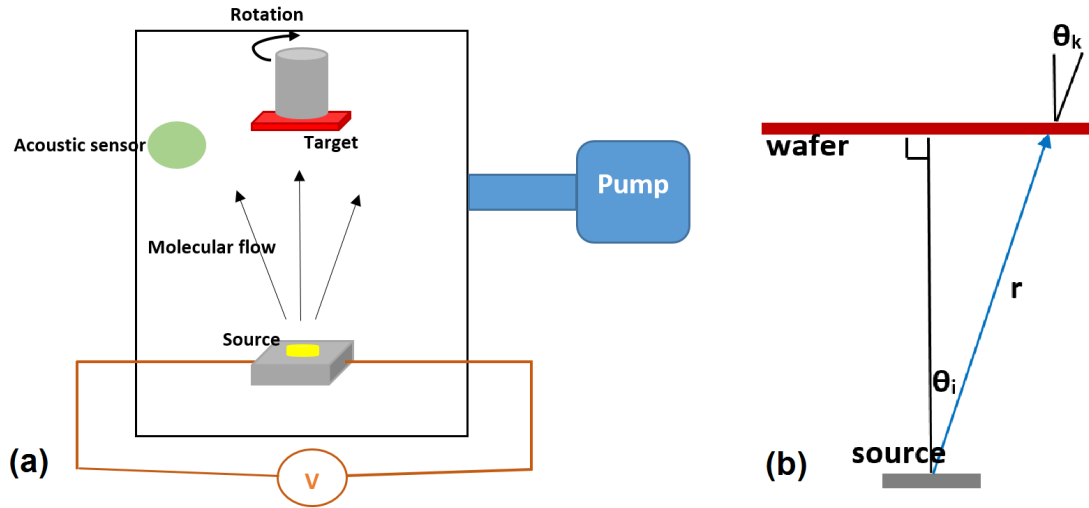


Figure 3.2: (a) Schematic of the chamber of a thermal evaporator (PVD system) and (b) the deposition geometry.

flow regime is called molecule like, meaning that there is minimum interaction between molecules and they interact with walls only. Therefore, mean free path

is in the order of few meters. In the schematic, there is a rotation in the target to make the deposition uniform and remove the spatial variations of the deposited film as much as possible. The pump is responsible for the vacuum of the chamber. The acoustic sensor monitors the deposition thickness. If the source is assumed to be a small planar surface (Fig. 3.2b), deposition rate (v) can be expressed as

$$v = \frac{R_{evp}}{\pi N r^2} \cos^n(\theta_i) \cos(\theta_k) \quad (3.3)$$

where R_{evp} is the evaporation rate and N is the density of the material being deposited [80]. The order of anisotropy n defines the distribution and the higher the anisotropy, the more uniform the deposition. In other words, if the source is elongated to be parallel and equal to the wafer (which is not the case in thermal evaporators), the deposited film will be more uniformly thick. The distribution is thus \cos^n type. The PVD deposition system used in fabrication processes is a VAKSIS system. The deposition pressure is $2-5 \times 10^{-6}$ Torr. The system is illustrated in Fig. 3.3a.



Figure 3.3: VAKSIS (a) thermal evaporator and (b) sputtering systems.

3.2.1.2 Sputtering

In this method, instead of evaporating the source, a plasma is used to sputter target which dislodges atoms and after molecular flow (similar to thermal evaporation), the atoms are deposited on the wafer. Some metals such as W which have very high evaporation temperatures are impossible to be deposited by thermal evaporation. In fact, the source holders in thermal evaporator are made of W. Thus, sputtering is used for such metals. It is also useful for the deposition of alloys. The schematic of a DC sputtering system (pump and sensor not shown) as well as voltage through the chamber are depicted in Figs. 3.4a and 3.4b. VAKSIS

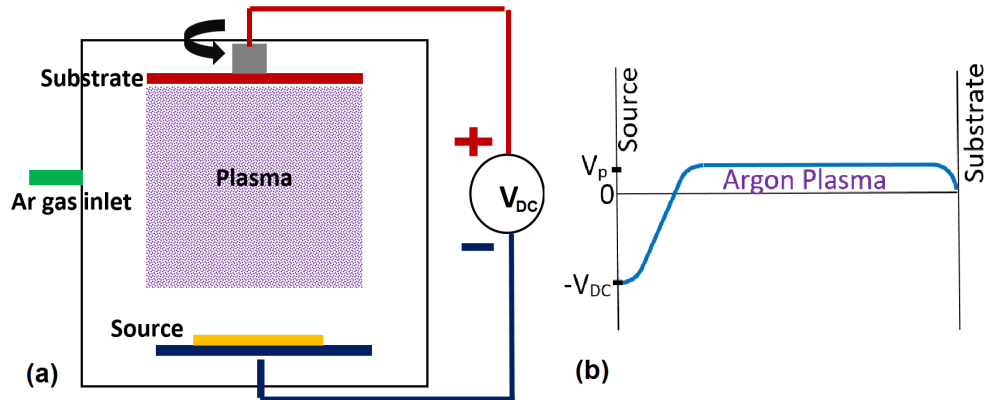


Figure 3.4: (a) Schematic of the chamber of a DC sputtering system and (b) the voltage drop inside the chamber.

sputtering system is used in the fabrication process (Fig. 3.3b). Sputtering also generates parallel deposition rays which provides more uniform deposited films. RF sputtering is mostly used for the deposition of dielectrics.

3.2.2 CVD

CVD is the abbreviation for chemical vapor deposition. In this method, the atoms of the source form chemical bonds and react with the surface of the wafer (or target) rather than physically sticking to it. In CVD systems, the reactants are in gas phase and the reaction energy is provided by heating or plasma. From

the myriad of CVD methods, atomic layer deposition (ALD) or atomic layer epitaxy is used in the fabrication processes of the devices in this thesis. Contrary to CVD methods, in ALD the two reactants are not simultaneously present in the chamber. This gives a very big advantage to ALD over other CVD methods; each deposition cycle (each of the two needed) are self terminating which means that there is Å-thick layer by layer deposition. As a result, deposition rate is controllable to Åprecision and the uniformity of the resulting films are outstanding. The Schematic of the ALD and the Cambridge Nanotech Savannah S-100 deposition system are depicted in Fig. 3.5. ALD is widely used in dielectric coating and recently, there are volatile precursors for metal coatings as well. In CVD systems, since reaction is the main drive for deposition, there is no need for ultra high vacuum. Moderate vacuum levels are acceptable for keeping the chamber isolated.

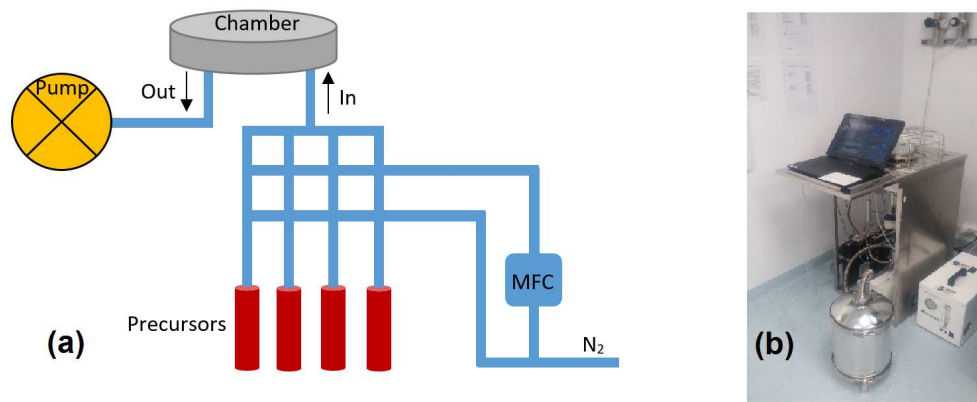


Figure 3.5: (a) Schematic of an ALD system and (b) Cambridge Nanotech Savannah S-100 ALD system.

The ALD system in Fig. 3.5a includes the following [81]:

- **Transport Gas Supply:** This gas is N₂ which is an inert gas. It is used for transporting the precursor vapors and purging the reaction chamber. A continuous flow of the inert gas is regulated with mass flow controllers to allow or block precursors entering the chamber. The flow rate is optimized for the device where the operating pressure is near 1 Torr.
- **Sources and precursors:** The sources are connected via cylinders which

include gas phase reactants.

- **Flow and sequencing control of the sources (inert gas valving):** Each source cylinder is connected both to a reaction chamber and exhaust such that the exhaust connection is between the source and the chamber. Each tube is also equipped with two inert gas flows which are the transport gas and the valving gas. Both these gases are connected to N₂ flow. When the source is in off state, the valving gas flow is on and the transport gas flow is off. The valving gas flow is divided into two parts, one purging the reaction chamber and the other one setting up a laminar flow barrier. The flow rate of the valving gas in the flow barrier is adjusted such that it counterbalances the diffusion rate of the precursor toward the chamber and blocks it. Similarly, when the source is turned on, the valving gas is turned off and the transport gas is turned on, thereby breaking the flow barrier.
- **Reaction Chamber:** The chamber is where the reactions take place and it has two connections one for entrance of precursors and one for the purging and exhaust system. There are also heaters connected to the chamber to keep it at the desired temperature which facilitates reaction of precursors with wafer. The temperature is optimized and affects deposition rate. In very low temperatures, there might not be enough activation energy for reaction. For very high temperatures, on the other hand, there might be precursor decomposition and unwanted reactions may take place. The window between these two extreme temperature values is called the ALD window. The ALD window is usually between 100 and 300 °C.
- **vacuum pump and related exhaust equipment.**

In order to further elucidate deposition process, Al₂O₃ is taken as an example which is deposited by Trimethyl aluminum (TMA) and water precursors. The deposition process is shown in Fig. 3.6. A deposition of monolayer is called a cycle which is composed of two sub-cycles including reaction and purge steps. Deposition of Al₂O₃ starts with introducing first precursor. In this step, the substrate surface is terminated with hydroxyl groups by introducing H₂O. This is also crucial for the reaction of the second precursor which will build on this

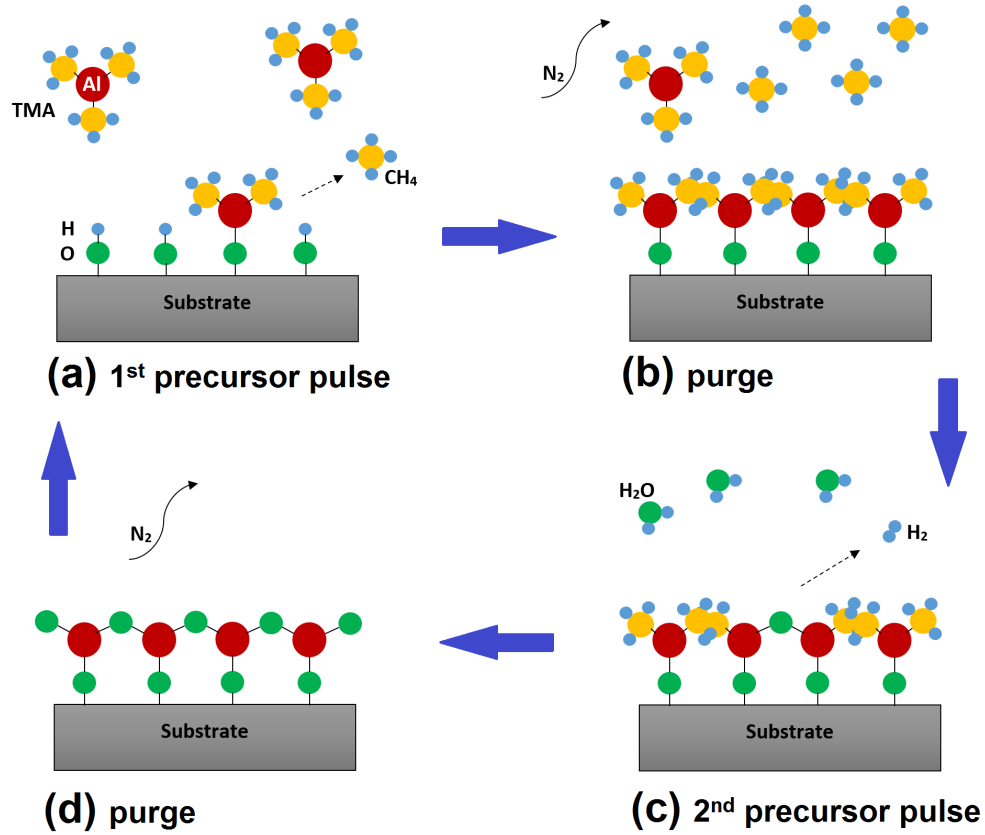
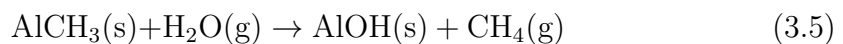
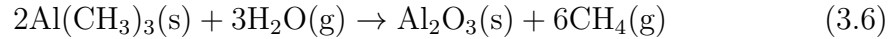


Figure 3.6: Al₂O₃ deposition from TMA and water cycles. (a) Introduction of hydroxyl groups to the surface and pulse of TMA in to the chamber, (b) reaction between TMA and the hydroxyl groups and purge of the byproducts, (c) introduction of hydroxyl groups to the surface and (d) reaction between TMA and the hydroxyl groups and purge of the byproducts

step. The byproducts as well as unreacted groups will be purged after reaction (second step). The reaction and purge are in one sub-cycle and since N₂ flows continuously, first it carries the precursor to the chamber for reaction and carries it out afterwards. Then, at second sub-cycle, the second precursor TMA (Al(CH₃)₃) will flow into the chamber. Similar to the first sub-cycle they will be adsorbed to the surface and will form chemical bonds with the substrate atoms and will release CH₄. Then, purge will take place and one cycle will be completed as shown in Fig. 3.6. The reaction equations can be written as [82]



These equations can be concisely expressed as



3.2.3 RTA

Rapid thermal annealing (RTA) is used for many electronic junctions to enhance Schottky or ohmic behaviors which may be attained by dopant activation or ion implantation damage repair. The level of temperature required for rapid thermal processing in semiconductors is in the order of 1000°C. The annealing is performed under N₂ flow to avoid oxidation. Moreover, forming gas is also a popular and well-known RTA process gas flow for junction treatment. The main advantage and use of RTA over furnaces is their capability to quickly rise to high temperatures which is attained by high intensity lamps or lasers. The heating rates can reach 200°C/s. The cooling is slow in standard systems due to the fact that high slowing temperature may cause fracture in the semiconductor with high stress on the crystal.

Another important application of RTA in research is dewetting near (and below) their melting temperatures (*i.e.* on the order of 500°C for Au and Ag). Some films such as gold or silver are not completely stable if they are deposited in very thin thicknesses. For example, if Au is deposited in the order of 5 nm, it will not form continuous film and there will be pinholes and the Au/air interface is unstable. If it is deposited in the order of 10 nm, the Au/air interface is thermodynamically metastable, meaning that under excitation with heat, the film will agglomerate in islands to minimize the vicinity with air with a specific contact angle [83]. This method is used to create random nanoparticles on a surface which can exhibit broadband plasmonic behaviors. The parameters affecting the particle sizes are the heating rate, cooling rate, film material and thickness and the metal wafer interface. The system used in creation of nanoislands is ATV Technologie GmbH, SRO-704 RTA (Fig. 3.7).



Figure 3.7: ATV Technologie GmbH, SRO-704 RTA system.

3.2.4 Photolithography

Photolithography is the primary process of transforming the desired feature onto the substrate. In this process a mask is used which includes the features written by laser on a glass and the places outside of the feature are coated with Cr. In photolithography, a UV lamp is used to expose the sample. Photolithography systems are placed in yellow rooms where the filtered fluorescent lighting in photolithography cleanrooms contains no ultraviolet or blue light in order to avoid exposing photoresists undesirably. This stems from the fact that photoresists have absorption in the first segment of visible light spectrum. The minimum feature size attainable by photolithography is governed by the wavelength used and the maximum tolerable distortion in features. Photolithography has three main modes that are optical projection, proximity and hard contact photolithography. In hard contact the mask is in contact with wafer which contaminates the mask and wafer and the masks are cleaned after each process. Hard contact is used for obtaining very small features since there is diffraction in proximity method which might distort the spatial features in small patterns. In projection method, lenses are used to further focus and reduce the dimensions of the features compared to

the mask itself. There are two sensitive wavelengths which are i-line (365 nm) and g-line (436 nm).

In photolithography as the first step, a solution (HMDS) is spin coated on the wafer to increase sticking of the photoresist. Afterwards, a photoresist is spin coated (we used AZ5214E, positive, i-line sensitive) on the wafer which includes photoactive compounds (PAC). Photoresists are composed of inactive resin, photoactive compound and solvent which is used to adjust the viscosity of the solution. After completing the spin coating, a pre-bake is done at 110°C for 1 to 3 min to increase sticking of the solution. Then, the wafer is aligned under the mask so that the features are obtained in the desired section of the wafer. When alignment is finished, the UV light exposes the photoresist. In positive photoresists, the exposed areas make PACs soluble in certain solutions called developer (AZ400K for 5214E) and other areas under the Cr coated parts of the mask are insoluble. Therefore, the photoresist in soluble parts is removed. In negative photoresists, the reverse phenomenon takes place and the exposed areas are insoluble. Afterwards, the sample is dipped in developer so that the exposed soluble areas are washed away. Figure 3.8 illustrates the schematic of the exposing system in proximity mode and the mask aligner system used in the processes in this thesis.

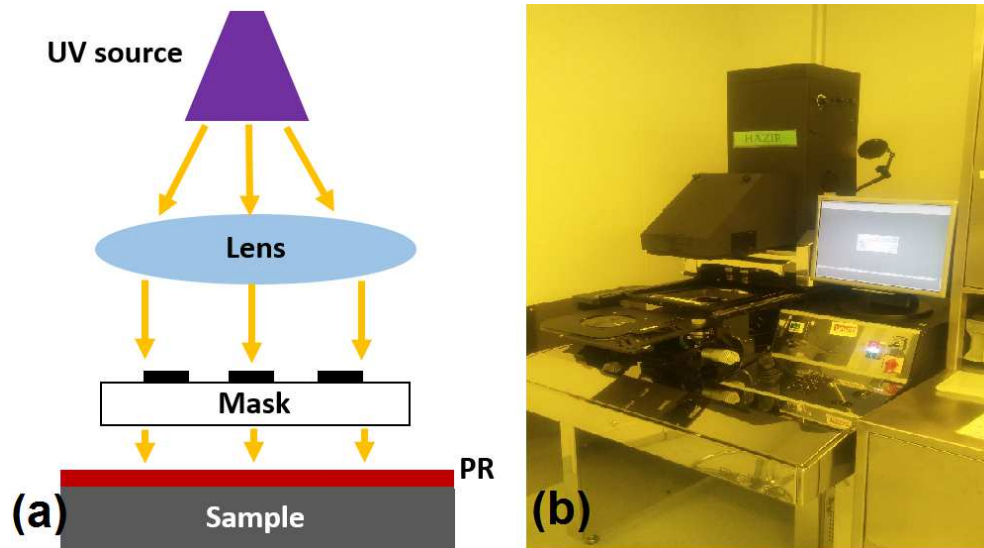


Figure 3.8: (a) Schematic of the exposure in proximity mode and (b) the aligner system used.

3.2.5 Etching

Etching is the process which allows for getting rid of some parts of a deposited film to obtain desirable features. This process is mostly carried out after lithography. After developing in the photolithography process, the material areas which are under soluble part are exposed and the other sides are covered with photoresist. Then, in the etching, the exposed material sections are removed and the photoresist protects other parts. There are two main types of etching which are wet and dry etching. In wet etching, a chemical that attacks the film by reaction is used which is called “liquid etchant”. In dry etching, plasma is used to attack the wafer (similar to sputtering). In this method, the chamber is in vacuum and molecules like CF_4 and O_2 are ionized and accelerated in RF field and hit the surface of the wafer which results in dislodging of atoms in wafer (etching). Dry etching can be a combination of chemical and physical etching by choosing reactive ions for etching. The main features of etching are:

- **Etch rate:** This is the speed of etch which is optimized by doses and time to obtain desirable amount of etching.
- **Selectivity:** This is very important specifically in wet etching. For example, if in a multilayer sample, the first layer is supposed to be etched, after finishing the etching in the first layer, the etchant might start etching of the second layer. If the etch rate in second layer is high or comparable to the first layer it might cause problems and the second layer might be lost as well. This would also be problematic if we have a combination of two layers in one film and only one of them should be etched.
- **Isotropy or anisotropy:** In wet etching the etchant generally attacks the material in all directions which is therefore called isotropic etch. This method can cause unwanted undercuts in the sample. However, dry etching is directional and anisotropic which can give almost vertical etching. Figure 3.9a illustrates a grating sample after wet and dry etching.

Wet etching has high throughput and many wafers can be etched at a time.

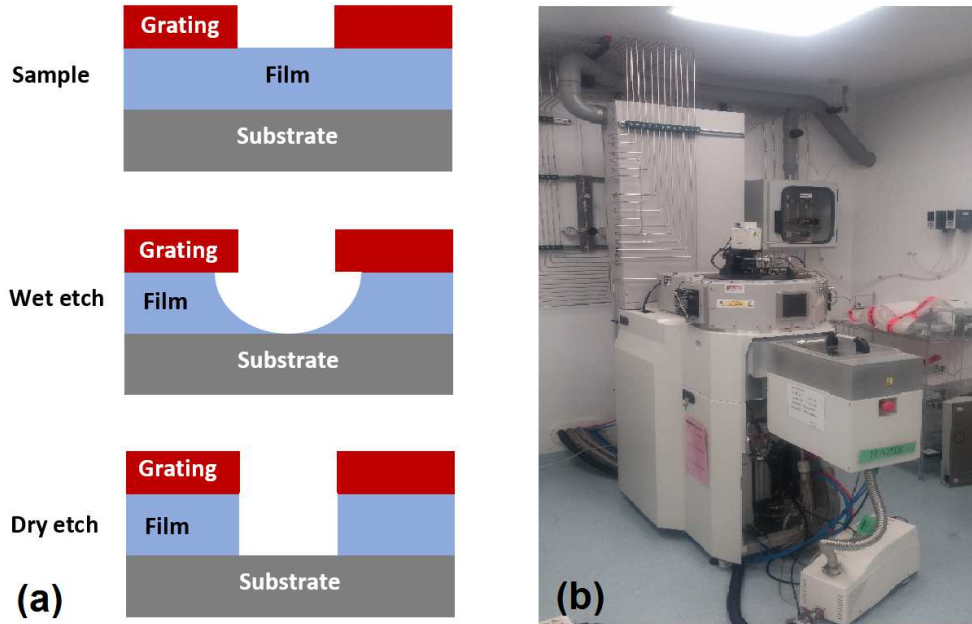


Figure 3.9: (a) Schematic of wet and dry etched grating sample and (b) the inductively coupled plasma etch system used for devices in this thesis.

However, due to isotropy and lack of selectivity dry etching is more reliable in small features. The undercuts which are illustrated in Fig. 3.9a can reach each other (two adjacent undercuts) in high aspect ratio etching and the whole film might be etched. The inductively coupled plasma etch system used in this thesis is illustrated in Fig. 3.9b which uses O_2 for etching.

3.3 Characterization

For characterization of the devices, some setups and tools are used which are Ellipsometer, FTIR and Spectral photoresponsivity setups.

3.3.1 Ellipsometer

Ellipsometer has been used for two different characterization processes. One of them is angled reflection and transmission measurement and the other one is

spectroscopic characterization of films.

3.3.1.1 Reflection and Transmission

In this measurement, the goal is measurement of reflectance and transmittance versus wavelength of samples. The measured reflected or transmitted intensity from the sample is normalized to the case when there is no sample on the way of the beam. This normalization removes the intensity distribution of lamp in the system. The sample is thus illuminated in different angles of incidence with TE (or s) or TM (or p) polarized light. The normalized ratios of intensities give Fresnel reflection and transmission coefficients. The schematic of an ellipsometer as well as the system used (J.A. Woollam Co. Inc. VASE Ellipsometer) are illustrated in Figs. 3.10a and 3.10b respectively.

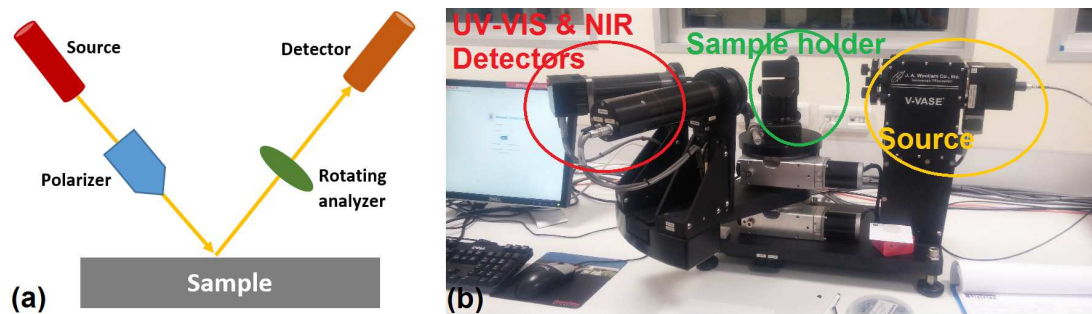


Figure 3.10: (a) Schematic of an ellipsometer and (b) J.A. Woollam Co. Inc. VASE Ellipsometer.

3.3.1.2 Spectroscopic Characterization

The ellipsometer diagram illustrated in Fig. 3.10a includes many components. There is a monochromator in the output of the source which sets the wavelength. First, the polarizer sets the polarization state of light (linear) as we desire in a known polarization. Afterwards, the reflected light off the sample is entered to analyzer which is the same as the polarizer but in the photodetection section. The only difference is that the analyzer in VASE rotates with a fixed angular

speed and converts the light intensity to a changing intensity and thus, a varying voltage on detector. This method allows for easy detection of the polarization status of the reflected light. If the light is linearly polarized The analyzer turns linear polarized light to sinusoidal voltage, circular to fixed DC and elliptical to a sinusoidal with a DC offset.

A dielectric material can be optically defined by its complex refractive index, $\tilde{n} = n + jk$. Refractive index is the square root of dielectric permittivity $\tilde{\epsilon}$. The light goes through polarization change when it propagates through a dielectric medium. In spectroscopic ellipsometry method, the polarization change upon reflection and transmission is used to extract the refractive index of the given material. Other information such as film thickness, surface roughness, material composition, carrier concentration, band structure and mechanical properties can also be extracted through theoretical modeling of the extracted data from the spectroscopic ellipsometry method. A reflected light would undergo polarization change which can be described by a complex reflectance ratio

$$\rho = \frac{r_p}{r_s} = \tan(\psi)e^{j\Delta} \quad (3.7)$$

In Eq. 3.7, ψ and Δ are amplitude ratio and phase shift respectively, which are extracted experimentally. The ψ and Δ pair is converted to Fresnel reflection coefficients. Afterwards, a fitting is needed to construct refractive index and thickness of the film. There are many oscillator function fitting models such as Lorentz, Drude, Cody-Lorentz and Gaussian oscillators to determine the refractive index. Since the films modeled in this study are transparent in the wavelengths of interest (VIS and NIR), Cauchy's model is used which assumes that the imaginary part of refractive index (k) is zero and the real part is [84]

$$n = a_0 + \frac{a_1}{\lambda^2} + \frac{a_2}{\lambda^4} + \dots \quad (3.8)$$

3.3.2 FTIR

Fourier transform infrared spectroscopy (FTIR) can measure reflectance, transmission and emission of a sample. Contrary to filtered light source method, FTIR

can measure all the wavelengths of a given spectrum at once. FTIR has a broad-band light source. The beam goes through a Michelson interferometer which has one moving mirror. The moving mirror modulates the beam such that at each position of the moving mirror, certain wavelengths are blocked or transmitted due to interference. The data is collected and after analysis, reflectance and transmittance data are generated. The normal reflectance is measured by Bruker Vertex 70v FTIR in this study which is illustrated in Fig. 3.11.

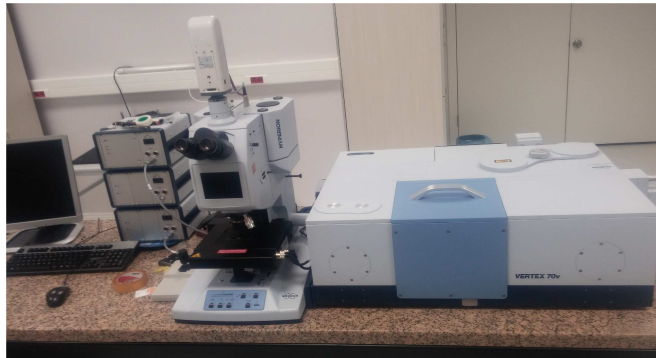


Figure 3.11: Bruker Vertex 70v FTIR in NANOTAM.

3.3.3 Spectral Photoresponsivity and Normal Absorption

3.3.3.1 Normal Absorption

For some part of the reflectance measurement, a home made reflection measurement setup was used. It is comprised of a halogen illuminator connected to a microscope and directed perpendicular to sample and the reflected light from the microscope is fed to a Newport OSM2 spectrometer and the data is collected by interfacing the spectrometer with PC. The reflectance measurements are normalized to an thick Al coated mirror. The schematic and the photo of this setup is put forth in Fig. 3.12.

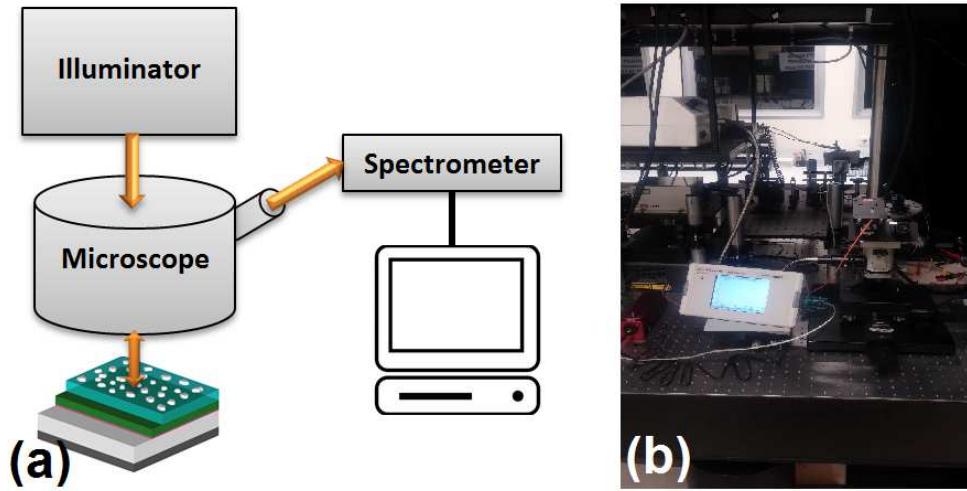
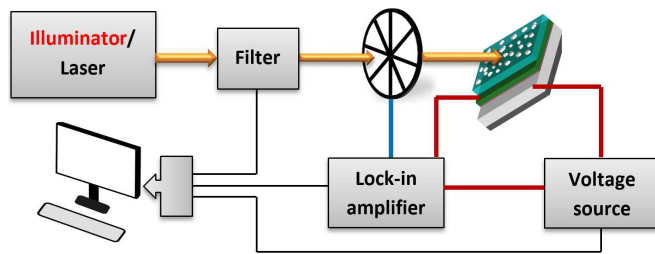


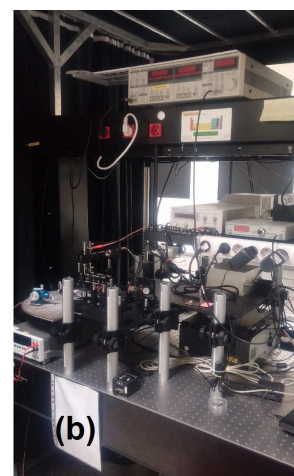
Figure 3.12: (a) Schematic of the home made reflectance measurement setup and (b) the photo of the setup [2].

3.3.3.2 Spectral Photoresponsivity

The dark I-V measurements of the devices are conducted using KEITHLEY 2401 Sourcemeter. The spectral photoresponsivity is measured also using a home made setup. For the spectral photoresponsivity for the wavelengths between 400 to 800 nm (VIS), we used a Xenon-lamp illuminator. The output of the lamp goes through an Oriel 74004 monochromator (1/8 meter, 1200 lines/mm grating) and monochromatic light is collimated and chopped with a mechanical chopper and the chop speed is 380 Hz. This speed is fed back to a lock-in amplifier (SR830). The short circuit photocurrent is measured by the lock-in amplifier. In order to measure the power at each wavelength, a calibrated Si detector is used at the sample position to collect the reaching light source power. The setup for photoresponsivity measurements for the NIR region (800 nm to 1300 nm) is similar to the afore-mentioned one; except that the source is a super continuum laser (Fianium) which is monochromated by an acousto-optic transmission filter (AOTF - Crystal Tech.) and the chopper speed is 960 Hz. The spectral power for the NIR region is detected with a calibrated InGaAs detector. The schematic and the photo of NIR photoresponsivity measurement setup is shown in Fig. 3.13.



(a)



(b)

Figure 3.13: (a) Schematic of the home made photoresponsivity measurement setup and (b) the photo of the NIR setup [2].

Chapter 4

Plasmonic MIM Absorbers and MIMIM Photodetectors

This chapter is based in part on the publication “Large area compatible broadband superabsorber surfaces in the VIS-NIR spectrum utilizing metal-insulator-metal stack and plasmonic nanoparticles,” **S. Abedini Dereshgi** and A. K. Okyay, *Optics express* Vol. 24, Issue 16, pp. 17644-17653 (2016). Reproduced (or Reproduced in part) with permission from Optical Society of America Publishing Group. Copyright 2016 Optical Society of America.

This chapter is also based in part on the publication “Plasmonically enhanced metalinsulator multistacked photodetectors with separate absorption and collection junctions for near-infrared applications,” **S. Abedini Dereshgi**, Z. Sisman, K. Topalli and A. K. Okyay, *Scientific Reports* Vol. 7, pp. 42349 (2017). Reproduced (or Reproduced in part) with permission from Nature Publishing Group. Copyright 2017 Nature Scientific Reports.

Some parts of the materials in this chapter are based in part on the publication “MIMIM photodetectors using plasmonically enhanced MIM absorbers,” **S. Abedini Dereshgi**, and A. K. Okyay, *Proceedings of SPIE* Vol. 10099, pp. 100991C-1 (2017). Reproduced (or Reproduced in part) with permission from

4.1 Introduction

As discussed earlier in chapter 1, plasmonic absorbers have been a hot topic for the recent decade. The attractiveness is in part due to the geometry dependence nature of plasmonic MIM absorbers which provides the tunability of bands and peaks of absorption, and in part due to very thin devices that are possible in this mechanism. Different MIM structures with the top metal layer designed as gratings [10, 11], nanoparticles [12, 13, 14, 15] and nanopillars [16, 17, 18] have been reported for more efficient, omni directional and compact structures thanks to advanced patterning methods such as EBL. MIM structures are capable of confining light in the nanoantenna-air and the spacer insulator layer which correspond to LSP and SPP excitation respectively [10]. Fabricating broadband absorbers is a challenge that has dragged a lot of attention. Some methods such as an MIM absorber with multi-harmonic geometries that bring together several absorption peaks from different geometries in a super cell was one way to achieve broadband absorption [19]. However, the plasmonic layer in these devices are fabricated using EBL which is slow, low throughput, expensive and applicable to only small areas. Therefore dewetting of thin films which creates randomly distributed and sized nanoparticles is an easy and cost-effective alternative for the top plasmonic layer.

Due to the myriad of applications for NIR photodetection ranging from telecommunication to spectroscopy, these devices are yet to be optimized. Since traditional semiconductor PN photodetectors for NIR are not functional in room temperature, plasmonic counterparts have been proposed. In plasmonic photodetectors, incident photons on the plasmonically active layer excite LSPs or SPPs and their non-radiative decay results in energetic EHPs that can be harnessed as photocurrent at a proper junction like Schottky [37]. Despite functioning fine, the reported designs are not tunable due to the fact that absorption and photodetection segments of the devices are the same.

In this chapter, first a plasmonic MIM absorber will be designed with the main focus on photodetection applications. In other words, different materials will be studied to have and MIM with ultra high absorption in the bottom metal through the excitation of SPPs in the bottom metal and insulator interface [3]. Then, the absorber MIM will be integrated on top of another MI to form a photodetector. The absorber (top) MIM and the photocollection (bottom) MIM share only one metal and provide the freedom of engineering each separately. The bottom MIM photocurrent junction is designed such that it blocks dark current and allows for collection of energetic EHPs by tunneling. The non-radiative decay of SPPs results in hot EHPs in the middle metal of MIMIM structure and by a proper bias, photocurrent can be sensed [2].

The schematic of the MIMIM photodetector is provided in Fig. 4.1, which points out the absorption and photocurrent MIMs with the applied bias polarity and current measurement circuitry used in the final photodetector. The shown thicknesses and materials of the films are for the most optimum device fabricated. We will discuss the optimum device at the final parts of this chapter. The proposed MIMIM structure is composed of (from top to bottom) metal nanoparticles (M_{NP}), spacer insulator (I_{spa}), absorbing middle metal (M_{abs}), tunneling insulator (I_{tunnel}) and the bottom contact metal (M_{cont}).

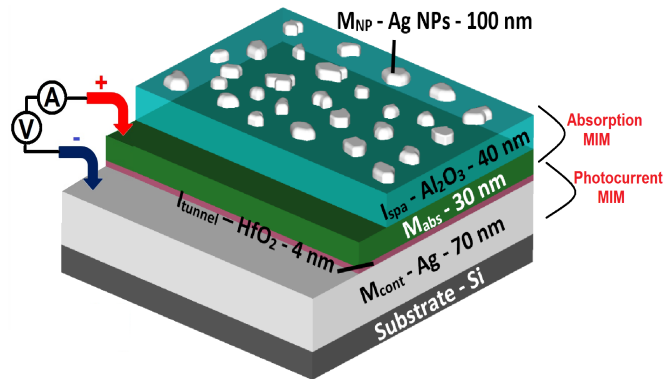


Figure 4.1: Schematic of the total MIMIM photodetector structure [2].

4.2 MIM Absorption

The design of the MIM absorber is started considering optically thick bottom metal layer. The spacer dielectric (insulator) is chosen to be Al_2O_3 , ZnO and TiO_2 , all of which are transparent in the wavelengths of interest (NIR). Afterwards, initial simulations using Lumerical FDTD Solutions reveal that an insulator thickness of 30 nm to 50 nm results in peaks of absorption in the bottom metal in NIR spectrum. The simulations also suggested that absorption in NIR requires nanoparticles with diameters in the order of 100 nm.

As discussed in the Fabrication section under RTA method (chapter 3), ultra-thin metal films like gold and silver are not stable due to the surface forces at metal-air interface. For thicknesses on the order of 10 nm, the film is thermodynamically metastable and under some sort of excitation, the film will evolve by agglomerating into islands to minimize its surface area with air [83]. This process is known as dewetting. The size and morphology of the resulting nanoclusters (islands) on the surface highly depend on the layer beneath metal, the metal type and excitation parameters which are heating and cooling rates, anneal temperature and time. 10 nm Ag was deposited on the insulator via thermal evaporation, and a consecutive rapid thermal annealing (RTA) was carried out at an ambient N_2 flow rate of 120 sccm. The applied annealing steps can be broken down into heating, fixed annealing and cooling. The three applied annealing recipes as well as the scanning electron microscope (SEM) image of the resulting nanoparticles for three different recipes are given in Fig. 4.2. The 500°C annealing temperature in recipes was found by trial and error. From Fig. 4.2 it can be deduced that applying very fast heating rate (500°C/min) results in very non uniform particles (Fig. 4.2b and Fig. 4.2d). This arises from the fact that applying sudden heat creates high local stress gradients which pushes the start of agglomeration from defect sites between the metal and the underlying dielectric and it is very random. On the other hand, sudden cooling (500°C/min) results in a spike of strain shock in the film and the film does not have enough time to distend and thus they remain in more spherical shape (Fig. 4.2c and Fig. 4.2d) and small residues of very small particles remain on the surface. Thus, slow heating rate and high

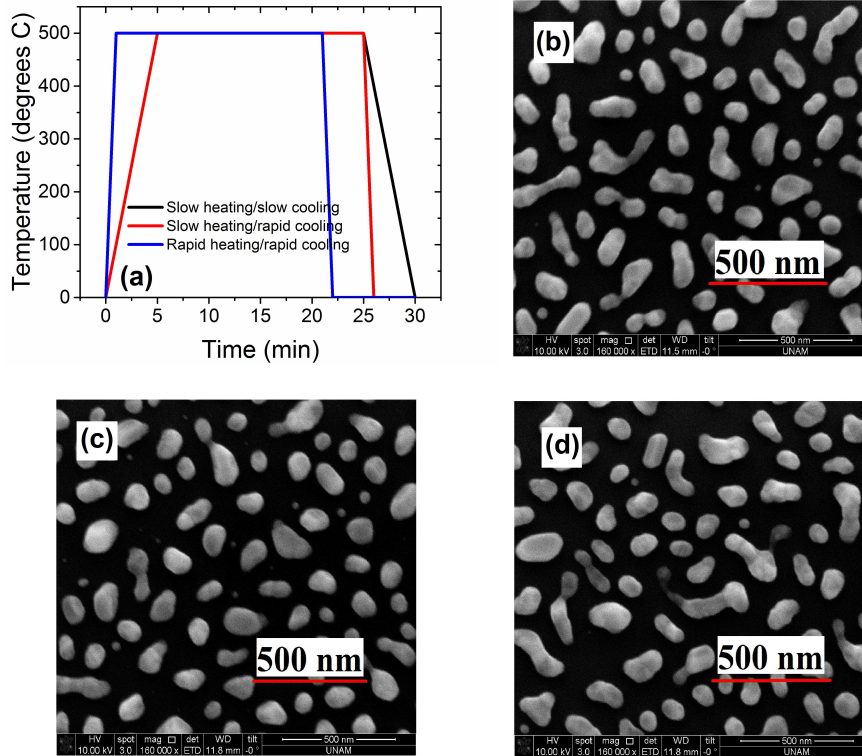


Figure 4.2: (a) Three applied RTA recipes of 500°C heat for 20 min with heating rate of 100 °C/min and cooling rate of 100 °C/min, heating rate of 100 °C/min and cooling rate of 500°C/min and heating rate of 500 °C/min and cooling rate of 500 °C/min respectively, SEM image of nanoparticles after (b) slow heating-slow cooling, (c) slow heating-rapid cooling and (d) rapid heating-rapid cooling [1].

cooling rate (Fig. 4.2c) is chosen due to reasonably uniform particles that it offers. The residues can be neglected since they are very small. Since there was no fast cooling mechanism in our RTA system, the film was allowed to reach to 200°C in 45 seconds and the sample is manually removed to room temperature afterwards. The size analysis of the particles from the chosen recipe of 100°C/min heating, 500°C annealing for 20 min and 500°C/min cooling rate (Fig. 4.2c) is illustrated in Fig. 4.3a. Figure 4.3a shows that the average nanoparticle diameter is approximately 100 nm. Moreover, since the thickness of the initial Ag film and the total nanoparticle areas (from the SEM image) are known, the average height of the particles can be estimated as 50 nm. It is worth pointing out that the obtained distributions are carried out on Al₂O₃ film to have similar results. Moreover, Al₂O₃ and other dielectrics of interest were deposited at 200°C

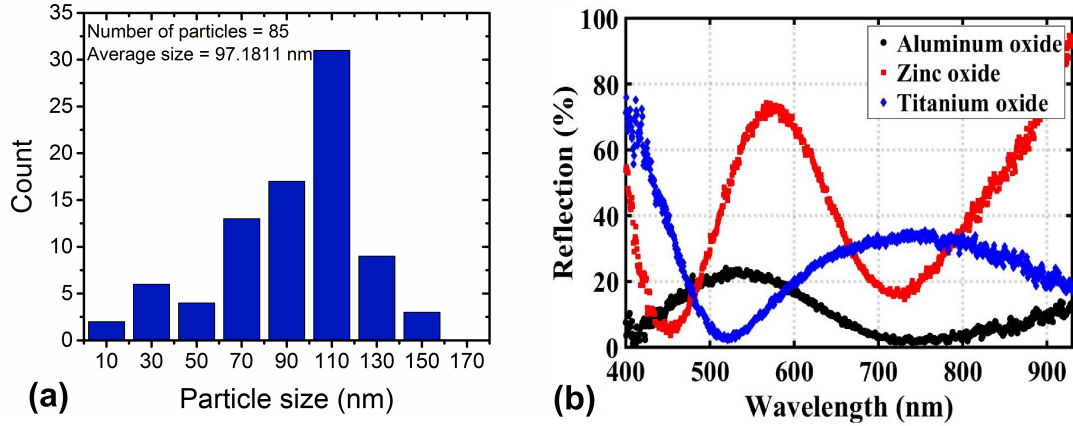


Figure 4.3: (a) particle size distribution analysis of the optimized RTA recipe for 10 nm deposited Ag film and (b) reflection of MIM absorber structure with Al absorbing metal, Ag nanoparticles and three different dielectric materials Al_2O_3 , ZnO and TiO_2 . [2, 3].

in ALD. The more the deposition temperature, the bigger the grain boundaries. It was experimentally observed that for example, when the dielectric is deposited at 150°C , since the grain boundaries are small, the dielectric cannot withstand the resulting stress and strain shock of RTA annealing and the dielectric breaks down.

In order to simulate the structure and calculate absorption, 3D simulation with Lumerical FDTD Solutions is used. First, our calculations reveal that simulating absorbing MIM yields the same results as the case when MIMIM is simulated unless the absorbing metal thickness is less than 20 nm. This is totally predictable since below 20 nm, the transmitted light through the absorbing metal will be significant. For the simulation of the nanoparticles, in order to obtain more accurate results, the SEM images of the particles are imported to Lumerical FDTD and an average height of 50 nm is given to the particles. The simulated area is $500\text{ nm} \times 500\text{ nm}$. The average size of particles periodically simulated does not yield accurate results (results not shown here). Moreover, transmission (T) vanishes in these structures and absorption (A) is simply $A = 1 - R - T = 1 - R$ where R is the reflectance. The reflectance simulation results for 30 nm Al, 40 nm different dielectrics and Ag nanoparticles of the optimized recipe are illustrated in Fig. 4.3b. The n, k data of the dielectrics are extracted using ellipsometer and

imported to Lumerical. The spectral shapes exhibit a red shift as the permittivity of the spacer dielectric (I_{spa}) in MIM stack. For the sample with TiO_2 for example, the second absorption resonance (reflection dip) falls out of our measurable range which is 400 nm to 1100 nm. The structure is optimized for Al_2O_3 which has the lowest k value between the deposited dielectrics in ALD. The n, k data of Al_2O_3 is provided in the Appendix. The most critical parameter in MIM absorbers for photodetection is absorption in the absorbing metal which should be maximized. The simulation of absorbers are similar to the case for different dielectrics discussed earlier. For the material parameters, Palik model [85] is used for chromium, aluminum and silver, and Johnson and Christy model [86] for gold. For Al_2O_3 the extracted n, k is applied. For the fabrication, thermal evaporator with chamber pressure of $2-4 \times 10^{-6}$ Torr is used. For the dielectrics, ALD is used and the deposition temperature is 200°C with an N_2 flow of 20 sccm. Al_2O_3 is deposited from Trimethylaluminum and milli-Q water precursors. The measurement of reflectance is carried out using home made reflection setup as discussed in chapter 3. The ALD deposition recipe is provided in the Appendix. Figure 4.4a and Fig. 4.4b show the simulated and experimental reflectance for MIM structures with Ag nanoparticles, 40 nm Al_2O_3 and four different absorbing metals. Once it is assured that the simulated and measured reflectance are congruent, the absorptions in the absorbing metals are calculated using absorption monitor in Lumerical FDTD and the results are illustrated in Fig. 4.4c. Besides, Fig. 4.4d displays the sample photos of fabricated MIM structures with four different absorbing metals that are obviously in agreement with the reflection results. The chosen metals are Al, Au, Ag and Cr. While the former three metals are widely used in plasmonic absorbers, Cr is rarely given the credit as a good absorbing metal due to high loss. Spectral reflection (experimental) results of Fig. 4.4a and Fig. 4.4b and those calculated computationally agree well. The little discrepancy between simulation and experiment results of reflection stems from the fact that the thickness of particles is assumed to be 50 nm for all of them in average which is not the case in practice. Additionally, there is generally a blue-shift in experimental reflection results compared to the simulation results which is attributed to the tarnishing of silver when the cooling is done rapidly by manually taking the sample out of the RTA chamber. This will be justified once

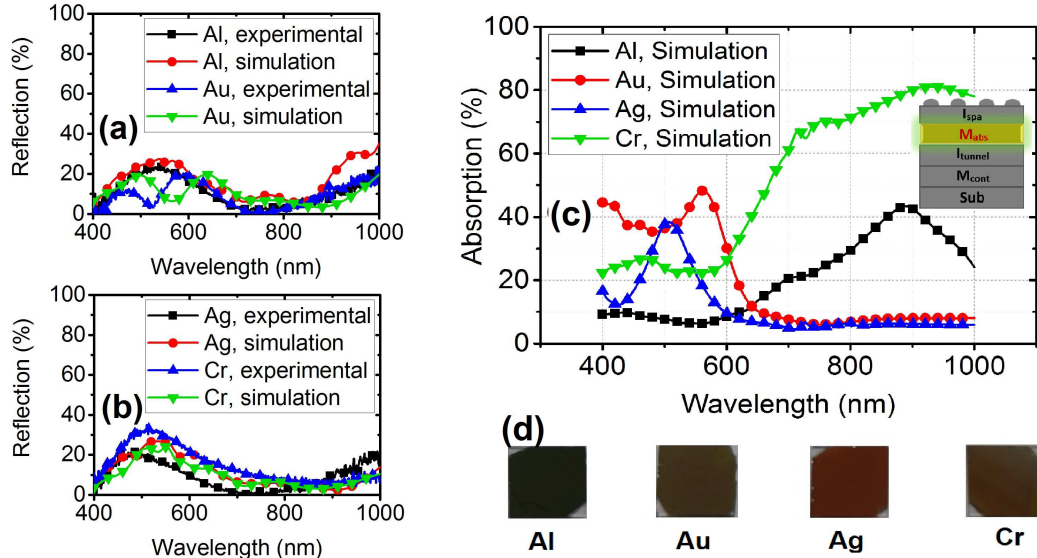


Figure 4.4: Measured and computational 3D simulation results of reflectance from a surface of MIMIM (Ag nanoparticles - 40 nm Al_2O_3 - 30 nm M_{abs} - 10 nm HfO_2 70 nm Ag bottom contact) with M_{abs} chosen to be (a) Aluminum and Gold, (b) Silver and Chromium, (c) simulated absorption percentage in different absorbing metals and (d) sample photos. Inset of (c) illustrates the layer being studied (i.e. absorbing metal) [2, 3].

more in the photoresponsivity results in the following sections. All of the samples show a highly decreased reflectance below 20% (high absorption) for most of the spectrum between 400 nm and 1000 nm. The absorption results of Fig. 4.4c demonstrate that Al and Cr show absorption peaks of 42 percent and 81 percent around 800 nm and 1000 nm, respectively while Silver and Gold are not desirable since they yield very low absorption beyond 600 nm. As discussed earlier, the broad absorption peaks are innate properties of random nanoparticle enhanced absorbers. The absorption in Cr is extended into NIR region which is the main purpose of this study and thus is the best material of choice.

Figure 4.5 displays the simulated E and H profiles for an MIMIM structure with Cr absorbing metal at 400 nm and 1000 nm. The mesh sizes are 15 nm in the x and y (lateral) directions and 3 nm in the z direction (perpendicular). The field profiles of all of the absorbing metals are analogous with small differences; thus, the results for Cr only are presented here. At a wavelength of 400 nm

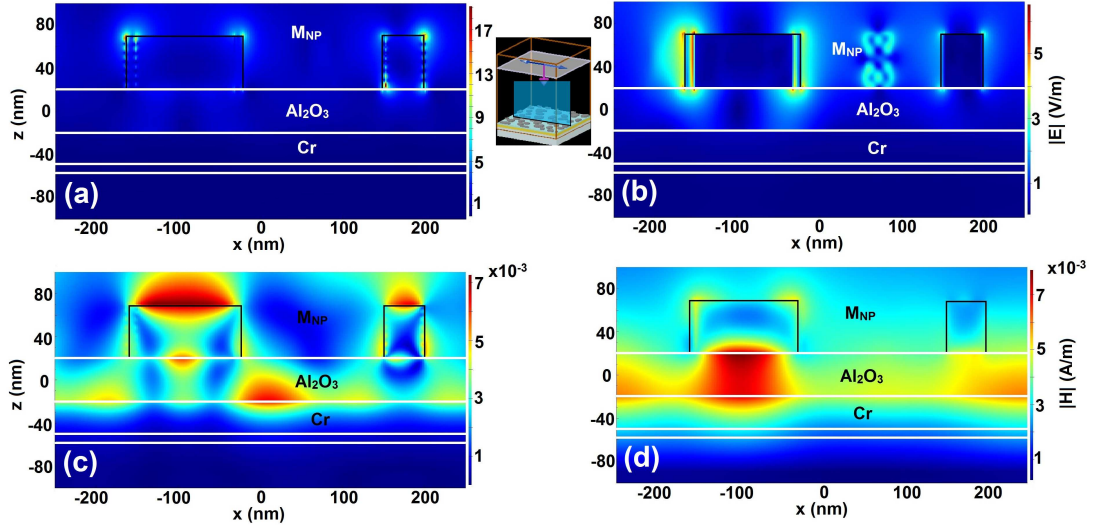


Figure 4.5: Computed field distributions at two different wavelengths. (a) E-field at 400 nm, (b) E-field at 1000 nm, (c) H-field at 400 nm and (d) H-field at 1000 nm for MIMIM structure with Chromium absorbing (middle) metal, at a cross section of the sample which includes and bisects two nanoparticles. The inset between the two E-field figures illustrates the cross section plane in the software environment [1, 2, 3].

(Fig. 4.5a and Fig. 4.5c) we observe higher order plasmon modes with confined field mostly within Ag nanoparticle/air interface which results in excitation of LSPs and absorption mainly occurs in Silver nanoparticles. On the other hand, at 1000 nm (Fig. 4.5b and Fig. 4.5d), however, the field is confined within the Ag nanoparticle/Al₂O₃ interface giving rise to absorption probability through excitation of SPPs in the metal. It is possible to mistakenly infer that the same field profiles may lead same absorption amounts in all absorbing metals which is wrong; there should be a material with high loss to absorb the confined field in the MIM plasmonic cavity. Cr provides more loss and is thus the best material of choice for these applications. An insightful tool to scrutinize higher absorption in Cr and Al is electric SPP quality factor of metals. SPP quality factor (Q_{SPP}) is defined as

$$Q_{SPP} = (\varepsilon')^2 / \varepsilon'' \quad (4.1)$$

where ε' and ε'' are respectively the real and imaginary parts of permittivity. Q_{SPP} for the four discussed absorbing metals are illustrated in Fig. 4.6 using the afore-mentioned material models. While there is little attention in literature

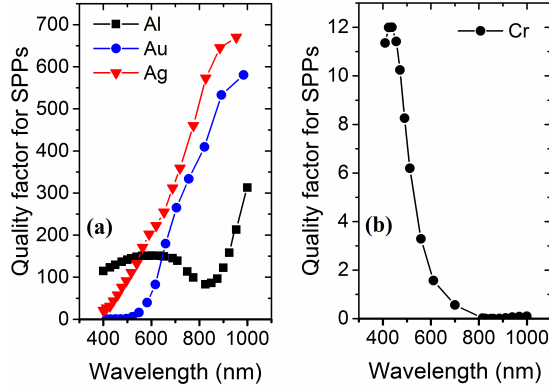


Figure 4.6: Q_{SPP} for (a) Al, Au, Ag and (b) Cr [2].

dragged to choosing the absorbing or scattering metals from the existing ones, the proposed concept fits best for such a purpose. In order for a metal to be a good absorber in a wavelength of interest, real permittivity must be low (to boost field penetration) and the complex permittivity should be high (high absorption). Applying this discussion, Al and specifically Cr show minima of SPP quality factor and are the most appropriate choices for the target wavelength range. While there is a relative minimum for Aluminum which accounts for increased absorption, the situation is more dramatic for Cr; the plasma frequency (real permittivity cross over of zero) of Cr occurs at 850 nm and as a result, it is the most suitable choice for absorption in NIR region. The opposite discussion would shed light on the choice of nanoparticles which are supposed to scatter light highly and have low loss. Therefore, Ag nanoparticles are also the reasonable choice due to their high SPP quality factor within 400 nm to 1000 nm wavelengths.

4.3 MIMIM Photodetection

After accomplishing absorption the EHP generation takes place and collection of the EHPs should be addressed which is designed to be done with a tunneling junction. It is also possible to have a semiconductor in contact with absorbing metal to form a Schottky junction. However, Schottky will lead to high dark current. Another concern is that since we are bound to the absorption up to

1100 nm in reflectance measurement setup, a semiconductor like Si has some absorption up to 1100 nm, where 1100 nm marks its bandgap edge. Therefore, if photocurrent is obtained, it will not be clear if the absorption is predominantly taking place in depletion region of Si or the absorbing metal. Tunneling junction is not efficient in hot EHP collection; however, for a proof of concept study it provides a good discussion to substantiate SPP excitation for photodetection.

Since Al and Cr proved better in absorption in NIR, only MIMIM photodetectors with these two absorbing metals were fabricated. The structures are AlHfO₂Al or Cr absorbing metalAl₂O₃Ag nanoparticles (from bottom to top); two other samples with the same structures without Ag nanoparticle layer (MIMI) are fabricated as references to the first two in order to emphasize the effect of plasmonic nanoparticle layer. One important design parameter for the junction is the substantial role of absorbing metal thickness in photocurrent. If the absorbing metal is chosen to be too thick, ohmic loss would degrade photoresponsivity dramatically. On the other hand, if this metal is too thin, there will be little absorption and some absorption also would take place in the bottom contact metal and two competing photocurrents would decrease the overall photocurrent. This trade-off led us to choose 30 nm to compensate for both effects. This amount is larger than the skin depths of metals in the wavelengths of interest which is approximately 20 nm [52].

The two remaining layers in the bottom are the tunneling insulator and the bottom contact metal. From the available insulators in ALD system, we have HfO₂ and Al₂O₃. In the fabrication process, during the developing process using AZ400K, Al₂O₃ is chemically etched. This effect is deteriorated since the thickness of the insulating layer is in the order of 5 nm to allow for tunneling. Therefore, HfO₂ is chosen as the tunneling insulator. For the thickness of this layer, the main trade-off is that thick insulator (greater than 5 nm) blocks tunneling current dramatically and a thin one (less than 3 nm) results in shorting of the absorbing and bottom contact metal layers in some of the features. Therefore 4 nm is chosen. Also, HfO₂ is a high-k dielectric which would provide high electric field to facilitate tunneling. As for the bottom contact metal, we prefer an offset between M_{abs} and M_{cont} layers. This choice can block the dark current and

allow only the hot EHPs to pass which can help us corroborate that the measured current is a result of EHPs. The tunneling MIM junction of Cr absorbing metal is schematically sketched in Fig. 4.7a. The junction for Al is also similar. The

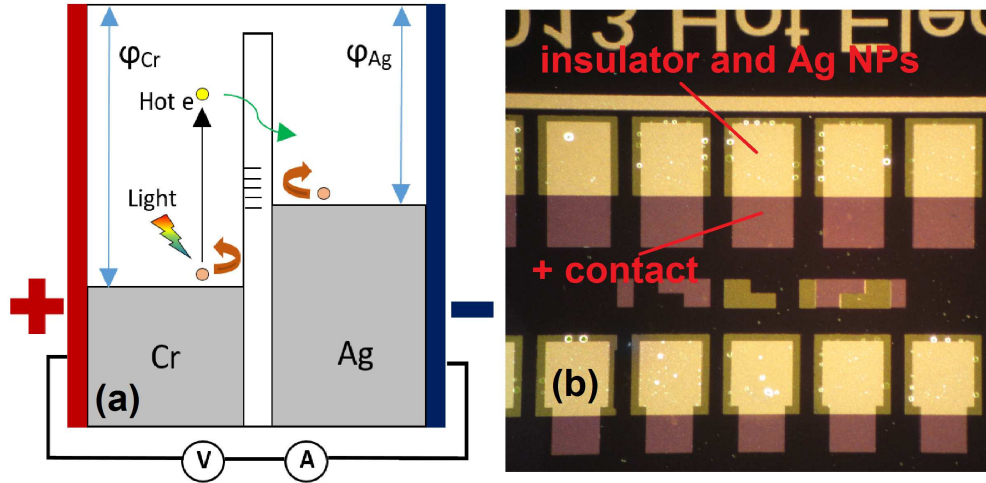


Figure 4.7: (a) Schematic of the tunneling junction and (b) photo of the sample under microscope [1].

fabrication of the photodetector starts with cleaning Si substrate in Acetone, Isopropanol and de-ionized water for 10 minutes each using ultrasonic agitation. A 70 nm Ag bottom contact metal is deposited with thermal evaporation at a base pressure of $2-4 \times 10^{-6}$ Torr. Then the sample was masked with a small margin to expose the bottom contact metal. A deposition of 4 nm HfO_2 at $200^\circ C$ from Trimethylhafnium and milli-Q water precursors with an N_2 flow of 20 sccm is carried out afterwards. The deposition recipe with Savannah S100 is provided in the Appendix. Then, a lift off process was carried out to have the absorbing metal. HMDS and AZ5214E photoresist were spin coated and after exposure in aligner and developing in AZ400K solution, a 30 nm deposition of Cr (or Al for the other sample) using VAKSIS thermal evaporator followed. Then the sample was dipped in Acetone which finished the lift off process. Then, 40 nm Al_2O_3 was deposited in the same conditions in ALD using Trimethylaluminum and milli-Q water. After deposition, a patterning process was done to expose the absorbing metal contact this time. Then ICP was used to dry etch the 40 nm Al_2O_3 from the unwanted regions. Finally, 10 nm Ag was deposited using thermal evaporator and RTA was applied to obtain nanoparticles. The photo of the sample under

microscope is illustrated in Fig. 4.7b where M_{abs} area is $300 \times 600 \mu\text{m}^2$ and the I_{spa} area is $350 \times 350 \mu\text{m}^2$.

4.4 Discussion

The home made setups as discussed in chapter 3 were used to measure spectral photoresponsivity. In order to measure photoresponsivity, a DC bias should be applied. High bias results in high photocurrent due to increased electric field over the barrier while it is also concomitant to high power loss with increased dark current. Therefore, an optimum point should be chosen for this trade-off. By increasing the bias gradually, higher photocurrent is observed. After a specific value, however, there is no significant change in photocurrent while the dark current is rising. This critical point was found to be -50 mV for MIMI(M) devices with Al and Cr (The bias convention of Fig. 4.7a is used). The $\text{Log}(|I|)$ -V curves of devices with Al and Cr are illustrated in Fig. 4.8a and Fig. 4.8c. The spectral photoresponsivity curves of MIMIM devices with and without Ag nanoparticles for Al and Cr (at a negative bias of 50 mV) are respectively depicted in Fig. 4.8b and Fig. 4.8d. Figures 4.8a and 4.8c suggest that the dark current is 5 nA and 7 nA for devices with Al and Cr absorbing metals which accounts for a dark current density of $0.028 \mu\text{A}/\mu\text{m}^2$. The photocurrent results are in accordance with calculated absorption results of Fig. 4.4. The smoother results of MIMIM with Cr absorbing metal is due to higher photoresponsivity opposed to that of Al which is close to minimum measurable current values.

Photoresponsivity of MIMIM device with Al exhibits a peak value of $36.84 \mu\text{A}/\text{W}$ at 850 nm which is 29 times the peak value of same device without nanoparticles (the reference device for Al case). The exemplar performance occurs for the MIMIM device with Cr absorbing metal which has a peak photoresponsivity of $96.24 \mu\text{A}/\text{W}$ at 980 nm which represents 3 times enhancement compared to the peak value of same device without nanoparticles (the reference device for Chromium case). This is also a 2.6 times increase compared to MIMIM device with Al. The full width at half maximum is more than 300 nm due to the use

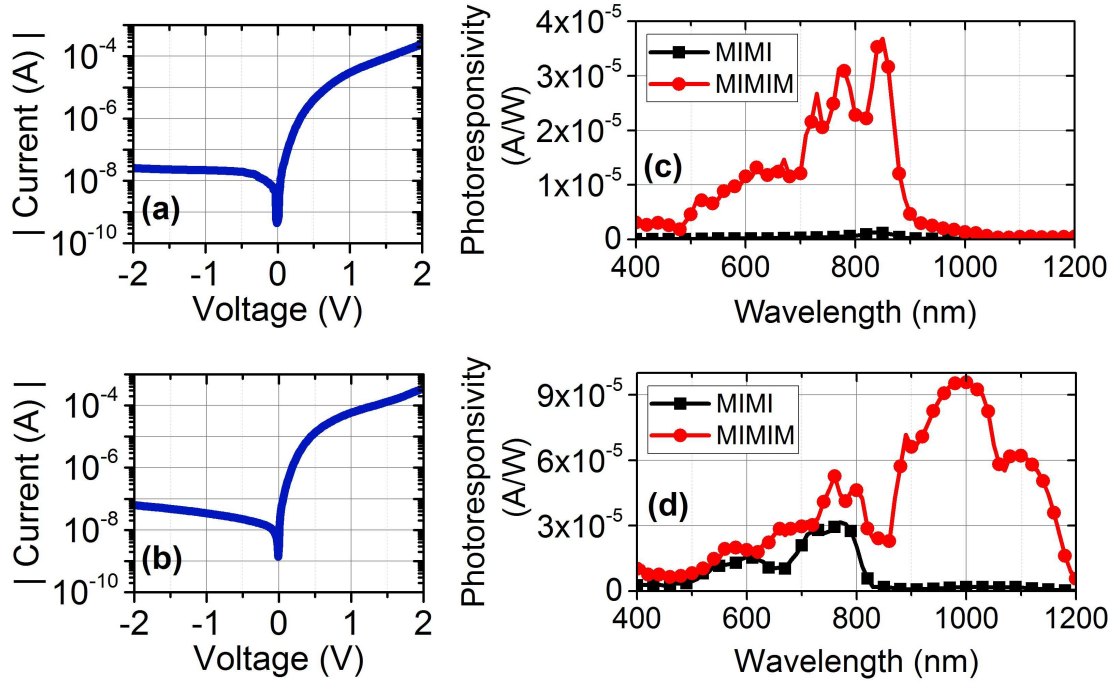


Figure 4.8: IV characteristics of MIMIM (Ag nanoparticles - Al_2O_3 - M_{abs} - HfO_2 - Ag negative bottom contact metal) devices with (a) Aluminum absorbing metal and (b) Chromium absorbing metal, photoresponsivity at applied negative 50 mV bias for MIMI (without Ag nanoparticles) and MIMIM devices respectively with (c) Aluminum absorbing metal and (d) Chromium absorbing metal. [2].

of random sized nanoparticles. Thus, our best result justifies almost an order of magnitude enhancement compared to MIMI device with Aluminum, which itself has a little absorption peak around 850 nm already. Additionally, our Cr MIMIM result exhibits approximately two orders of magnitude enhancement in photoresponsivity over the reported spin-coated MIMIM structures [76].

One last remark is that the photoresponsivity curves follow the simulated absorption curves quite acceptably and Fig. 4.9 represents absorption and photoresponsivity curves together. The only discrepancy is a red-shift in photoresponsivity results compared to calculated absorption results which is as stated earlier, due to tarnishing of Ag nanoparticles in experiments.

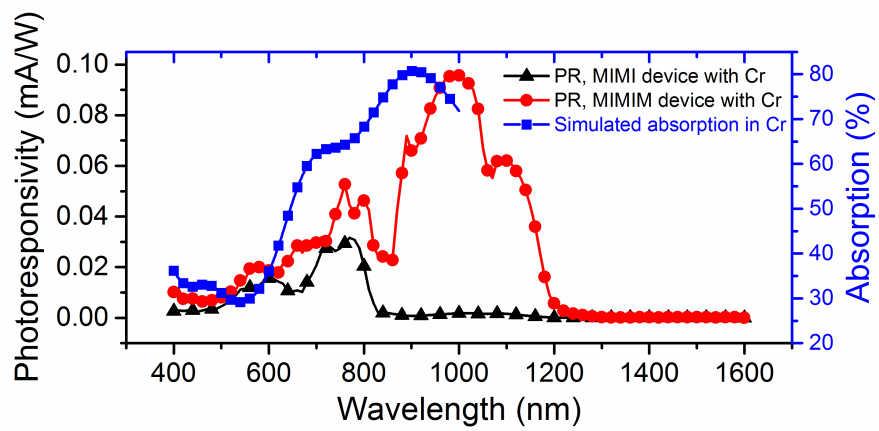


Figure 4.9: (a) Calculated absorption in the absorbing metal and spectral photoresponsivity at applied negative 50 mV bias for MIMI and MIMIM devices with chromium absorbing metals. [1].

Chapter 5

MIMI Cavity Absorbers

5.1 Introduction

Increasing the breadth of absorption is one of the motivations in literature. Michael *et. al.* proposed an MIM structure containing a combination of multi-harmonic geometries that brings together different absorption peaks from different geometries in a super cell to achieve broadband absorption [19]. However, such multi-geometric absorbers are fabricated using electron beam lithography (EBL) which is slow, expensive and applicable to small areas. Other innovations in broadband absorbers include using layered tandem cell structures that are reasonably simple while fulfilling figures of merit of perfect absorbers to a large degree which despite being lithography free, require deposition of many layers [20]. Albeit having good performance, the many layer deposition creates reproducibility problem. One of the broadest absorption results reported so far is the use of pyramid structure composed of MI layers which illustrates nearly 100% absorption from 1 μm to 14 μm [21]. This structure has a very broad absorption response due to the fact that the middle insulator layer is gradually changing in thickness in a pyramid which brings together the response of insulator layers with different thicknesses. Still, the fabrication of a metamaterial pyramid is challenging but possible. A very simple and subtle absorber design

is using thin deposited MI layers (most frequently MIMI) with lossy metals to form Fabry-Perot cavities that trap light. This method is lithography-free and applicable to large areas and requires rather few different types of materials to be deposited which is a reasonable trade-off between complexity of structure and response. These structures can also exhibit extended bandwidth into mid-infrared (MIR) when the number of MI layers is increased. Not only do MIMI absorbers eradicate the need for EBL but also they outperform most of the plasmonic absorbers. One of the initial reports that attracted attention for Fabry-Perot cavity absorbers was reported by Kats et al. in which nanometer thick anti-reflection coatings (ARC) resulted in absorption in a simple two-layer structure [22]. In order to enhance the functionality of these absorbers, several metals and insulators were then utilized to get ultra-broadband perfect light absorption. Some of them are W-Al₂O₃ [23], Cr-SiO₂ [24], Ag-Si [25], Ni/Ti-SiO₂ [26], Au-PMMA-Cr [27] and Cu-SiO₂ [28]. The broadest over 90% absorption is reported for an MIMI absorber with Au-Al₂O₃-Cr-Al₂O₃ (from bottom to top) layers which is from 400 nm to 1400 nm [29]. Most of the competitive absorbers are MIMI structures which have been studied in recent years. However, these absorbers are not optimally engineered to have broadest possible absorption and material choice is an issue of study. In this chapter, we will provide a versatile method to obtain the broadest absorption in VIS-NIR spectrum to the best of our knowledge. We focus and analyze the selection of each metal layer to achieve high absorption. Before choosing the metal layers, first the geometry (*i.e.* thickness) of the layers is optimized using simulation and TMM method. Then the most lossy metal is chosen for the middle thin absorbing layer. Afterwards, using the equivalent wave impedance of the structure and matching it to the impedance of free space, ideal permittivity values versus wavelength is obtained which reveals the bottom reflector metal material.

5.2 Calculation and Analysis

Firstly, the schematic of the MIMI absorber structure is illustrated in Fig. 5.1a.

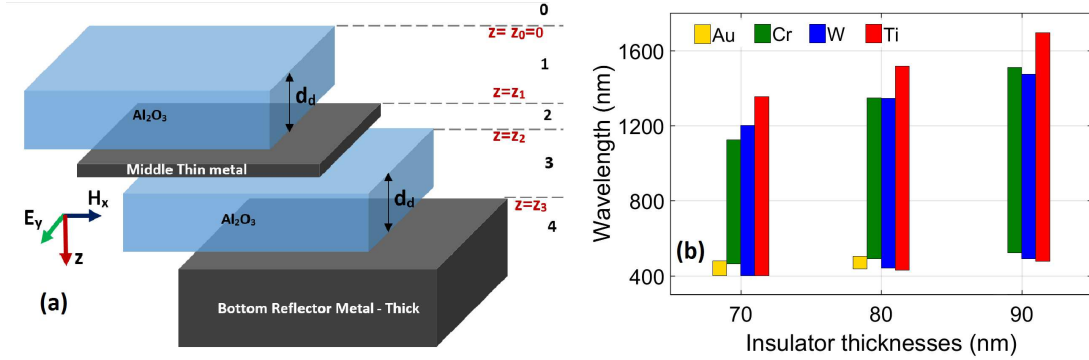


Figure 5.1: (a) Schematic of the MIMI structure and (b) over 90% absorption bandwidth for four different double metal-Al₂O₃ (MIMI) stacks where the middle thin metals are 10 nm thick. The insets of Fig. 1 (a) illustrate field directions, the direction of propagation (TE) and the layer and boundary numbers.

The absorption in these absorbers are a result of trapping the incoming light in the cavity formed by the middle thin metal layer, Al₂O₃ and the bottom thick reflector metal. The top dielectric serves as an ARC which couples the incoming light effectively (with minimum reflection) to the cavity. Afterwards, the light trapped in the cavity decays in the metal layers of the cavity in such a low quality factor cavity. In order to provide a preface into these absorbers, four different absorbers are investigated. These absorbers include double pairs (MIMI) of Au-Al₂O₃, Cr-Al₂O₃, W-Al₂O₃ and Ti-Al₂O₃. As discussed earlier, two critical figures of merit are breadth and the high value of absorption. Therefore, a limit of over 90% absorption is applied to these structures. The simulation results (with Lumerical FDTD) of these four pairs for over 90% absorption bandwidth are depicted in the bar graph of Fig. 5.1b for four different insulator thicknesses. It should be noted that the thickness of insulators d_d are equal in all MIMI structures in this chapter. Also, the thickness of the middle thin metals are 10 nm and the bottom metal is optically thick.

From the results of Fig. 5.1b it can be deduced that Au is not at all suitable for broadband absorption which is obvious given the little lossy behavior of this material for NIR wavelengths. Ti, on the other hand has the best performance in terms of broadband over 90% absorption. Moreover, 70 nm and 90 nm Al₂O₃ are not ideal; the formers suffer form low bandwidth into NIR and the latter suffer from loosing the first segment of VIS. Thus, 80 nm is the optimum choice

of insulator thicknesses.

TMM method is used to vindicate simulations numerically. As discussed in chapter 2, a solution with backward and forward propagating waves is supposed. For each layer in MIMI structure, d_i , $\gamma_i = \alpha_i + j\beta_i = j\omega\sqrt{\mu_i\varepsilon_i}$, μ_i and ε_i ($i=0, 1, 2, 3, 4$) represent the thickness, complex propagation constant, complex permeability and complex permittivity of layer while ω stands for angular frequency. The notations demonstrated in Fig. 5.1a are used. While TE illuminating wave is assumed initially, since the angle of incidence is set to zero, the results can also be considered a TEM wave solution. A transfer matrix is designated for each layer as

$$\begin{pmatrix} A_i \\ B_i \end{pmatrix} = (M_i)_{2 \times 2} \begin{pmatrix} A_{i+1} \\ B_{i+1} \end{pmatrix} \quad (5.1)$$

$$(M_i) = \begin{pmatrix} \frac{1}{2} \left[1 + \frac{\gamma_{i+1} \mu_i}{\gamma_i \mu_{i+1}} \right] e^{(\gamma_{i+1} - \gamma_i)z_i} & \frac{1}{2} \left[1 - \frac{\gamma_{i+1} \mu_i}{\gamma_i \mu_{i+1}} \right] e^{-(\gamma_{i+1} + \gamma_i)z_i} \\ \frac{1}{2} \left[1 - \frac{\gamma_{i+1} \mu_i}{\gamma_i \mu_{i+1}} \right] e^{(\gamma_{i+1} + \gamma_i)z_i} & \frac{1}{2} \left[1 + \frac{\gamma_{i+1} \mu_i}{\gamma_i \mu_{i+1}} \right] e^{-(\gamma_{i+1} - \gamma_i)z_i} \end{pmatrix} \quad (5.2)$$

where A_i and B_i represent the amplitudes of forward and backward propagating waves respectively. Since for the bottom reflector metal layer, transmittance is zero, the ratio of $R = |A_0/B_0|$ would give absorption ($A = 1 - R - T = 1 - R$). The reflectance and thus absorption can be calculated assuming $B_4=0$ due to optically thick bottom metal that does not transmit light as

$$\begin{pmatrix} A_0 \\ B_0 \end{pmatrix} = (M_0)(M_1)(M_2)(M_3) \begin{pmatrix} A_4 \\ B_4 \end{pmatrix} \quad (5.3)$$

The permittivity of dielectric layers (Al_2O_3) are approximately to be $\varepsilon_1 = \varepsilon_3 = \varepsilon_d = 1.7$. The permittivities of the metal layers are imported to Matlab from Palik model permittivities [85].

5.3 Results and Discussion

The thickness of the Al_2O_3 layers were optimized as 80 nm in the previous section. One thickness parameter remaining to be optimized is the thin metal layer thickness (the bottom reflector metal is optically thick). Ruling out Au due to its

gloomy performance as shown in the results of Fig. 5.1b, the absorption results for Ti, Cr and W in MIMI structures with thin metal layers of 5 nm, 10 nm, 15 nm and 20 nm are provided in Fig. 5.2. The thicknesses of Al_2O_3 layers are 80 nm and the metal layers are the same in each panel.

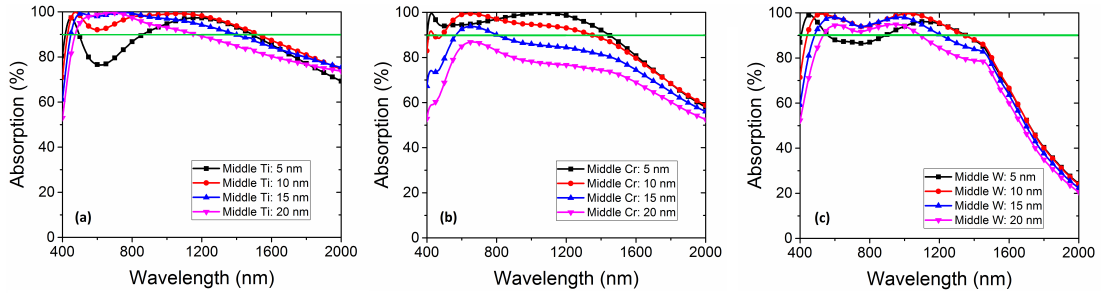


Figure 5.2: Absorption versus wavelength of double MI pairs (MIMI) with $d_d = 80$ nm and thick bottom metals and the same middle thin metal materials of 5 nm, 10 nm, 15 nm, and 20 nm thick (a) Ti, (b) Cr, and (c) W. The green line denotes 90% limit for absorption.

From the results of Fig. 5.2, it is concluded that Ti has the best performance as stated earlier. 5 nm thin layer in MIMI structure results in little dissipation of light which allows the reflected light from the bottom metal to have high enough power to penetrate the thin metal and get transmitted which is detectable as dips in the absorption curves in all metals. On the other hand, 15 nm and 20 nm thin metal thicknesses result in reduced breadth and peaks of absorption which is due to weak coupling of the light to the cavity. Therefore, 10 nm is the optimal choice of thickness for thin metal layer.

In order to further delve into the reason of Ti showing superior performance, the contribution of different layers in MIMI structure can be taken into account. The most important dissipation takes place in the thin metal layer. This phenomenon is indicated in Fig. 5.3a which shows the simulated contour plot of absorption percentage in different layers of our the MIMI absorber with Ti and Al_2O_3 layers. Therefore, this layer must be chosen as the most lossy metal possible in VIS-NIR spectrum. In order to point out the most lossy metal, a simple but insightful simulation is carried out which shows the absorption in infinite slabs of some lossy metals in VIS-NIR spectrum (400 nm to 200 nm) as displayed in Fig. 5.3b. The result for Au is also provided so that a fair comparison between lossy metals

and a non-lossy metal such as Au can be conducted. These results reassure that Ti is the best metal of choice for at least the thin metal layer which should exhibit extreme loss.

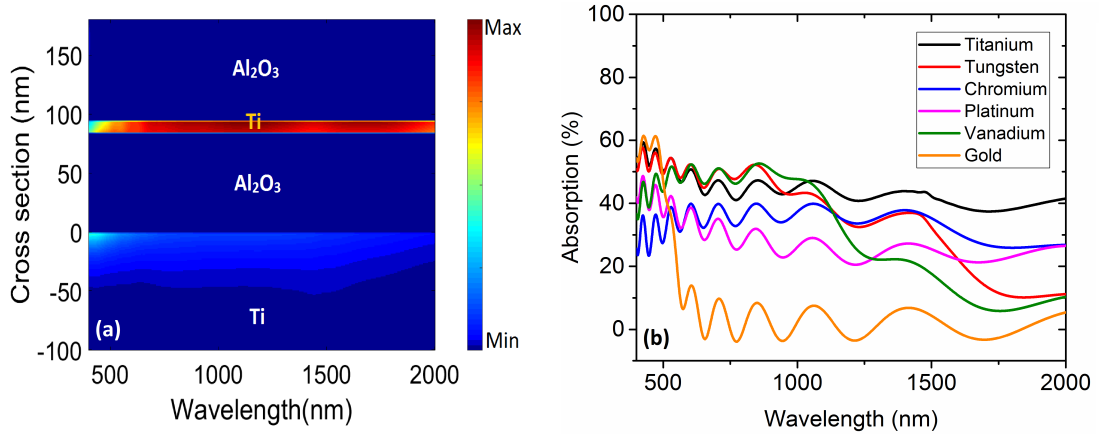


Figure 5.3: (a) Simulated contour plot of absorption in a cross-section of the MIMI sample with optimum parameters (thin metal thickness of 10 nm and $d_d = 80$ nm) and (b) simulated absorption versus wavelength for infinite slabs of some metals.

As discussed earlier, the incident light is coupled into the MIMI system with the help of a top ARC layer which assures minimum reflection. Afterwards, it is partially absorbed in the thin metal layer and partially coupled into the cavity formed by the bottom MIM part of the structure. Inside this cavity, the light goes through several back and forth paths and since its intensity is reduced in the beginning, it cannot surpass the thin metal and get reflected to air. Thus, it gradually decays only inside the two metal layers due to the lossless nature of Al_2O_3 . Besides, Fig. 5.3a leads to the conclusion that the first part of absorption in lower wavelengths is mostly due to the loss in the bottom thick metal and the second one is mostly a result of absorption in the thin middle metal layer.

A strong analysis tool to investigate MIMI absorbers is the application of equivalent wave impedance matching to them. If the wave impedance of the structure is matched to that of air, there will be perfect coupling of light to the structure and since there is a cavity, this phenomenon will finally yield perfect absorption. In previous works reported for MIMI absorbers, the bottom metal is deemed to be an insignificant metal where the only specification for it is being a good reflector.

However, since all layers contribute to the equivalent impedance, this assumption is not viable. Up to this point the optimized layers and thicknesses are two 80 nm Al_2O_3 layers and a 10 nm Ti thin metal layer between them. Therefore, the final optimization is dedicated to the material selection for the thick bottom reflector metal. We first compute the overall normalized equivalent wave impedance of the structure where all optimized parameters are known except for the material (permittivity values) for the bottom thick reflector metal. Setting this equivalent normalized impedance to the impedance of air (*i.e.*, one, due to normalization), the ideal permittivity values for the bottom metal can be extracted. As stated in chapter 2, the normalized effective impedance is calculated using the transfer matrix method as discussed earlier in chapter 2 derived by [28, 29]

$$Z_T = \frac{A_1 + A_2 n_R}{B_1 + B_2 n_R} \quad (5.4)$$

where

$$A_1 = n_d n_m \tan^2(\varphi_d) + n_d n_m \varphi_m (n_d^2 + n_m^2) - n_d^2 n_m \quad (5.5)$$

$$A_2 = -j n_m^2 \varphi_m \tan^2(\varphi_d) + j 2 n_d n_m \tan(\varphi_d) - n_d^2 \varphi_m \quad (5.6)$$

$$B_1 = -j n_d^4 \varphi_m \tan^2(\varphi_d) + j 2 n_d^3 n_m \tan(\varphi_d) + j n_d^2 n_m^2 \varphi_m \quad (5.7)$$

and

$$B_2 = n_d^2 n_m \tan^2(\varphi_d) + n_d \varphi_m (n_d^2 + n_m^2) \tan(\varphi_d) - n_d^2 n_m \quad (5.8)$$

In these equations, subscript R , m and d stand for the back reflector metal, middle thin metal and the dielectrics. $\varphi_i = j\gamma_i d_i$ represents the phase shift coming from each layer and γ , d and n are the complex propagation constant, thickness and complex refractive index of layers respectively. In order to simplify the derivation of Eq. 5.4, it is assumed that $\varphi_m = j\gamma_m d_m \ll 1$ due to very thin layer of middle metal (10 nm) in MIMI structures which leads to $\tan(\varphi_m) \approx \varphi_m$. Applying $Z = 1$ condition on Eq. 2.28 and considering optimum thicknesses and material parameters for the other three layers, it is possible to obtain the ideal refractive index (n_R) of the optically thick bottom layer that we assumed to be unknown. Using the relation $\varepsilon_{rR} = n_R^2$, the permittivity of an ideal material for the bottom metal is sketched in Fig. 5.4a.

The closer the material relative permittivities to the ideal values, the broader and more perfect the absorption will be. The real and imaginary parts of some

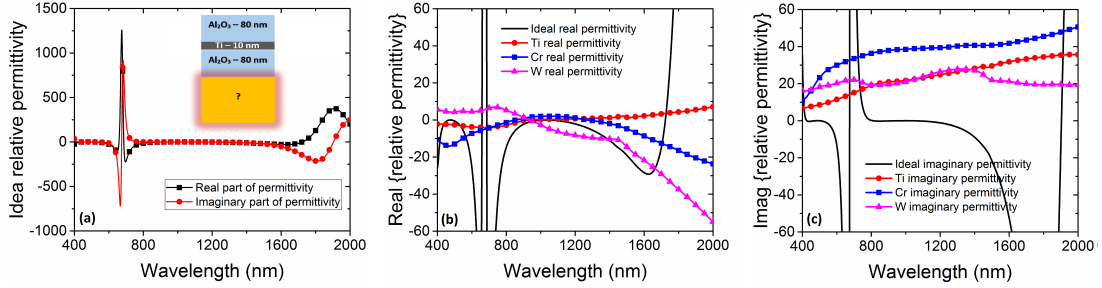


Figure 5.4: (a) Calculated ideal real and imaginary parts of permittivity for bottom reflector thick metal, (b) ideal real relative permittivity versus real parts of relative permittivity of Ti, Cr, and W and (c) ideal imaginary relative permittivity versus imaginary parts of relative permittivity of Ti, Cr, and W. The inset of Fig. 4 (a) shows the known and unknown calculation parameters.

metals are provided in Fig. 5.4b and Fig. 5.4c respectively. It is deduced from these figures that the closest metal of choice for the ideal relative permittivity values is W for the bottom reflector metal. This might seem counter intuitive due to the fact that an MIMI structure of Al₂O₃-Ti-Al₂O₃-W outperforms Al₂O₃-Ti-Al₂O₃-Ti. The optimized structure is again simulated for the best Al₂O₃ thickness using both FDTD simulation and TMM implementation. Moreover, the optimum device is fabricated and the experimental measurements including normal absorption using FTIR and the angled incidence responses using ellipsometer are carried out. Fig. 5.5 illustrates all the mentioned data together with the FIB image of the cross section of the device. The simulated and calculated absorption as well as the experimental results are provided together in Fig. 5.5d for the sake of comparison. The simulation, calculation, and experimental absorption results demonstrate over 90% absorption from 400 nm to 1705 nm, 400 nm to 1685 nm and 400 nm to 1642 nm, respectively. The absorption is retained over 90% at normal incidence onto the MIMI sample from 400 nm to 1642 nm which is close to the numerical results estimated by simulation and TMM. The response for different incident angles (θ) on the sample for TE and TM polarizations emphasize the fact that the sample has quite well absorption performance in angled illumination as well. The fabricated optimum sample deviates a little from the simulation and calculation results. This is attributed to the exact thickness of layers which is found to be 82 nm for Al₂O₃ layers and 9.5 nm for Ti. The thicknesses for the dielectric and Ti layers are calculated from the results of

spectroscopic ellipsometry and FIB cross section image presented in Fig. 5.5c.

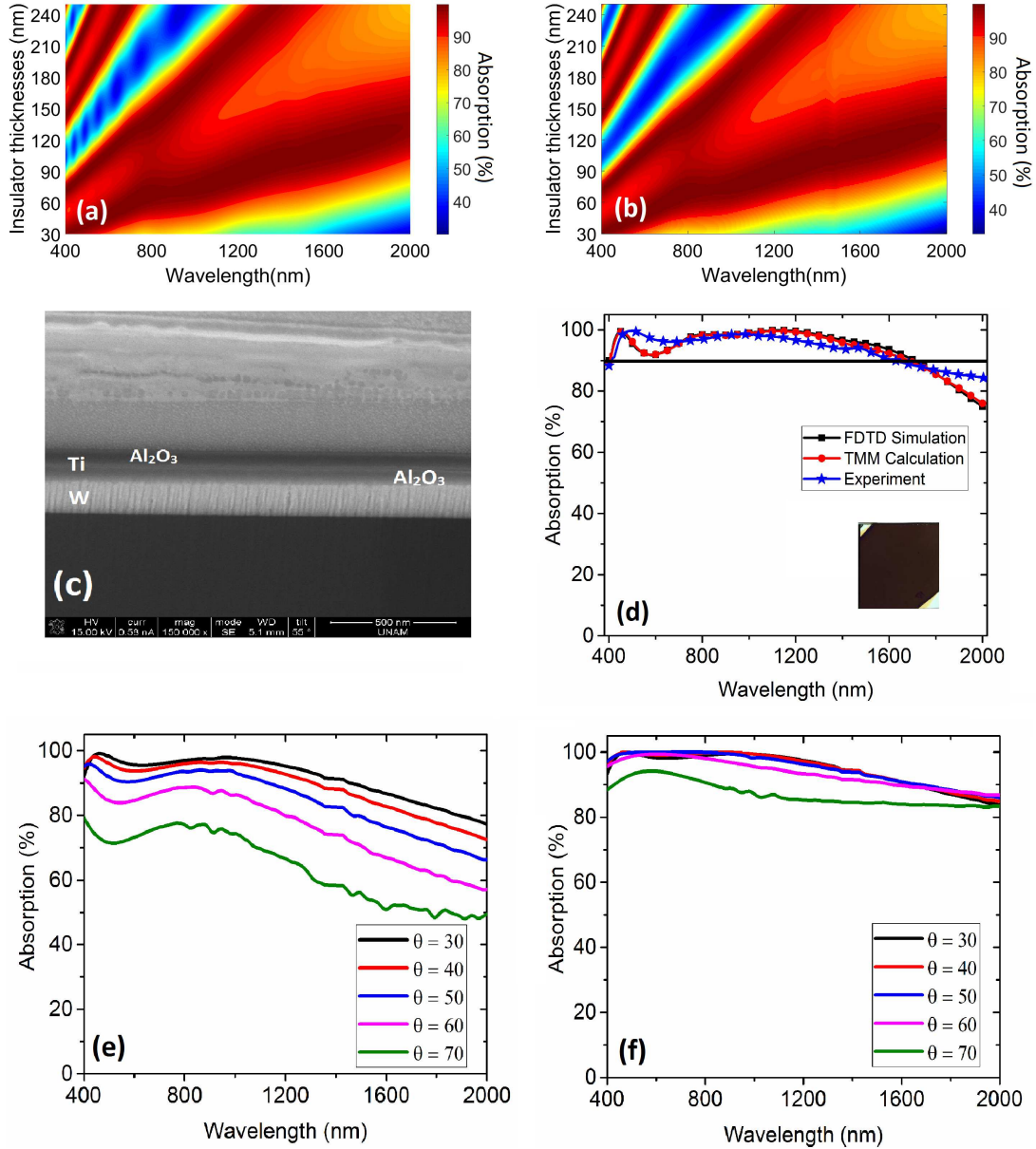


Figure 5.5: (a) Simulated absorption versus the wavelength and dielectric thicknesses (d_d) for the optimum MIMI sample with $d_{Ti} = 10$ nm, (b) calculated TMM counterpart of part (a), (c) cross section FIB image of the fabricated sample, (d) measured, simulated, and calculated (TMM) absorption at normal incidence, absorption of the fabricated sample (e) measured at different incidence angles (θ degrees) for TE polarization and (f) measured at different incidence angles (θ degrees) for TM polarization. The inset of Fig. 5 (d) shows the sample photo.

Chapter 6

Conclusion

After providing the necessary background for the theoretical framework, fabrication and characterization methods in chapters 2 and 3, some critical issues in absorbers and photodetectors are addressed. In chapter 4, plasmonic absorbers in VIS-NIR region based on metal-insulator stacks are investigated. Dewetting is used as a method for fabrication of plasmonic top metal layer which is cost and time effective and applicable to large areas and curved surfaces in contrary to EBL method. It also supports broad response due to random sized nanoparticles that it produces. Quality factor for SPP are introduced as a strong tool for optimization of plasmonic absorbers. Our results emphasize a counter intuitive metal, Cr, as a plasmonic absorber that can support SPPs. Lumerical FDTD is used to simulate and study the contribution of different layers in plasmonic MIM absorbers with the main focus on absorption in the bottom metal. SPP resonances at NIR wavelengths demonstrate the capability of these absorbers for photovoltaic applications. In an MIM structure composed of Ag nanoparticles-Al₂O₃-Cr, an absorption peak of 82% is observed in Cr at 850 nm and FWHM of 1000 nm (600 nm to 1600 nm) which illustrates the high potential of it to be tailored to NIR photodetectors. We point out Cr as an efficient absorbing metal due to high loss and suitable plasma frequency that happens in NIR region rather than UV for other metals of choice here. As a follow up study, MIMIM

photodetectors were studied which benefited the mentioned MIM plasmonic absorbers integrated on top of another insulator-metal layer. The photodetectors were engineered such that the dark current was suppressed and the photocurrent mechanism was based on tunneling of hot electrons. In the MIMIM structure, light falling on the particles excites SPPs in the middle absorbing metal. The non-radiative decay of SPPs results in hot EHPs and hot electrons are directed to the bottom metal by tunneling. The resulting absorption and photocurrent curves are highly in agreement. Our photodetector design manages to decouple absorption and photocollection parts which facilitates design of efficient photodetectors by engineering each layer independently. The spectral photoresponsivity shows a peak of approximately 0.1 mA/W which is two orders of magnitude enhanced compared to similar reports. The dark current is only 7 nA for devices with areas of $300 \times 600 \mu m^2$.

In another attempt, a perfect (over 90%) absorber was experimentally demonstrated between 400 nm and 1640 nm which is the broadest one between MIMI absorbers in literature to the best of our knowledge. The optimized structure is 80 nm Al_2O_3 - 10 nm Ti - 80 nm Al_2O_3 - thick W (from top to bottom). This method is lithography-free and large scale compatible and works on the basis of low quality factor cavities. The choice of each layer material and thickness was investigated in detail using FDTD simulations and TMM numerical calculations. The significance of metallic layer materials were pointed out in their contribution to the overall absorption. Besides, wave impedance matching was used to match the equivalent impedance of the MIMI structure to air which affirms perfect coupling of the wave to the cavity. This approach in general is a versatile method to obtain perfect and broadband absorbers.

As the future studies in the direction of this thesis two prominent ones can be considered for MIMIM photodetectors and MIMI absorbers. For MIMIM photodetectors, a symmetric metal work function photocurrent tunneling junction with thinner tunneling oxide can be designed to enhance the photoresponsivity to a great deal. Besides, the absorbing MIM junction can also be integrated on top of a semiconductor to form MS Schottky photocurrent junction which would increase photoresponsivity due to higher capability of Schottky in hot EHP collection. In terms of MIMI absorbers, since the loss takes place in the middle thin

(on the order of 10 nm) metal, it is possible to design efficient NIR photodetectors based on them. As an example, a TCO can be used instead of insulators and by applying bias in the top two layers (thin metal and TCO) one can engineer and obtain photocurrent. The prominence of this design is due to very high absorption in the middle thin metal in NIR region. Since the light is confined in a thin metal layer, there exists the possibility of generation of hot EHPs which would be in very close vicinity to the junction. This will enhance the collection probability of hot EHPs. However, low defect TCO will remain as a challenge due to the fact that TCOs are conductive on the basis of defects (frequently oxygen vacancies) which trap the photocurrent and result in high recombination of hot electrons and holes.

Bibliography

- [1] S. A. Dereshgi and A. Okyay, “Mimim photodetectors using plasmonically enhanced mim absorbers,” in *Proc. of SPIE Vol*, vol. 10099, pp. 100991C–1, 2017.
- [2] S. A. Dereshgi, Z. Sisman, K. Topalli, and A. K. Okyay, “Plasmonically enhanced metal–insulator multistacked photodetectors with separate absorption and collection junctions for near-infrared applications,” *Scientific Reports*, vol. 7, 2017.
- [3] S. A. Dereshgi and A. K. Okyay, “Large area compatible broadband superabsorber surfaces in the vis-nir spectrum utilizing metal-insulator-metal stack and plasmonic nanoparticles,” *Optics Express*, vol. 24, no. 16, pp. 17644–17653, 2016.
- [4] H. Choo, M.-K. Kim, M. Staffaroni, T. J. Seok, J. Bokor, S. Cabrini, P. J. Schuck, M. C. Wu, and E. Yablonovitch, “Nanofocusing in a metal-insulator-metal gap plasmon waveguide with a three-dimensional linear taper,” *Nature Photonics*, vol. 6, no. 12, pp. 838–844, 2012.
- [5] K. Kim, S.-Y. Lee, H. Yun, J.-B. Park, and B. Lee, “Switchable beaming from a nanoslit with metallic gratings controlled by the phase difference between incident beams,” *Optics express*, vol. 22, no. 5, pp. 5465–5473, 2014.
- [6] N. Landy, C. Bingham, T. Tyler, N. Jokerst, D. Smith, and W. Padilla, “Design, theory, and measurement of a polarization-insensitive absorber for terahertz imaging,” *physical review B*, vol. 79, no. 12, p. 125104, 2009.

- [7] M. Diem, T. Koschny, and C. M. Soukoulis, “Wide-angle perfect absorber/thermal emitter in the terahertz regime,” *Physical Review B*, vol. 79, no. 3, p. 033101, 2009.
- [8] H. A. Atwater and A. Polman, “Plasmonics for improved photovoltaic devices,” *Nature materials*, vol. 9, no. 3, pp. 205–213, 2010.
- [9] L. Tang, S. E. Kocabas, S. Latif, A. K. Okyay, D.-S. Ly-Gagnon, K. C. Saraswat, and D. A. Miller, “Nanometre-scale germanium photodetector enhanced by a near-infrared dipole antenna,” *Nature Photonics*, vol. 2, no. 4, pp. 226–229, 2008.
- [10] C. Min, J. Li, G. Veronis, J.-Y. Lee, S. Fan, and P. Peumans, “Enhancement of optical absorption in thin-film organic solar cells through the excitation of plasmonic modes in metallic gratings,” *Applied Physics Letters*, vol. 96, no. 13, p. 56, 2010.
- [11] A. Tittl, P. Mai, R. Taubert, D. Dregely, N. Liu, and H. Giessen, “Palladium-based plasmonic perfect absorber in the visible wavelength range and its application to hydrogen sensing,” *Nano letters*, vol. 11, no. 10, pp. 4366–4369, 2011.
- [12] K. Nakayama, K. Tanabe, and H. A. Atwater, “Plasmonic nanoparticle enhanced light absorption in gaas solar cells,” *Applied Physics Letters*, vol. 93, no. 12, p. 121904, 2008.
- [13] J. N. Anker, W. P. Hall, O. Lyandres, N. C. Shah, J. Zhao, and R. P. Van Duyne, “Biosensing with plasmonic nanosensors,” *Nature materials*, vol. 7, no. 6, pp. 442–453, 2008.
- [14] P. K. Jain, K. S. Lee, I. H. El-Sayed, M. A. El-Sayed, *et al.*, “Calculated absorption and scattering properties of gold nanoparticles of different size, shape, and composition: applications in biological imaging and biomedicine,” *Journal of Physical Chemistry B*, vol. 110, no. 14, p. 7238, 2006.
- [15] J. R. Cole and N. Halas, “Optimized plasmonic nanoparticle distributions for solar spectrum harvesting,” *Applied physics letters*, vol. 89, no. 15, p. 153120, 2006.

- [16] H. Gao, C. Liu, H. E. Jeong, and P. Yang, “Plasmon-enhanced photocatalytic activity of iron oxide on gold nanopillars,” *ACS nano*, vol. 6, no. 1, pp. 234–240, 2011.
- [17] S.-J. Tsai, M. Ballarotto, D. B. Romero, W. N. Herman, H.-C. Kan, and R. J. Phaneuf, “Effect of gold nanopillar arrays on the absorption spectrum of a bulk heterojunction organic solar cell,” *Optics express*, vol. 18, no. 104, pp. A528–A535, 2010.
- [18] P. Senanayake, C.-H. Hung, J. Shapiro, A. Lin, B. Liang, B. S. Williams, and D. Huffaker, “Surface plasmon-enhanced nanopillar photodetectors,” *Nano letters*, vol. 11, no. 12, pp. 5279–5283, 2011.
- [19] M. G. Nielsen, A. Pors, O. Albrektsen, and S. I. Bozhevolnyi, “Efficient absorption of visible radiation by gap plasmon resonators,” *Optics express*, vol. 20, no. 12, pp. 13311–13319, 2012.
- [20] C. Yang, C. Ji, W. Shen, K.-T. Lee, Y. Zhang, X. Liu, and L. J. Guo, “Compact multilayer film structures for ultrabroadband, omnidirectional, and efficient absorption,” *ACS Photonics*, vol. 3, no. 4, pp. 590–596, 2016.
- [21] Q. Liang, T. Wang, Z. Lu, Q. Sun, Y. Fu, and W. Yu, “Metamaterial-based two dimensional plasmonic subwavelength structures offer the broadest waveband light harvesting,” *Advanced Optical Materials*, vol. 1, no. 1, pp. 43–49, 2013.
- [22] M. A. Kats, R. Blanchard, P. Genevet, and F. Capasso, “Nanometre optical coatings based on strong interference effects in highly absorbing media,” *Nature materials*, vol. 12, no. 1, pp. 20–24, 2013.
- [23] M. Chirumamilla, A. S. Roberts, F. Ding, D. Wang, P. K. Kristensen, S. I. Bozhevolnyi, and K. Pedersen, “Multilayer tungsten-alumina-based broadband light absorbers for high-temperature applications,” *Optical Materials Express*, vol. 6, no. 8, pp. 2704–2714, 2016.
- [24] Z. Li, E. Palacios, S. Butun, H. Kocer, and K. Aydin, “Omnidirectional, broadband light absorption using large-area, ultrathin lossy metallic film coatings,” *Scientific reports*, vol. 5, p. 15137, 2015.

- [25] G. Kajtár, M. Kafesaki, E. Economou, and C. Soukoulis, “Theoretical model of homogeneous metal–insulator–metal perfect multi-band absorbers for the visible spectrum,” *Journal of Physics D: Applied Physics*, vol. 49, no. 5, p. 055104, 2016.
- [26] Y. K. Zhong, Y.-C. Lai, M.-H. Tu, B.-R. Chen, S. M. Fu, P. Yu, and A. Lin, “Omnidirectional, polarization-independent, ultra-broadband metamaterial perfect absorber using field-penetration and reflected-wave-cancellation,” *Optics express*, vol. 24, no. 10, pp. A832–A845, 2016.
- [27] H. Kocer, S. Butun, Z. Li, and K. Aydin, “Reduced near-infrared absorption using ultra-thin lossy metals in fabry-perot cavities,” *Scientific reports*, vol. 5, p. 8157, 2015.
- [28] N. Mattiucci, M. Bloemer, N. Aközbek, and G. D’Aguanno, “Impedance matched thin metamaterials make metals absorbing,” *Scientific reports*, vol. 3, 2013.
- [29] H. Deng, Z. Li, L. Stan, D. Rosenmann, D. Czaplewski, J. Gao, and X. Yang, “Broadband perfect absorber based on one ultrathin layer of refractory metal,” *Optics letters*, vol. 40, no. 11, pp. 2592–2595, 2015.
- [30] L. G. Burriesci, “Nircam instrument overview,” in *Optics & Photonics 2005*, pp. 590403–590403, International Society for Optics and Photonics, 2005.
- [31] J. B. Soole and H. Schumacher, “Ingaas metal-semiconductor-metal photodetectors for long wavelength optical communications,” *IEEE journal of quantum electronics*, vol. 27, no. 3, pp. 737–752, 1991.
- [32] J. C. Campbell, “Recent advances in telecommunications avalanche photodiodes,” *Journal of Lightwave Technology*, vol. 25, no. 1, pp. 109–121, 2007.
- [33] M. P. Hansen and D. S. Malchow, “Overview of swir detectors, cameras, and applications,” in *SPIE Defense and Security Symposium*, pp. 69390I–69390I, International Society for Optics and Photonics, 2008.

- [34] L. Chaerle and D. Van Der Straeten, "Seeing is believing: imaging techniques to monitor plant health," *Biochimica et Biophysica Acta (BBA)-Gene Structure and Expression*, vol. 1519, no. 3, pp. 153–166, 2001.
- [35] B. G. Osborne, T. Fearn, P. H. Hindle, *et al.*, *Practical NIR spectroscopy with applications in food and beverage analysis*. Longman scientific and technical, 1993.
- [36] M. Blanco and I. Villarroya, "Nir spectroscopy: a rapid-response analytical tool," *TrAC Trends in Analytical Chemistry*, vol. 21, no. 4, pp. 240–250, 2002.
- [37] M. W. Knight, H. Sobhani, P. Nordlander, and N. J. Halas, "Photodetection with active optical antennas," *Science*, vol. 332, no. 6030, pp. 702–704, 2011.
- [38] W. Cai and V. M. Shalaev, *Optical metamaterials*, vol. 10. Springer, 2010.
- [39] V. M. Shalaev, W. Cai, U. K. Chettiar, H.-K. Yuan, A. K. Sarychev, V. P. Drachev, and A. V. Kildishev, "Negative index of refraction in optical metamaterials," *Optics letters*, vol. 30, no. 24, pp. 3356–3358, 2005.
- [40] G. Dolling, C. Enkrich, M. Wegener, C. M. Soukoulis, and S. Linden, "Simultaneous negative phase and group velocity of light in a metamaterial," *Science*, vol. 312, no. 5775, pp. 892–894, 2006.
- [41] S. Linden, C. Enkrich, M. Wegener, J. Zhou, T. Koschny, and C. M. Soukoulis, "Magnetic response of metamaterials at 100 terahertz," *Science*, vol. 306, no. 5700, pp. 1351–1353, 2004.
- [42] E. Plum, V. Fedotov, A. Schwanecke, N. Zheludev, and Y. Chen, "Giant optical gyrotropy due to electromagnetic coupling," *Applied Physics Letters*, vol. 90, no. 22, p. 223113, 2007.
- [43] M. W. Klein, C. Enkrich, M. Wegener, and S. Linden, "Second-harmonic generation from magnetic metamaterials," *Science*, vol. 313, no. 5786, pp. 502–504, 2006.
- [44] W. Cai, D. A. Genov, and V. M. Shalaev, "Superlens based on metal-dielectric composites," *Physical review B*, vol. 72, no. 19, p. 193101, 2005.

- [45] Z. Liu, H. Lee, Y. Xiong, C. Sun, and X. Zhang, “Far-field optical hyperlens magnifying sub-diffraction-limited objects,” *science*, vol. 315, no. 5819, pp. 1686–1686, 2007.
- [46] W. Cai, U. K. Chettiar, A. V. Kildishev, and V. M. Shalaev, “Optical cloaking with metamaterials,” *Nature photonics*, vol. 1, no. 4, pp. 224–227, 2007.
- [47] W. Cai, U. K. Chettiar, A. V. Kildishev, V. M. Shalaev, and G. W. Milton, “Nonmagnetic cloak with minimized scattering,” *Applied Physics Letters*, vol. 91, no. 11, p. 111105, 2007.
- [48] D. A. Miller, *Quantum mechanics for scientists and engineers*. Cambridge University Press, 2008.
- [49] W. Chow, “Theory of phonon-assisted optical absorption in semiconductors. i.,” *Physical Review*, vol. 185, no. 3, p. 1056, 1969.
- [50] N. V. Tkachenko, *Optical spectroscopy: methods and instrumentations*. Elsevier, 2006.
- [51] M. Casalino, G. Coppola, M. Iodice, I. Rendina, and L. Sirleto, “Near-infrared sub-bandgap all-silicon photodetectors: state of the art and perspectives,” *Sensors*, vol. 10, no. 12, pp. 10571–10600, 2010.
- [52] S. A. Maier, *Plasmonics: fundamentals and applications*. Springer Science & Business Media, 2007.
- [53] E. Kretschmann and H. Raether, “Notizen: radiative decay of non radiative surface plasmons excited by light,” *Zeitschrift für Naturforschung A*, vol. 23, no. 12, pp. 2135–2136, 1968.
- [54] A. Otto, “Excitation of nonradiative surface plasma waves in silver by the method of frustrated total reflection,” *Zeitschrift für Physik*, vol. 216, no. 4, pp. 398–410, 1968.
- [55] E. Devaux, T. W. Ebbesen, J.-C. Weeber, and A. Dereux, “Launching and decoupling surface plasmons via micro-gratings,” *Applied physics letters*, vol. 83, no. 24, pp. 4936–4938, 2003.

- [56] M. M. Alvarez, J. T. Khoury, T. G. Schaaff, M. N. Shafigullin, I. Vezmar, and R. L. Whetten, “Optical absorption spectra of nanocrystal gold molecules,” *The Journal of Physical Chemistry B*, vol. 101, no. 19, pp. 3706–3712, 1997.
- [57] M. Meier and A. Wokaun, “Enhanced fields on large metal particles: dynamic depolarization,” *Optics letters*, vol. 8, no. 11, pp. 581–583, 1983.
- [58] E. K. Payne, K. L. Shuford, S. Park, G. C. Schatz, and C. A. Mirkin, “Multipole plasmon resonances in gold nanorods,” *The journal of physical chemistry. B*, vol. 110, no. 5, p. 2150, 2006.
- [59] Lumerical solutions, Inc., “Finite-difference time-domain solutions.”
- [60] M. G. Nielsen, D. K. Gramotnev, A. Pors, O. Albrektsen, and S. I. Bozhevolnyi, “Continuous layer gap plasmon resonators,” *Optics express*, vol. 19, no. 20, pp. 19310–19322, 2011.
- [61] D. M. Pozar, *Microwave engineering*. John Wiley & Sons, 2009.
- [62] C. A. Balanis, *Advanced engineering electromagnetics*. John Wiley & Sons, 2012.
- [63] M. L. Brongersma, N. J. Halas, and P. Nordlander, “Plasmon-induced hot carrier science and technology,” *Nature nanotechnology*, vol. 10, no. 1, pp. 25–34, 2015.
- [64] B. E. Saleh, M. C. Teich, and B. E. Saleh, *Fundamentals of photonics*, vol. 22. Wiley New York, 1991.
- [65] S. M. Sze, *Semiconductor devices: physics and technology*. John Wiley & Sons, 2008.
- [66] T. Pearsall, “Semiconductors and semimetals, vol. 32,” in *Strained-Layer Superlattices.*, Academic Press Boston, 1990.
- [67] A. K. Sood, J. W. Zeller, R. A. Richwine, Y. R. Puri, H. Efstathiadis, P. Haldar, N. K. Dhar, and D. L. Polla, “Sige based visible-nir photodetector technology for optoelectronic applications,” *Chapter in Advances in Optical*

Fiber Technology: Fundamental Optical Phenomena and Applications, edited by M. Yasin, H. Arof, and SW Harun, Intech, 2015.

- [68] F. D. P. Alves, G. Karunasiri, N. Hanson, M. Byloos, H. Liu, A. Bezinger, and M. Buchanan, “Nir, mwir and lwir quantum well infrared photodetector using interband and intersubband transitions,” *Infrared physics & technology*, vol. 50, no. 2, pp. 182–186, 2007.
- [69] J. H. Werner, “Schottky barrier and pn-junctioni/v plotssmall signal evaluation,” *Applied Physics A: Materials Science & Processing*, vol. 47, no. 3, pp. 291–300, 1988.
- [70] S. Cheung and N. Cheung, “Extraction of schottky diode parameters from forward current-voltage characteristics,” *Applied Physics Letters*, vol. 49, no. 2, pp. 85–87, 1986.
- [71] M. Alavirad, A. Olivieri, L. Roy, and P. Berini, “High-responsivity sub-bandgap hot-hole plasmonic schottky detectors,” *Optics express*, vol. 24, no. 20, pp. 22544–22554, 2016.
- [72] H. Muta, “Electrical properties of platinum-silicon contact annealed in an h2 ambient,” *Japanese Journal of Applied Physics*, vol. 17, no. 6, p. 1089, 1978.
- [73] M. A. Nazirzadeh, F. B. Atar, B. B. Turgut, and A. K. Okyay, “Random sized plasmonic nanoantennas on silicon for low-cost broad-band near-infrared photodetection,” *Scientific reports*, vol. 4, p. 7103, 2014.
- [74] J. W. Haus, D. de Ceglia, M. A. Vincenti, and M. Scalora, “A quantum tunneling theory for nanophotonics,” in *SPIE OPTO*, pp. 89941Q–89941Q, International Society for Optics and Photonics, 2014.
- [75] F. Wang and N. A. Melosh, “Plasmonic energy collection through hot carrier extraction,” *Nano letters*, vol. 11, no. 12, pp. 5426–5430, 2011.
- [76] F. B. Atar, E. Battal, L. E. Aygun, B. Daglar, M. Bayindir, and A. K. Okyay, “Plasmonically enhanced hot electron based photovoltaic device,” *Optics express*, vol. 21, no. 6, pp. 7196–7201, 2013.

- [77] UNAM (National Nanotechnology Research Center).
- [78] Nanotechnology Research Center).
- [79] K. Yee, “Numerical solution of initial boundary value problems involving maxwell’s equations in isotropic media,” *IEEE Transactions on antennas and propagation*, vol. 14, no. 3, pp. 302–307, 1966.
- [80] J. D. Plummer, *Silicon VLSI technology: fundamentals, practice and modeling*. Pearson Education India, 2009.
- [81] M. Leskelä and M. Ritala, “Atomic layer deposition (ald): from precursors to thin film structures,” *Thin solid films*, vol. 409, no. 1, pp. 138–146, 2002.
- [82] R. L. Puurunen, “Surface chemistry of atomic layer deposition: A case study for the trimethylaluminum/water process,” *Journal of applied physics*, vol. 97, no. 12, p. 9, 2005.
- [83] L. Leger and J. Joanny, “Liquid spreading,” *Reports on Progress in Physics*, vol. 55, no. 4, p. 431, 1992.
- [84] J. A. Woollam Co., Inc., “Guide to using wvase spectroscopic ellipsometry data acquisition and analysis software.”
- [85] E. D. Palik, *Handbook of optical constants of solids*, vol. 3. Academic press, 1998.
- [86] P. B. Johnson and R.-W. Christy, “Optical constants of the noble metals,” *Physical review B*, vol. 6, no. 12, p. 4370, 1972.

Appendix A

ALD Recipe and Characterization

Al₂O₃. All Al₂O₃ films in this thesis were deposited using Cambridge Nanotech Savanna S100 system. The deposition recipe of 40 nm Al₂O₃ is provided in Table A.1.

In Table A.1, heater 8 and 9 stand for the temperatures of pipes and chamber which represent deposition at 200°C. The stabilize command is introduced to minimize the variations of the temperatures of the heaters before starting the deposition. The “flow” command is for the carrier and purge gas N₂ flow rate. Pulse 0 commands the opening of the valve which is connected to milli-Q water and similar one is for pulse 3 for Trimethylaluminum. In other words, water and TMA are attached to valves 0 and 3 respectively in our ALD system. The wait commands are introduced after each valving so that enough time is given for reaction to take place and the reactant to be purged from the chamber. The “goto” command denotes the repetition of deposition cycle for 400 times. Figure A.1 shows the refractive index data of the deposited Al₂O₃ film extracted with ellipsometer using Cauchy model which assumes that $k=0$. The Cauchy model is applicable since the film is transparent in VIS-NIR spectrum.

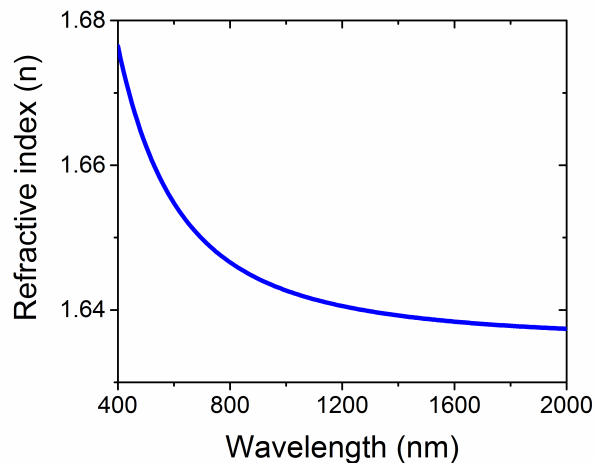


Figure A.1: Refractive index data of the deposited Al_2O_3 at 200°C .

The ellipsometer spectroscopic data shows the thickness of approximately 40.5 nm which corresponds to a deposition rate of $1.001 \text{ \AA}/\text{cycle}$.

HfO₂. Analogous to Al_2O_3 , HfO_2 was also deposited using the same ALD system at 200°C . In order to be able to characterize the film (4 nm tunneling layer was too thin), 10 nm deposition was carried out, the recipe of which is provided in Table A.2.

The same discussion applies to this recipe as well where the only difference is that Trimethylhafnium is installed to valve number 4. The refractive index versus wavelength for HfO_2 extracted using Cauchy model in ellipsometer is provided in Fig. A.2.

The calculated rate was $0.9871 \text{ \AA}/\text{cycle}$. Since the uniformity of HfO_2 was critical as very thin (4 nm) tunneling insulator, a uniformity measurement was done by measuring thicknesses at four different points on a 4 inch wafer for 10 nm deposition case. Note that the uniformity in the fabricated sample is very high since the sample is only $2 \text{ cm} \times 2 \text{ cm}$. The uniformity in the 4 inch wafer is still acceptably well.

Table A.1: Al₂O₃ deposition recipe in ALD.

Row	Instruction	#	Value	Units
0	heater	8	200	°C
1	heater	9	200	°C
2	stabilize	8		
3	stabilize	9		
4	wait		200	sec
5	flow		20	sccm
6	wait		30	sec
7	pulse	0	0.015	sec
8	wait		8	sec
9	pulse	3	0.015	sec
10	wait		8	sec
11	goto	7	400	times

Table A.2: HfO₂ deposition recipe in ALD.

Row	Instruction	#	Value	Units
0	heater	8	200	°C
1	heater	9	200	°C
2	stabilize	8		
3	stabilize	9		
4	wait		200	sec
5	flow		20	sccm
6	wait		30	sec
7	pulse	0	0.015	sec
8	wait		8	sec
9	pulse	4	0.015	sec
10	wait		8	sec
11	goto	7	100	times

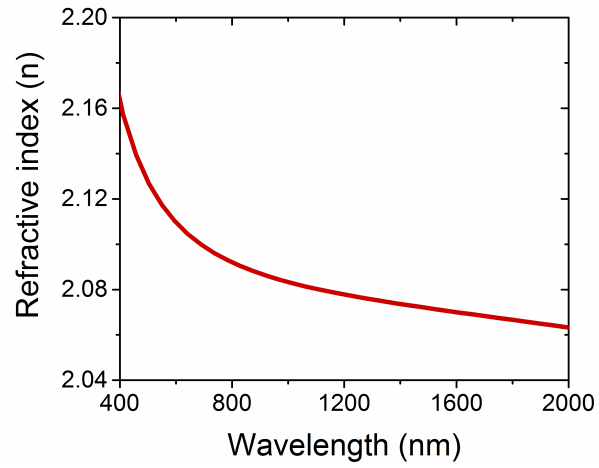


Figure A.2: Refractive index data of the deposited HfO₂ at 200°C.

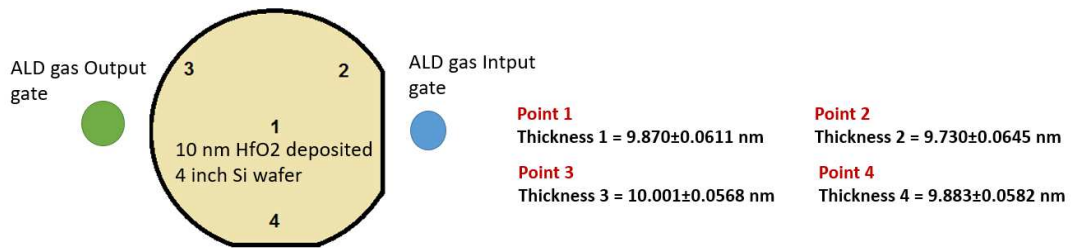


Figure A.3: Uniformity test of deposited HfO₂ at 200°C on a 4 inch wafer.